
INSTITUTE OF PHYSICS,
POLISH ACADEMY OF SCIENCES

DOCTORAL DISSERTATION

---

# Exploring electronic properties of topological semimetals $TaAs_2$ and NbP: crystal growth, electron transport and ARPES studies

---

**Author**
Ashutosh S. Wadge

**Advisor**
Prof. dr hab. Andrzej Wiśniewski


**International Centre for Interfacing Magnetism and Superconductivity with Topological Matter – MagTop**

June 2023

*The Fermi surface, a stage adorned*
*where electrons dance, their tale untold*
*upon its grand theatre, their lives unfold*
*a drama captivating, their stories bold*

Ashutosh S. Wadge

*To my family for their endless love,*
*to K. Ryczkowski for inspiration.*

# Statement

"The data presented in this thesis are original and have been meticulously collected through crystal growth, electron transport and ARPES techniques. All figures referenced in this thesis have been appropriately obtained with permission (listed below) from the respective journals, ensuring the accuracy and integrity of the information presented."

- License Number: 1358018
- License Number: RNP/23/MAY/066524
- License Number: RNP/23/MAY/066522
- License Number: RNP/23/MAY/066523

# Acknowledgement

I would like to express my gratitude to Prof. T. Dietl and Prof. T. Wojtowicz, the heads of the MAGTOP research group. Their support and guidance have created an exceptional environment that has nurtured my growth, allowing me to flourish from a novice researcher to the accomplished individual I am today.

I am grateful to Prof. A. Wiśniewski, my supervisor, for his unwavering support and belief in my research ideas and perspectives. Throughout my PhD journey, he extended his help in resolving complex problems, providing valuable guidance, and granting access to state-of-the-art lab facilities.

I am indebted to Prof. B. Kowalski for his invaluable guidance in teaching me the details of ARPES techniques right from the basics. Our fruitful discussions and interactions have enhanced my understanding of this field. I would like to express my sincere thanks to Prof. G. Grabecki for his invaluable support in teaching me electron transport techniques and granting me access to the cryostat facility.

I am grateful to Dr. P. Iwanowski and Dr. A. Hruban for their exceptional mentorship in teaching me the complex process of chemical vapor transport. I am grateful to MSc. D. Jastrzębski and MSc. K. Cieslak for their kind support and would like to thank them.

I want to express my sincere gratitude to Prof. C. Autieri for his contribution to providing theoretical support for my research. Without his guidance and expertise, it would have been challenging to bridge the gap between theory and experiment.

I am grateful to Prof. T. Story for his invaluable suggestions during our weekly meetings. His expertise and help have been crucial in navigating and resolving complex problems throughout my research. I also would like to acknowledge MSc. M. Rosmus for his help regarding IGOR pro scripts to extract the ARPES data and beamline scientist Dr. N. Olszowska for her support during beam time at the SOLARIS Synchrotron facility in Cracow, Poland.

I would like to express my deepest gratitude to Dr A. Kazakov and Prof. K. Dybko for their unwavering support and motivation throughout

my journey. Their help in electron transport, along with the provision of necessary facilities, has been helpful in my research. I would like to thank Dr. R. Diduszko for the X-ray diffraction measurements. Dr T. Wojciechowski for EDX and SEM measurements, Prof. P. Dłużewski and MSc. B. Kurowska for transmission electron microscopy measurements. Dr. M. Foltyn for providing me with wire-bonding and Al deposition facility and for inspiration. MSc. J. Polaczyński's guidance and expertise in various techniques in deposition and lithography have been helpful in expanding my skill set. I am grateful to MSc. B. Turowski for his assistance in providing a Python script to facilitate data slicing for ARPES analysis, as well as his help with the software aspects. Their support and willingness to lend a helping hand have been truly appreciated. I also would like to thank all MAGTOP members and my crystal growth team to support me during my PhD studies. I also would like to acknowledge our secretaries Ms A. Kozakiewicz, Ms. A. Kniola and Ms. S. Nowicka for their support during PhD studies.

I am deeply thankful to my friends and colleagues T. Paul, M. Białobrzewski and Adil for their support and motivation. I am grateful to my close friends in Poland, Adriana, Ewa, Martyna, Iga, Wiktor, Michał, Mateusz, Julia, Nikola and Kamil. I would like to thank them and appreciate their support during the journey. I am eternally grateful to Ms. A. Ryczkowska, Mr. R. Ryczkowski and K. Ryczkowski for taking care of me, motivating me, and getting happy over every small achievement especially Ms. Anna for cooking delicious Polish cuisine for me. I also would like to appreciate my very close friends Apoorva, Tejas, and Sushil to support me through my emotional ups and downs and inspire me. I would like to acknowledge my friends Sarita, Nikhil and Venugopal to inspire me. Also, I am deeply thankful to my Indian friends in Poland, Ishika, Abinash, Pradosh, Sukant, Suhani and Ruchi for supporting me and cooking delicious Indian food. I am thankful to Ms. A. Jedrzejewska, Ms. Bożena and Ms. Jolanta for their great support in the Guest house of IFPAN. I appreciate my Uncle M. Bachhav for supporting me during my studies. Finally, I would like to express my deepest gratitude towards my loving family especially my brother Nilesh, who always inspires me by saying "Remember, there is always Schrodinger's cat alive!"

# Academic achievements

## Publications

1. **A. S. Wadge**, G. Grabecki, C. Autieri, B. J. Kowalski, P. Iwanowski, G. Cuono, M. F. Islam, C. M. Canali, K. Dybko, A. Hruban, A. Łusakowski, T. Wojciechowski, R. Diduszko, A. Lynnyk, N. Olszowska, M. Rosmus, J. Kołodziej, and A. Wisniewski, Electronic properties of $TaAs_2$ topological semimetal investigated by transport and ARPES, J. Phys.: Condens. Matter **34**, 125601 (2022).

2. **A. S. Wadge**, B.J. Kowalski, C. Autieri, P. Iwanowski, A. Hruban, N. Olszowska, M. Rosmus, J. Kołodziej and A. Wiśniewski, Topological Lifshitz transition in Weyl semimetal NbP decorated with heavy elements, Phys. Rev. B **105**, 235304 (2022).

3. M. S. Alam, P. K. Tanwar, K. Dybko, **A. S. Wadge**, P. Iwanowski, A. Wiśniewski, and M. Matusiak, Temperature-driven spin-zero effect in $TaAs_2$, J. Phys. Chem. Solids **170**, 110939 (2022).

## Oral Presentation

1. **A. S. Wadge, et al.**, Joint European Magnetism Symposia Conference (JEMS 2022), "Surface decorated Weyl semimetal: topological quantum Lifshitz transition", (24-29 July 2022), Poland.
   **Contributed talk**

2. Centre for Nanotechnology Research, VIT University, Vellore, India "Angle-resolved photoemission spectroscopic study of topological Weyl semimetals", (22 March 2022).
   **Invited talk**

# Poster Presentation

1. **A. S. Wadge et al.**, Northern Lights Conference 2022, "Surface decorated topological Lifshitz transition in Weyl semimetal: NbP", (12-15 October 2023), Reykjavik, Iceland.

2. **A. S. Wadge et al.**, $4^{th}$ Interdisciplinary FNP Conference, "Interfacing NbP Weyl semimetal with superconducting elements", (6-7 October 2022), Warsaw, Poland.

3. **A. S. Wadge et al.**, $50^{th}$ International School and Conference on the Physics of Semiconductors (Jaszowiec 2022), "Manipulation of surface states in topological Weyl semimetal(NbP): An ARPES study", (4-10 June 2022), Szczyrk, Poland.
   **Best poster award**

4. **A. S. Wadge et al.**, International School and Conference on the Physics of Semiconductors (Jaszowiec 2021) (Virtual), "Electron transport and ARPES study on topological semimetal: $TaAs_2$", (1-10 September 2021), Poland.

5. **A. S. Wadge et al.**, Joint Meeting of Polish Synchrotron Society and SOLARIS Users (Virtual), "Anisotropy of the Fermi surface of non-magnetic semimetal $TaAs_2$", (9-11 Sepember. 2020), Poland.

# Abstract

In this PhD thesis, we investigated the electronic properties of two topological semimetals, $TaAs_2$ and NbP. Electron transport and angle-resolved photoemission spectroscopy (ARPES) measurements were performed on $TaAs_2$ single crystals on $(\bar{2}01)$ surface. Fourier analysis of the Shubnikov–de Haas oscillations revealed four distinct peaks and their angular dependence was examined relative to the magnetic field orientation. The results indicate elliptical Fermi surface cross-sections. Mobility spectrum analysis confirmed the presence of at least four types of carriers contributing to the conductance at 1.6 K, including two types of electrons and two types of holes. ARPES spectra on the freshly cleaved $(\bar{2}01)$ surface confirmed the elliptical shape of the bulk states pockets, supporting the magnetotransport angle-dependent studies. With an increased Fermi level due to weak n-doping, theoretical calculations reproduced the ARPES data better. The studies facilitated the understanding of the physics of Dirac and Weyl points in this compound.

Furthermore, we performed ARPES studies to examine Fermi surface modifications in NbP semimetal with in-situ deposition of ultra-thin layers of Pb and Nb. Pristine single crystals with P and Nb terminations of the (0 0 1) surface were investigated. The P-terminated surface exhibited spoon and bow-tie-shaped surface states, while the Nb-terminated surface lacked these features. Deposition of a single monolayer (ML) of Pb induced a topological Lifshitz transition (TLT) in P-terminated NbP, exchanging the pair of Weyl points connecting adjacent Brillouin zones. The Fermi surface was modified along with a shift in the Fermi energy. On the other hand, the deposition of approximately 0.8 ML of Nb pushed the electronic structure of P-terminated NbP close to the critical point of a TLT, partial transformation. Despite the Fermi surface evolution, surface Fermi arcs remained connected to topologically protected Weyl points. Additionally, Nb-terminated NbP covered with 1.9 ML of Pb exhibited altered trivial surface states caused by Lifshitz transition.

# Streszczenie

W pracy doktorskiej zostały przedstawione wyniki badań elektronowych właściwości dwóch topologicznych półmetali: $TaAs_2$ i NbP. Badania transportowe i kątowo-rozdzielczej spektroskopii fotoelektronów (ARPES) monokryształów $TaAs_2$ zostały przeprowadzone dla powierzchni $(\bar{2}01)$. Analiza fourierowska oscylacji Shubnikova-de Haasa wykazała istnienie czterech wyraźnych maksimów, zbadano kątową zależność ich położenia od kierunku zewnętrznego pola magnetycznego. Otrzymane rezultaty wskazują na eliptyczny kształt przekrojów powierzchni Fermiego. Analiza widma ruchliwości nośników pokazuje występowanie co najmniej czterech rodzajów nośników, dwóch rodzajów elektronów i dwóch rodzajów dziur, dających wkład do przewodnictwa w temperaturze 1,6 K. Widma ARPES zarejestrowane dla świeżo odsłoniętej powierzchni $(\bar{2}01)$ świadczą o eliptycznym kształcie „kieszeni" związanych ze stanami objętościowymi, potwierdzając tym samym wyniki badania magneto-transportowych zależności kątowych. Obliczenia teoretyczne przeprowadzone przy założeniu wyższego położenia poziomu Fermiego, ze względu na małe domieszkowanie typu n, lepiej odtwarzają wyniki ARPES i ułatwiają zrozumienie fizyki związanej z punktami Diraca i Weyla występującymi w tym związku.
Metodą ARPES przeprowadzono badania modyfikacji powierzchni Fermiego półmetalu NbP, który został pokryty in-situ ultra cienkimi warstwami Pb i Nb. Badano świeżo odsłonięte powierzchnie (001) NbP zakończone warstwą atomów P lub Nb. Powierzchnie zakończone warstwą P wykazują kształt stanów powierzchniowych zbliżony do kształtu łyżeczki lub muszki, stany powierzchni zakończonej warstwą Nb nie wykazują takich cech. Pokrycie powierzchni NbP zakończonej warstwą P jedną monowarstwą (ML) Pb indukuje topologiczne przejście Lifshitza (TLT), którego skutkiem jest zamiana pary punktów Weyla łączących przylegające strefy Brillouina. Powierzchnia Fermiego została zmodyfikowana wraz z przesunięciem poziomu energii Fermiego. Z kolei nałożenie około 0,8 ML atomów Nb na powierzchnię zakończoną warstwą P powoduje tylko częściową transformację, prowadząc do przesunięcia struktury elektronowej w kierunku punktu krytycznego TLT. Niezależnie od ewolucji powierzchni Fermiego, powierzchniowe łuki

Fermiego pozostają połączone z chronionymi topologicznie punktami Weyla. Powierzchnia NbP zakończona warstwą Nb, po pokryciu jej 1,9 ML Pb, wykazuje modyfikację trywialnych (nie topologicznych) stanów powierzchniowych spowodowaną przejściem Lifshitza.

# Contents

# List of Figures

# List of Tables

# Motivation

In the last decade, the discovery of topological phases is a major scientific breakthrough in condensed matter physics. It has been shown that the study of the integer quantum Hall effect reflects the emergence of topological phases in which electron becomes massless while carrying current on their surface without dissipation [1–4]. Topological insulators (TIs) exhibit gapless metallic surface or edge states, alongside a bulk gap. The presence of surface states (SS) was initially observed in a two-dimensional electron gas system [5]. Surprisingly, three-dimensional topological insulators, such as $Bi_xSb_{1-x}$, have shown band inversion with strong spin-orbit interaction. As a result of it, SS occur in three-dimensional TI with Dirac cone-type dispersion [6–9]. Successively, a class of material that gives metallic SS with band degeneracy protected by crystalline symmetry has been found, which influenced the field of topological insulators [10].

Another family of quantum materials known as topological semimetals (TSMs) has made an outstanding impact and enriched the field of topological materials [11, 12]. Tantalum di-arsenide ($TaAs_2$) is one of the di-pnictide family candidates with remarkable properties such as large unsaturated positive magnetoresistance, pronounced Shubnikov-de Haas oscillations, ultrahigh mobility of carriers, etc. The electronic band structure of $TaAs_2$ exhibits nodal lines in the absence of spin-orbit coupling (SOC), while these lines become gapped and exhibit band inversion upon the inclusion of SOC [13, 14]. These electronic properties in $TaAs_2$ are strongly orientation dependent. The majority of previous studies are mainly based either on experimental electron transport or theoretical band structure calculations of $TaAs_2$. In 2016, Y. Luo, et al. [15] have shown the existence of giant semi-classical magnetoresistance (MR) mechanism in $TaAs_2$ semimetal. The electron transport was taken at the (0 0 1) plane. They found quantum oscillations in the material that was supported by first principle calculations [16]. Later, Z. Yuan et al. elaborated on the concept of large magnetoresistance in $TaAs_2$ based on the charge compensation phenomenon [17]. Furthermore, in the same year, a group of Y. Luo showed experimental results on MR, quantum oscillation, angle dependence and negative magnetoresistance in

support of density functional theory (DFT). They discussed that the SS in $TaAs_2$ are governed by non-trivial weak topological indices [15]. Additionally, some theoretical articles studied this material and showed some facts such as the existence of type II Weyl points (tilted Weyl cones formed due to crossing of two Fermi pockets) in the presence of a magnetic field, surface-dependent spin zero effect, topological crystalline insulating states protected by rotational symmetry [14, 18, 19]. Subsequently, T. Butcher, et al. investigated the Fermi surface with electron-hole pockets by de Haas–van Alphen effect and with DFT calculations [20].

This dissertation emphasizes some unexplored problems such as the angle-resolved photoemission spectroscopic study (ARPES) of $TaAs_2$ showing the existence of electron and hole pockets in momentum space with DFT support as well as mobility spectrum analysis based on electron transport data along with single crystal growth. Previous studies lack a visualization of carriers with different mobility present in this material; hence mobility spectrum analysis gave more precise data in the case of multi-carriers which was analyzed in the given study.

Topological Weyl semimetal (TWS) exhibits the existence of an exotic phase of the quantum matter which hosts the Weyl fermions. They are named after the physicist Herman Weyl who solved the Dirac equation for massless fermions with spin $\frac{1}{2}$ and the solution predicted the existence of particles with defined chirality [21]. TWS has topological characteristics such as Weyl points (WPs), which are bulk-protected. Their surface projection manifests open Fermi surface states called surface Fermi arcs (SFAs) [22]. These signatures can be visualized by using a surface-sensitive ARPES technique [23–25]. The literature survey shows that Y. Sun, et al. [26] theoretically investigated the SS in the TaAs family by using ab-initio band structure calculations. This article also showed the existence of the polar nature of tantalum monophosphide (TaP) with different electronic structures and SS modifications by doping light element (K) on the surface [26–29]. Later, experimental evidence on the polar nature of NbP was shown by S. Souma, et al. with ARPES results on P and Nb-terminated surfaces with different trials of *in situ* cleaving process [27]. Another important concept introduced in this dissertation is the 'Lifshitz transition' which is a phase transition in the material when there is a continuous change in the Fermi surface topology and it is often called a 'topological Lifshitz transition' when it involves the materials with nontrivial surface topology. A. Lau, et al. did a theoretical study on LaPtBi showing the results on Lifshitz transition under in-plane compressive strain [30]. Furthermore, H. F. Yang, et al. examined NbAs samples by depositing K on freshly cleaved (0 0 1) surface and found the topological Lifshitz transition with change in SS [31]. A. Bedoya-Pinto, et al. have epitaxially grown NbP showing that existence of trivial SS due to dangling bonds [32]. An experiment has been performed

by G. Grabecki, et al. in which Andreev reflection was observed at Pb (>100 nm)/NbP and Nb (>100 nm)/NbP spectra however, the conductance spectra showed the transmission through only small contact region [33, 34].

After a careful literature survey on TWS, the problems were framed towards an experimental study such as how one can get the two different terminations in NbP? How does surface decoration with heavy elements, mainly Pb and Nb (with a large perturbation and large spin-orbit coupling) impact the Weyl semimetal as compared to previously done light element (K) deposition on TWS? What changes appear during the first stage of interface formation at Pb/NbP and Nb/NbP even in a normal state? The dissertation also deals with the problems mentioned earlier. The high-quality NbP crystals were grown by chemical vapor transport (CVT) and studied by ARPES measurements. Different electronic structures of P and Nb-terminations confirmed the polar nature. Later the ultra-thin layers of Pb and Nb were deposited on freshly cleave (0 0 1) surface and the ARPES study showed that one monolayer (ML) Pb deposited on P-terminated NbP causes topological Lifshitz transition whereas 1.9 ML Pb on Nb-terminated NbP showed ordinary Lifshitz transition. The addition of a 0.8 ML Nb on top of P-terminated NbP demonstrated that the Fermi surface is at the critical points i.e. on the edge of the topological Lifshitz transition. After the deposition of 1.3 ML of Nb on Nb-terminated NbP, the ARPES results were blurred due to a disorder introduced in the system.

Chapter 1 of this thesis deals with the introduction of topological semimetals. It comprises a theoretical framework aimed at elucidating the underlying concepts. Various definitions such as signatures of topological semimetals and their fingerprints, charge compensation, Landau level and quantum oscillations, chiral anomaly and topological Lifshitz transition. The second chapter is dedicated to exploring crystal growth and characterization techniques, providing an overview of the history of crystals and their growth processes. The chapter then focuses on the CVT method to prepare $TaAs_2$ and NbP, which are the main points of interest in the thesis. In addition to these materials, other substances such as $ZrAs_2$ are also prepared using the CVT route. Mainly, X-ray diffraction studies have been done to check the correct phase of the materials with crystals structure. Energy dispersive X-ray (EDX) was performed to check the elemental content. Chapter 3 covers the experimental techniques. This chapter is classified into two parts. The first part deals with the low-temperature cryostat and vertical temperature insert systems for the electron transport measurements along with sample preparation, whereas the second part describes the ARPES setup and process. The ARPES measurements were performed at the SOLARIS synchrotron radiation centre, in Cracow, Poland. Chapter 4 provides a systematic discussion of the experimental results obtained and the issues addressed in the $TaAs_2$ case. The chapter

emphasizes the electron transport of $TaAs_2$ with theoretical band structure calculations, which include electron-hole pockets and experimental ARPES results.

Chapter 5 delves into the surface electronic properties of NbP by employing an ARPES study. The study highlights the bipolar nature of *in situ* cleaved NbP crystals and demonstrates the topological Lifshitz transition that occurs when the surface is decorated with Pb and Nb elements. The results of the study are presented in detail, providing a comprehensive analysis of the experimental findings. Finally, the conclusions summarize the key results and their implications for future research in this area.

# 1

# Introduction

*Physics is the most Important*

*Leonard Sosnowski*

## 1.1 Overview of topological materials

An interplay between symmetry and topology is important for understanding electronic phases of matter, from trivial insulators to topological insulators [3]. The dynamic developments in condensed matter theory show that the insulators can be classified into a novel class of quantum materials. In the 1980s, physicists made a ground-breaking discovery showing the two-dimensional system with confined electrons [35, 36]. Such a system subjected to a magnetic field shows the quantum Hall effect because of topological order. It led to dissipation-less edge transport. Later, 3D topological insulators such as $Bi_2Se_3$ also showed a quantum Hall effect due to the existence of metallic surface states which inherit the topological properties from the bulk insulator [37, 38]. For a topological insulator, spin-orbit coupling (SOC) is the factor that should be strong enough to change the electronic structure. The first 3D topological insulator was

realized with $Bi_xSb_{1-x}$ compound and the surface states were mapped using surface-sensitive angle-resolved photoemission spectroscopy [39,40]. ARPES technique involves high-energy synchrotron radiation used to eject the electrons from the crystal. The momentum of the ejected electrons is analyzed as a function of the angle at which the electrons are ejected, and the surface or bulk band structure is determined [41–43].
Another fascinating advancement in topological materials that deserves to be mentioned is topological semimetals. In 1928, Paul Dirac formulated an equation with a 4x4 matrix for relativistic free electrons from which one can look for the origin of spin and charge. Later, Hermann Weyl modified the same Dirac equation by setting the mass term to zero and obtained a new equation with a pair of two massless particles having opposite chirality and known as massless Weyl fermions [21]. Massless Dirac fermions are the overlapped version of two massless Weyl fermions and are protected by time reversal and inversion symmetry. Weyl semimetals are 3D analogous to graphene, where the valence band and the conduction band touch at two discrete points which are called Weyl points (WP). These nodes always come with opposite chirality, acting as monopole and anti-monopole of Berry curvature in momentum space [44]. At these points, Berry flux is quantized to be the net charge of WP enclosed within it. The quantized Berry flux acts as a topological invariant for surface states [45–47]. An extended classification from topological insulators to topological semimetals is shown in Figure 1.1

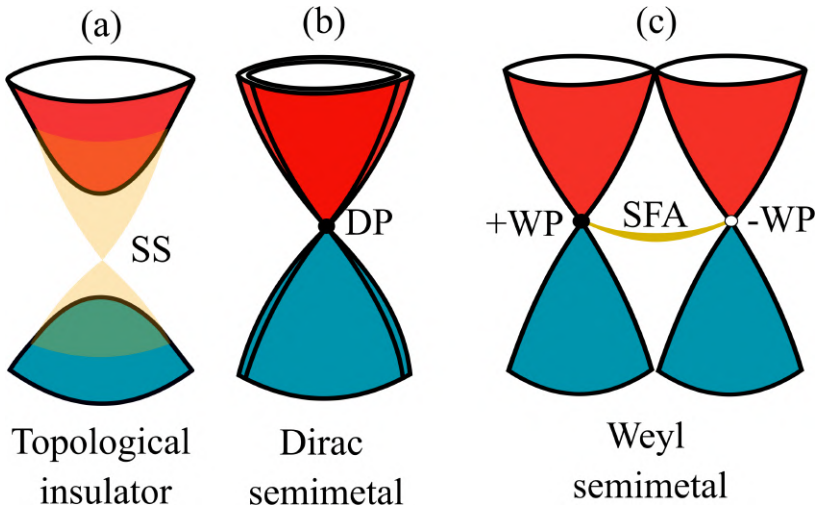


Figure 1.1: Classification of topological materials on the basis of band structure, (a) topological insulator with bulk gap and metallic surface states (SS), (b) Dirac cone with degenerated bands forming Dirac point (DP), (c) two Weyl points (WPs) with opposite chirality connected by surface Fermi arc (SFA).

## 1.2 Topological Weyl semimetals (WSMs)

In the 3D Dirac system, a point degeneracy exists between four energy levels whereas Weyl point has point degeneracy between two energy levels (see Figure 1.1) [48]. To understand the topological characteristics of a Weyl semimetal, let's look into a non-degenerate Weyl cone. This particular Weyl cone has an accidental band crossing between the valence and the conduction band and their point of intersection is called Weyl point [49, 50]. The Hamiltonian describing a single Weyl cone is given as

$$H = \chi.\nu_F(k_x\sigma_x + k_y\sigma_y + k_z\sigma_z) \tag{1.1}$$

here, $\chi$ denotes the chirality which means that the spin and momentum are anti-parallel,
$\nu_F$ is the Fermi velocity,
$\sigma_x, \sigma_y, \sigma_z$ are the Pauli matrices and
$\mathbf{k}$ is the momentum.
From equation 1.1, we know that the momentum and spin are coupled to each other and the dispersion relation is almost similar to graphene [49, 51–53]. Any additional term into it will just shift the points in $\mathbf{k}$ space without opening an energy gap and it is the reason why Weyl points are said to be protected topologically [54]
The Weyl points are strongly related to the surface states and they are

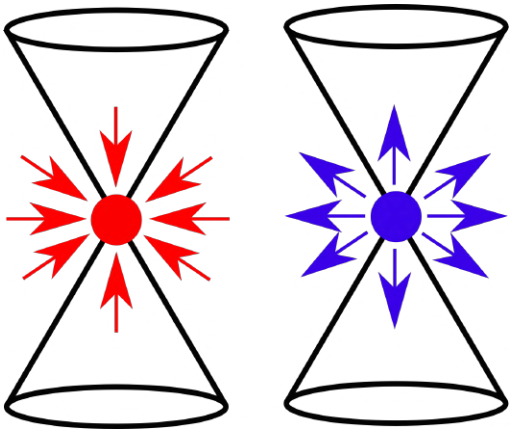

Figure 1.2: Berry flux related to Weyl points of opposite chirality, red color: (sink) and blue color: (source).

topologically protected [22]. As we know that the Weyl semimetal system is gapless, so let's consider the WPs are at $k_x = (0, 0, \pm\chi k_0)$. By considering the fact that when translation symmetry is preserved, it becomes possible to define the three-dimensional Brillouin zone as a stack of two-dimensional

planes, the third component $k_z$ is introduced in the system [49]. The Chern number (topological invariant) is calculated for WPs and given as

$$C_{k_z} = \frac{1}{2\pi} \int_{S_{k_z}} dk \, . \, B(k) \tag{1.2}$$

$$B(k) = \nabla_k \times i \sum_{n}^{filled\ bands} \langle u_n(k)| \nabla_k |u_n(k)\rangle \tag{1.3}$$

Equation 1.3 was obtained by integrating Berry flux over all bands that are filled. Berry flux shows that the Weyl points with opposite chirality act as sink and source as shown in Figure 1.2. Berry flux flows between opposite chirality Weyl cones via time-reversal invariant points. Intermediate planes possess non-trivial Chern numbers, making them topological insulators with protected surface states. Outside the Weyl points the Chern number is zero i.e. there is no existence of the surface states. The Weyl points of opposite chirality always come with a pair. One needs to bring them to the same point in **k** space in order to annihilate them [12].

### 1.2.1 Surface Fermi arcs (SFA)

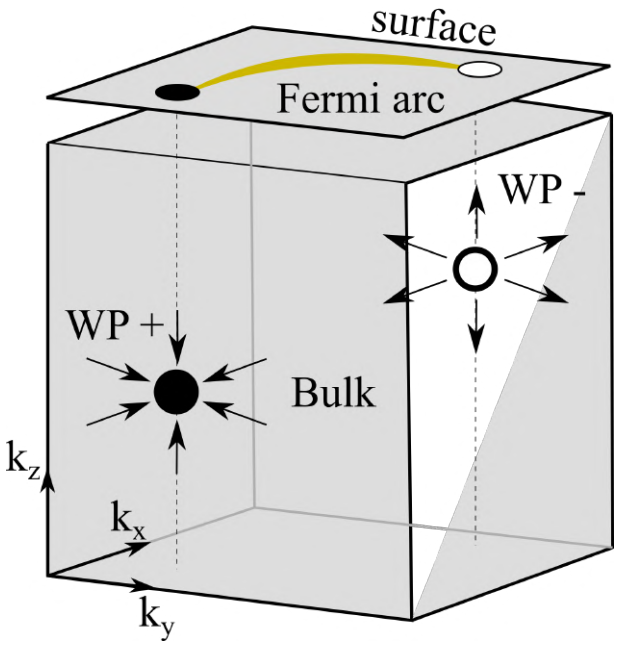


Figure 1.3: The Weyl system in which the Weyl points are protected in the bulk and their surface projection is the Fermi arc.

Bands arise due to surface contribution in Weyl semimetals and stand out as a significant characteristic, even important from an experimental

point of view. When the surface bands intersect with the Fermi energy, they give rise to open Fermi surfaces known as surface Fermi arcs (SFA) or simply Fermi arcs. SFAs are characterized as open lines that connect surface projections of Weyl points (see Figure 1.3) [55].
Mostly, Fermi surfaces are closed contours that act as boundaries between filled and empty states. The existence of open Fermi surfaces may seem contradictory. However, Fermi arcs on two opposing surfaces of a Weyl semimetal complement each other. When combined, they form a closed Fermi surface [56]. As the thickness of a Weyl semimetal is progressively reduced, the Fermi arcs on its surfaces would eventually merge and form a closed Fermi surface also known as a Weyl orbit. This merging occurs due to the increased proximity and interaction between the surface bands as the material becomes thinner [57].

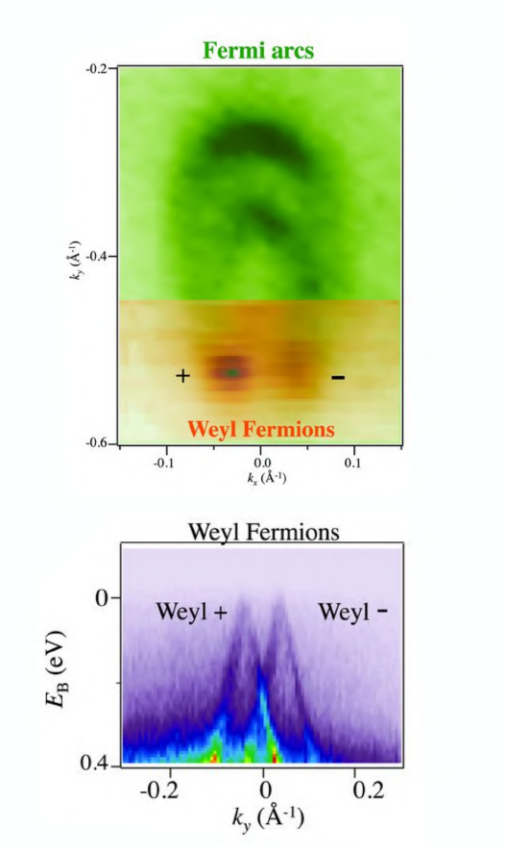


Figure 1.4: ARPES results of TaAs show the Fermi arcs along with Weyl points in the top image whereas the bottom image shows the linear dispersion from the Weyl points, source: [43].

The discovery of Weyl semimetals in 2015 sparked a surge of interest in this field. The initial experimental realization occurred in tantalum arsenide (TaAs) [45], marking a significant milestone. Subsequently, other Weyl

semimetals were also found such as niobium arsenide (NbAs) [46], tantalum phosphide (TaP) [58] and niobium phosphide (NbP) [59]. These experimental findings further expanded our understanding of Weyl semimetals and paved the way for exploring their unique properties and potential applications.
The groundbreaking experiments were conducted to observe Weyl characteristics by using angle-resolved photoemission spectroscopy with synchrotron light or ultraviolet light sources [25]. By employing this technique, researchers were able to gain valuable insights into the unique electronic properties and surface states (Fermi arcs) of Weyl semimetals.

## 1.3 Type II Weyl semimetals

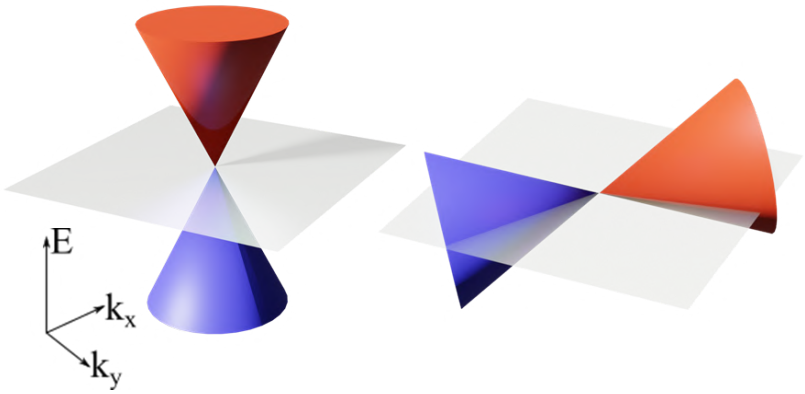


Figure 1.5: The type I and type II semimetals.

Weyl semimetals [22, 48, 60] have linear energy dispersion through the Weyl points in the electronic band structure and display interesting quantum properties, such as the surface Fermi arcs. A. A. Soluyanov et al., introduced type II Weyl semimetal in late 2015 [61], based on calculations performed on the layered transition-metal dichalcogenide $WTe_2$ [62]. This newly discovered type of Weyl semimetal is distinct from the previously known Weyl semimetals, as it exhibits Weyl fermions that emerge at the boundary between electron and hole pockets, rather than having a point-like Fermi surface at the Weyl point. In type II Weyl semimetals the cones are tilted as shown in Figure 1.5 along with the linear dispersion. Right after $WTe_2$ [62], another candidate $MoTe_2$ showed the existence of type II Weyl cones. The $MoTe_2$ family quickly emerged as a type II Weyl semimetal through direct observations. By comparing the calculated band structure of the $T_d$ phase $MoTe_2$ with the experimental structure obtained through ARPES, a notable agreement was found, providing clear evidence of Weyl points originating

from the electron and hole pockets [63]. Furthermore, the absence of Fermi arcs in the centrosymmetric $1_{T'}$ phase further solidified the confirmation of the Weyl semimetallic state in this material [64].

### 1.3.1 Inversion symmetry broken WSMs

Designing materials that may exhibit a Weyl semimetal phase requires considering certain general factors. As discussed earlier, a Weyl semimetal phase can only exist if the product of parity and time reversal is not symmetry. Therefore, it is important to select a material that is close to a band inversion transition and breaks either P or T symmetry. However, unlike in some Dirac systems, the existence of Weyl nodes is coincidental, which makes it challenging to search for them systematically. Moreover, because the band touching can occur at different momentum positions, they can be missed in band structure calculations [65].
A Weyl semimetal phase can be created through a simple mechanism during the band inversion transition between a trivial and a topological insulator, provided that the material's space group lacks inversion symmetry. As the band gap approaches the inversion transition, the material can become either a Weyl semimetal or a nodal line semimetal for a significant range of parameter values, but there is no direct transition between the two insulating states. The symmetry of the space group and the wave vector where the gap closes uniquely determine which possibility will occur. If the material becomes a Weyl semimetal, the number of Weyl node pairs that emerged during the band inversion can range from 1 to 6, depending on the material's symmetry [66].
In the last decade, numerous materials have been predicted and discovered to exhibit Weyl semimetal (WSM) properties through the inversion symmetry breaking mechanism [19], identified TaAs, NbAs, TaP and NbP as materials belonging to the type I class of WSMs explained in the following section. This family of materials is completely stoichiometric and does not require additional doping, external strain, or pressure to fine-tune their state, despite being predicted to have 24 Weyl points. Soon after, TaAs and related materials were observed to exhibit signatures of the Weyl state using ARPES, as reported in the articles [24, 45, 46, 65]. In organizing and understanding the origin of nodes in WSMs, symmetry plays a helpful role. In the TaAs class of compounds, there are 24 Weyl nodes in the band structure, as reported by B. Yan et al [22]. The TaAs structure has two mirror planes $M_x$, $M_x T$ and a (nonsymmorphic) C4 rotation symmetry. A Weyl point with chirality C = 1 can, for instance, be found at $(k_x, k_y, k_z)$ In a single mirror operation, the chirality is reversed, and Weyl points with C = -1 are produced at $(-k_x, k_y, k_z)$ and $(k_x, -k_y, k_z)$. Performing two mirror

operations simultaneously yields a Weyl point with C = 1 at $(-k_x, -k_y, k_z)$. By maintaining the chirality, T generates the four time-reversed partners of these four Weyl points at $(\pm k_x, \pm k_y, \pm k_z)$. By considering the C4 rotation, the eight Weyl points at $(\pm k_x, \pm k_y, \pm k_z)$ result in eight additional partners at $(\pm k_x, \pm k_y, \pm k_z)$ while preserving chirality. The band structure calculations reveal two groups of points, labeled W1 and W2, where W1 is situated in the $k_z = 0$ plane or on the Brillouin zone (BZ) face, and W2 is located at an asymmetric intermediate $k_z$.

## 1.4 Electron transport properties

Electron transport in topological materials shows some extraordinary results such as extremely large magnetoresistance (MR), anisotropic nature of Fermi pockets, ultra-high mobility, pronounced quantum oscillations, chiral anomaly, etc. [66,67]. These features have potential applications in electronic systems mainly in the field of spintronics. Let's look at the concepts one by one as follows.

### 1.4.1 Large unsaturated magnetoresistance

When no magnetic field is present, it is convenient to express the conductivity tensor relative to the crystal symmetry axes. However, when a magnetic field is applied along the $z$-axis, it is more practical to switch to a basis that considers only the field direction. In the ensuing discussion, the notation follows the convention where the first subscript indicates the direction of the current, and the second subscript represents the direction along which the voltage is measured. In cubic or tetragonal systems with the field applied along a principal crystallographic axis, the symmetry allows us to assume only three independent components of the conductivity tensor: $\sigma_{xx} = \sigma_{yy}$, $\sigma_{xy}$ = -$\sigma_{yx}$, and $\sigma_{zz}$. By inverting the conductivity tensor matrix, we can obtain the corresponding components of the conductivity tensor as follows:

$$\sigma_{xx}(B) = \frac{\rho_{xx}(B)}{[\rho_{xx}(B)]^2 + [\rho_{xy}(B)]^2} \tag{1.4}$$

$$\sigma_{xy}(B) = \frac{\rho_{xy}(B)}{[\rho_{xx}(B)]^2 + [\rho_{xy}(B)]^2} \tag{1.5}$$

One of the important characteristics observed in both Dirac and Weyl semimetals is the emergence of large unsaturated MR, which is a measure of

the change in resistance (or resistivity) under a magnetic field, normalized by the resistance (or resistivity) in the absence of a magnetic field which is often expressed as:

$$MR\,\% = \frac{\rho(B) - \rho(0)}{\rho(0)} \times 100\,\% \tag{1.6}$$

The measurements are usually taken in the configuration in which the current direction and magnetic field direction are perpendicular, typically by sweeping the magnetic field from -9 to +9 T. Within this range, there is no saturation observed in topological semimetals. The Lorentz effect is expected to cause a positive transverse MR with a quadratic field dependence in a normal metal [68]. However, this type of MR induced by the Lorentz effect is typically weak and saturates in systems that have a closed Fermi surface. Conversely, topological semimetals display a much larger MR that does not reach saturation. The origin of this abnormally large MR in topological semimetals has been extensively researched, with 'electron-hole compensation' proposed as a possible explanation. In some topological semimetals, it occurs due to zero field backscattering. When the number of holes and electrons are the same in the system, then the magnetic field term dominates $\rho_{xx}$. In this case, $\rho_{xx} \propto B^2$ causes non-saturated MR and is related to electron-hole compensation effect [69]. In the presence of an external magnetic field, at lower temperatures, quantum oscillations can be found in the MR. The next section will explain the details of quantum oscillations.

### 1.4.2 Shubnikov-de Haas oscillations

Electronic properties in topological semimetals are greatly influenced by an external magnetic field. However, additional consequences can arise when the magnetic field is sufficiently strong. When the magnetic field is applied along the $z$-axis to an electron gas confined within a close volume, it leads to the formation of quantized circular orbits in the $k_x$ - $k_y$ plane. Simultaneously, the dispersion along the $z$-axis remains unchanged, preserving $k_z$ as a conserved quantum number. Consequently, the presence of the magnetic field alters the spectrum of the free electron gas and the energy is given as follows:

$$E_n = (n + \frac{1}{2})\hbar\omega_c + \frac{\hbar^2 k_z^2}{2m^*} \tag{1.7}$$

The first term in equation 1.7, refers to Landau levels with Landau index $n$ and cyclotron frequency $\omega_c = \frac{eB}{m^*}$ whereas the second term is the dispersion along magnetic field which remains unchanged. The magnetic field compels the charged particles to move into the cyclotron orbit and eventually, these

particles will return to the point they previously traversed causing an interference. Only constructive interference will be responsible for the quantization of orbits. This quantization is related to the Landau index denoted by $n$ which characterizes the discretization of electron orbit. In this process, tube-shaped states, known as Landau tubes, emerge in the Brillouin zone as shown in Figure 1.6 [70]. In a system with a finite number

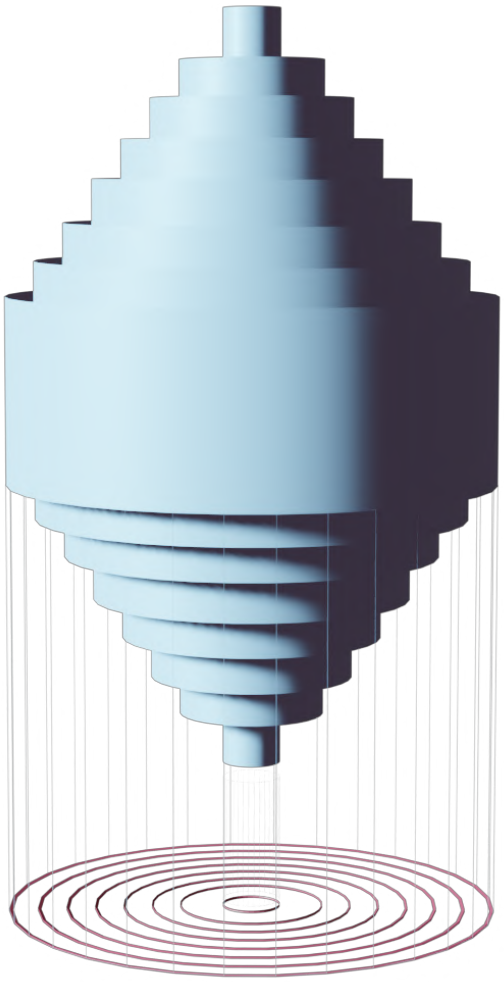

Figure 1.6: Landau tubes and their projection in the form of circular concentric rings in the momentum space in $k_x$-$k_y$ plane.

of electrons, these electrons occupy all available states from zero energy up to a maximum energy level also known as Fermi energy. This occupied level forms a spherical Fermi surface in the $k$ space. As all possible states undergo discretization into Landau tubes, the Fermi surface also undergoes a similar discretization process. However, during this process, the overall shape of the Fermi surface is not affected. The energy of the individual

Landau tube increases with increasing magnetic field and Landau tubes grow. When the Landau tube crosses an area of the Fermi surface that corresponds to an extremal cyclotron orbit, which encloses an extremal cross-section, a notable increase in the material's density of states occurs. As the Landau tubes gradually depart from the Fermi surface one by one, a periodic succession of jumps in the density of states arises. These jumps exhibit a periodicity that is inversely proportional to the applied magnetic field (1/B) and quantum oscillations will be produced [71]. According to Onsager relation, the frequency (F) related to quantum oscillations is related to the cross-section of the Fermi surface (S) given as follows

$$S = \frac{2\pi e}{\hbar} \tag{1.8}$$

The Lifshitz-Kosevich equation provides a detailed description of how various parameters, such as temperature (T), effective mass ($m_* = m/m_0$), and scattering time ($\tau$), influence the amplitude of the oscillations ($A_{FFT}$) and the relation is given as

$$A_{FFT} = \frac{\frac{2\pi^2 k_B T m^*}{Be\hbar}}{\sin\left(\frac{2\pi^2 k_B T m^*}{Be\hbar}\right)} \tag{1.9}$$

here, $k_B$ is the Boltzmann constant, 1/B is the window of the oscillations. Quantum oscillations are widely investigated in topological insulators and topological semimetals [72–74]. It shows that the Landau level quantization is different e.g. energy level in the following equation shows the energy for 2D Dirac fermions in graphene

$$E_n = \nu_F . sgn(n)\sqrt{2e\hbar|B\|n|} \tag{1.10}$$

where $\nu_F$ is the Fermi velocity, n = 0, ±1, ±2, . . . hence the Landau levels are not equally spaces. One of the most remarkable features is the emergence of a field-independent zeroth (n = 0) LL, which becomes locked at the band crossing point ($E_0 = 0$). This unique characteristic is specific to two-dimensional relativistic electron systems. The occurrence of this zero energy state can be explained by considering the Berry phase resulting from the cyclotron motion of carriers in momentum space. The Berry phase is an added phase correction in the quantum system due to the topologically non-trivial nature of the bands present. Obtaining the Berry phase from quantum oscillations is a very convenient method. The presence of band touching points, such as Dirac nodes, leads to a nonzero Berry phase. When subjected to a magnetic field, the cyclotron motion of Dirac fermions, represented by closed trajectories in momentum space, induces a Berry phase that alters the phase of quantum oscillations. In the ideal case of exact linear energy-momentum dispersion, the Berry phase is equal to $\pi$.

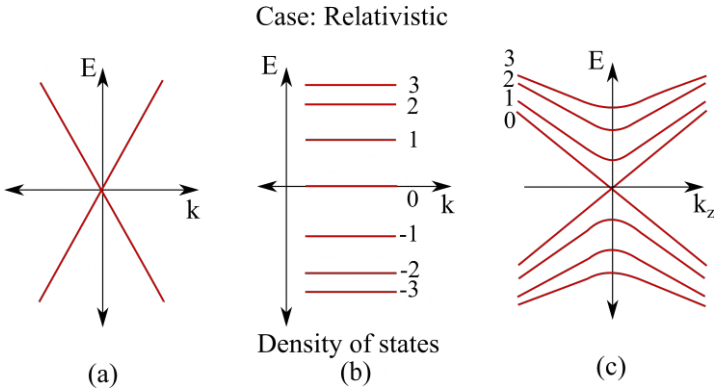


Figure 1.7: (a) The linear energy dispersion in the case of relativistic electrons along with (b) Landau spectra and (c) Landau spectra when an external magnetic field is applied along $z$ direction.

However, this value can shift when the bands deviate from linear dispersion or when the Zeeman effect becomes significant [75].

### 1.4.3 Chiral anomaly

In certain systems, there are points where bands cross each other with a dispersion that differs from the typical quadratic form. Instead, these band crossings exhibit a linear dispersion relation with a fixed relationship between spin and momentum, referred to as "chirality". This linear dispersion is analogous to that of massless Dirac fermions [76]. These special points are known as Weyl points and always occur in pairs with opposite chirality. The spin and momentum are parallel and anti-parallel at a pair of Weyl points. In the normal metal, the dispersion is quadratic whereas, in the case of Weyl semimetals, the dispersion is linear. In condensed matter, chiral

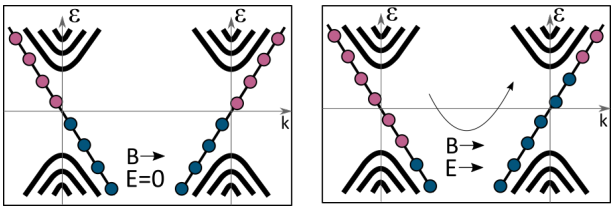


Figure 1.8: Schematic of chiral anomaly showing (left) charge equilibrium, when an applied electric field is zero and (right) charge pumping with the applied electric field when the direction of electric and magnetic fields are parallel.

anomaly leads to unusual transport phenomena, such as negative longitudinal magnetoresistance. There can be many causes that are responsible for negative magnetoresistance in the material such as highly anisotropic magnetoresistance, magnetic effects, current jetting effect in high mobility samples and chiral anomaly [77]. In the case of magnetic materials, the negative MR is caused by spin-flip scattering when the material undergoes a transition [78].
Classically, current jetting effects arise due to improper contact geometry. When a uniform current injection is not applied to a sample, it can lead to an increase in the resistivity tensor perpendicular to the external B field, while the current component in the direction of the B field remains low. This phenomenon is referred to as current jetting, which can result in an uneven distribution of current (as shown in Figure 1.7). If not handled with care, this effect can cause inaccurate values of the longitudinal MR [77]. The figure demonstrates the measurement of longitudinal resistances at

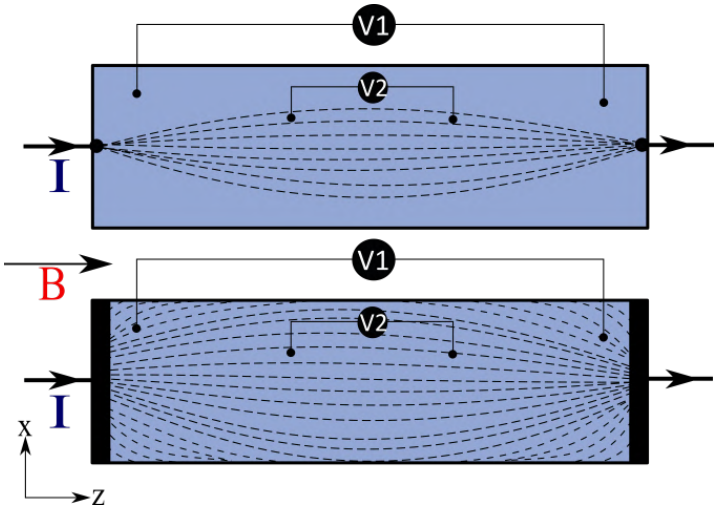


Figure 1.9: explanation of how improper contact geometry can create non-uniform electric currents through the influence of two effects: (top) current jetting effect and (bottom) chiral anomaly.

different voltage probe pairs under the influence of chiral anomaly and current jetting [79]. The voltage V1 and V2 typically decrease with an increase in $B$ field for chiral anomaly effects, whereas V1 decreases and V2 increases with an increase in B due to the current jetting effect. From the figure, it is clear that point-like current injection can cause issues if the voltage-detecting contacts are not located at the same points. For example, in the second subfigure, placing detecting contacts at the edges will result in no voltage difference, leading to a false measurement of no longitudinal resistance. In creating the current jetting effect, the magnetic field-induced resistance anisotropy, $A = \rho_{xx}/\rho_{zz}$, plays a crucial role, where current flow

and $B$ field are in the $z$ direction. This effect can be overcome by careful contact geometry.

# 2

# Crystal growth and characterization

*In a crystal we have clear evidence of the existence of a formative life principle, and though we cannot understand the life of a crystal, it is nonetheless a living being.*

*Nikola Tesla*

## 2.1 Overview and brief history

In nature, the periodic arrangement of atoms holds a secret of evolution. Over the centuries, we have learned that these ordered atoms can be magically transformed into technology. This ordered pattern is called "crystals". It is originated from the Greek word krystallos which means a kind of ice. Crystal is the most commonly encountered solid material state and the building block of technological advancements. In the primeval ages, people were attracted by crystals and used to use them as a symbol of

religion, as lucky charms and as precious gemstones in beautiful ornaments. Later, the curiosity of people towards this field led to an entirely new science called crystal growth.

The scientists attempting to understand the morphologies of mineral crystals produced the earliest significant scientific investigations on the topic of crystal growth. In 1564, a Swiss naturalist Conrad Gesner was one of the early pioneers who reported that the angles and form of the crystals vary in different crystals [80]. Later in the sixteenth century, Andreus Caesalpinus wrote "De Metallicis" which explains the shape of the crystals grown from water solutions such as sugar, salt, etc. Later, a well-known Danish scientist, Neils Stensen became one of the founders of crystallography, he studied the different quartz crystals and observed the fact that quartz crystals are different in appearance from one another but the angle between corresponding faces is the same. Additionally, he observed that the quartz crystal grew by inorganic hydrothermal method. A century later, the French Jean Baptiste Rome´ de l'Isle concluded that every crystalline substance with a specific composition had a similar and particular crystal shape [81].

In the eighteenth century, French physicist Auguste Bravais determined that there are 14 unique types of lattices in three-dimensional crystals which provided a fundamental platform for crystal morphology, crystal symmetry and anisotropy. The science of crystal growth along with its thermodynamics was studied by J. W. Gibbs. An American scientist, Gibbs studied the effect of state variable quantities such as temperature and pressure on various phases in heterogeneous systems which included the first and second laws of thermodynamics. Gibbs's work in this field gave rise to "phase diagrams" which became a prominent source for crystal growth. It allows the selection of appropriate conditions and methods to grow the crystals in a desired composition and stoichiometry. In the early twentieth century, Jan Czochralski introduced a crystal growth technique that revolutionized the production of single crystals for various applications, including semiconductors, metals, salts, and synthetic gemstones. He initially invented this method while working at AEG in Berlin, Germany, and later refined it at the Warsaw University of Technology in Poland. Known as the Czochralski process, it played an important role in the advancement of electronic semiconductor devices and the field of modern electronics. Later, Harold Wilson dedicated his work concerning the velocity of solidification and viscosity of supercooled liquids and another pioneer worked on kinetic molecular theory which played a vital role in molecular beam epitaxy. In 1921, German chemist Max Volmer along with his student I. Estermann proposed a layer-by-layer growth theory in which the adsorption layer lies between the crystal and nutrient phase. They were the first to consider ad-atoms or vacancies in the crystal under non-equilibrium and equilibrium conditions. The work of German physicist W. Kossel and a

Bulgarian chemist Stranski was linked together by a Kossel-Stranski model in which they worked on rock salt structure. In 1958, Jackson worked on the problem of producing many nonmetals from melt-grown crystals. This problem later evolved into solid-liquid interface theory which influenced the field of crystal growth [81].

## 2.2 Classification of crystal growth techniques

Crystals can be grown with controlled parameters such as composition, rate of crystal growth, dimensions, perfections, etc. and the protocols to control physical parameters are underlying in the crystal growth processes. Crystals can be prepared from elements, organic compounds, alloys, inorganic compounds and biological compounds which may be binary or multicomponent. It is a very challenging task to grow high-quality crystals. The best method for growing high-quality crystals relies on the needed size, purity, and capacity to control the defect structure. Crystals can be grown in bulk, ribbons, and thin films or in micro or nanoscale wires from nanometer size to several meter dimensions. The numerous crystal growth methods are available as shown in Figure 2.1. One of the simplest approaches to selecting a particular crystal technique is to classify them by their nutrient phase [82]. Single crystals can grow from a strained solid phase or liquid phase (solution or melt) or vapour phase (sublimation, reaction or condensation). Each technique has its own pros and cons. It depends very much on the elements involved in the process as well as on the system for particular phases of the crystal.

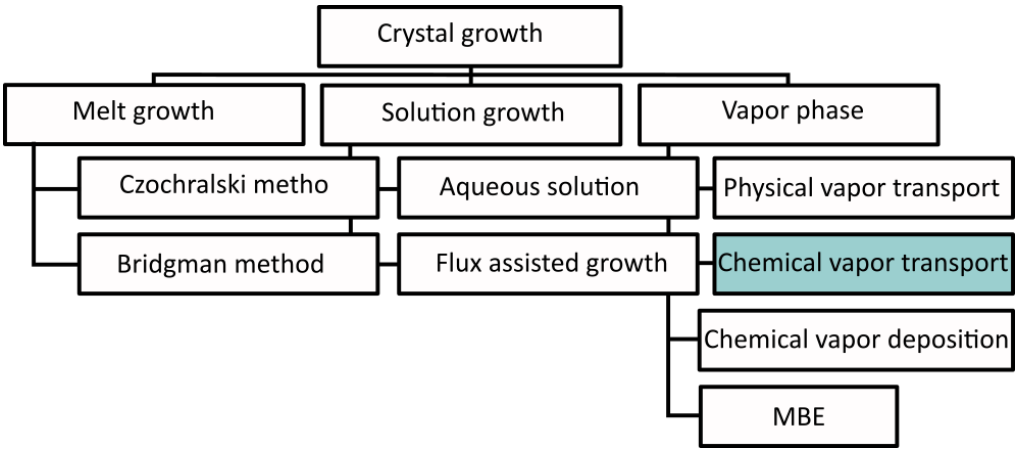


Figure 2.1: Classification of crystal growth techniques based on their nutrient phases.

### 2.2.1 Melt growth

The morphologies and kinetics of the melt growth technique depend on the interface between a crystal and its melt. It is a process of crystallization of the melt when the liquid cools down below its freezing point. This process does not involve any other impurities than the contamination from the crucible and atmosphere. It is more widely used to prepare large single crystals for industrial applications such as electronics and quantum technologies [83]. Czochralski and Bridgman methods are two widely used techniques in order to prepare single crystals from the melt. They can be explained as follows:

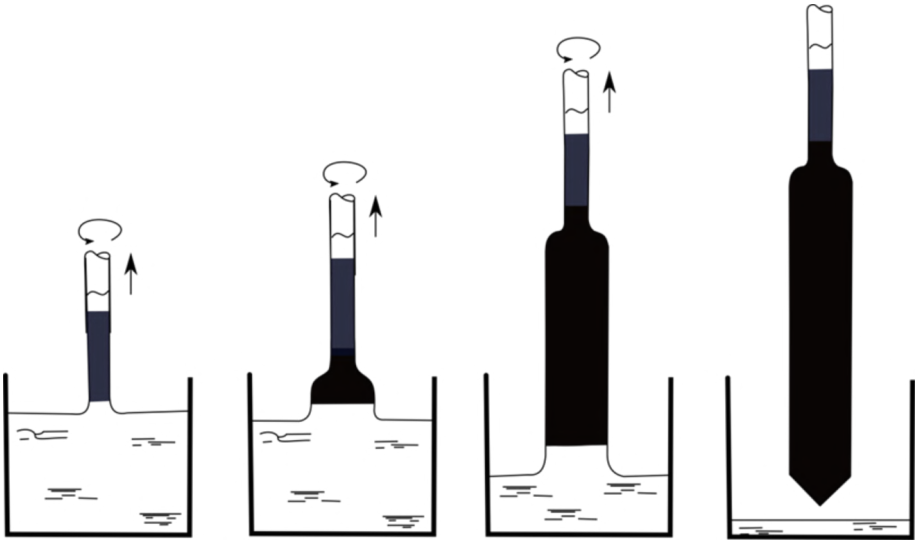

Figure 2.2: Step by step process of Czochralski technique.

The Czochralski technique is a process that involves the small crystal as a seed for growing a large single crystal. This technique is developed in 1916 and named after a Polish scientist Jan Czochralski. It is very useful and vital in semiconductor industries nowadays to obtain silicon and germanium. The Czochralski technique starts by inserting a small seed crystal into a crucible containing melt as shown in Figure 2.2 and then pulling it upward direction with rotations. The temperature of the melt is tuned in such a way that the first part of the crystal grown should have a diameter smaller as compared to a seed. The diameter of the growing crystal can be reduced by increasing the temperature of the melt and vice versa. To obtain the dislocation-free crystals, the diameter of the grown crystal should be less at the first stage and then maintained at about 10 mm, and then increased again to the final target size. The increasing rate of pulling or rate of rotations reduces the crystal diameter and vice-versa. The rate of cooling

depends on thermal conductivity, latent heat of fusion of charge and the rate of cooling. The seed is rotated in order to get uniformity. One of the biggest advantages of this method is that the grown crystal is unstressed because there is no direct contact between the crystal and the walls of the crucible.
Another technique which is also known as the Bridgman method is the most common technique to prepare topological quantum materials such as $Bi_2Se_3$. This method uses a furnace with two zones depending upon the configuration (horizontal or vertical). The hot zone has a temperature above the melting point of the charge and the cold zone has less than that of the melting point. These temperatures are controlled externally [84]. A charge

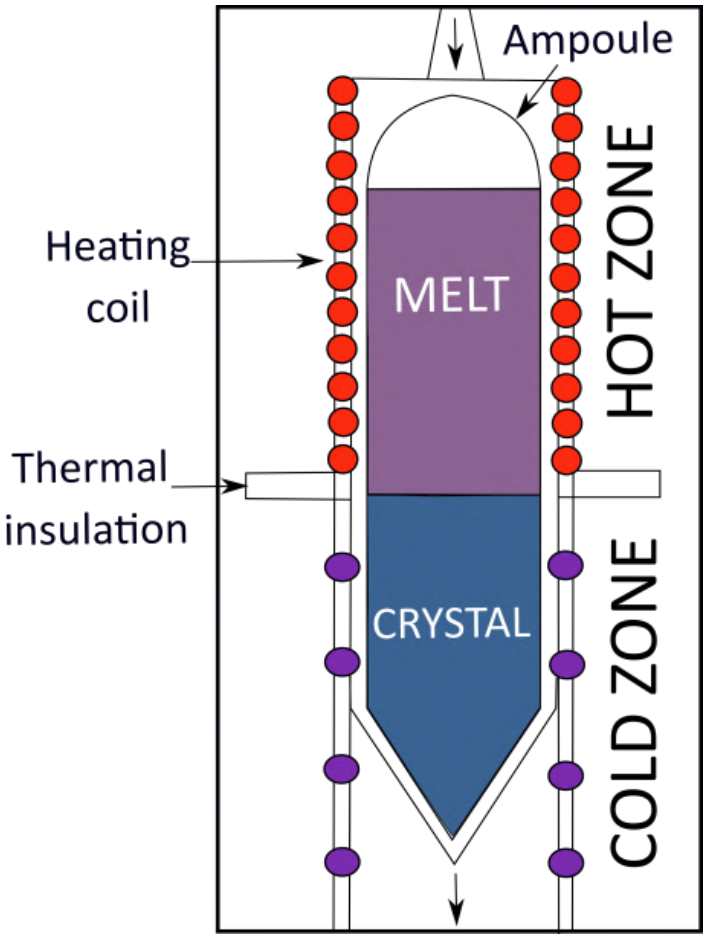


Figure 2.3: A vertical Bridgman system with the two-zone furnace.

(precursor) is loaded with seed crystal within the ampoule or crucible with a narrower end at the bottom and sealed under the vacuum, as shown in Figure 2.3. The sealed ampoule is then placed into the furnace in the hot zone in order to melt the charge and slowly move the ampoule to the cold zone either by moving the ampoule or moving the furnace (depending upon

the facility). Material starts to solidify and a crystal starts to grow as it enters the cold zone. The Bridgman method is simple and cost-effective.

### 2.2.2 Solution growth

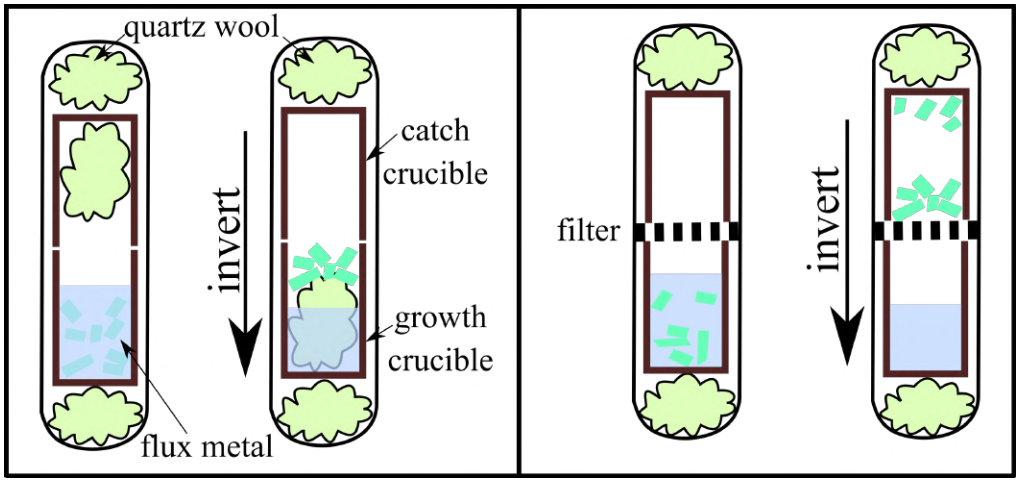


Figure 2.4: High-temperature solution growth in which crystals (green) nucleate and grow and after inversion crystals and flux are separated.

In solution growth technique solvent plays a vital role. There are plenty of solvents available with all suitable properties but water is the most commercially significant. Gallium is the most widely used solvent to prepare Ga-containing compounds such as GaAs. The supersaturation is necessary in order to grow the crystals and can be achieved by either temperature gradient transfer or cooling or solvent evaporation. Crystal grows at the cooler region of the solution [85]. The following relation shows the solute concentration (c) as a function of temperature (T).

$$c = c_0 \exp\left(\frac{-\Delta H_s}{RT}\right) \tag{2.1}$$

Where, $c_0$ is a constant, $\Delta H_s$ is the enthalpy of the solution and T is the temperature.
Another kind of solution growth is high-temperature solution growth which is also known as growth from the flux. In this method, metal fluxes can be used as solvents. A required material is dissolved into flux, and then the solution is heated at a high temperature followed by slow cooling to get the desired composition. Reductants such as In, Ga, Zn, Sn, and Bi are added along with reactants and flux in order to lower the temperature of the process [86]. After the crystal growth process, the flux can be washed

away or removed by a centrifuge machine or inverting an ampoule as shown in Figure 2.4.

### 2.2.3 Vapor phase growth

Physical vapor deposition is the process of depositing thin films and coatings from Angstrom to millimetre thickness. Figure 2.5 shows the process in which atoms are transferred from source to substrate by means of thermal evaporation or e-beam evaporation in a vacuum.

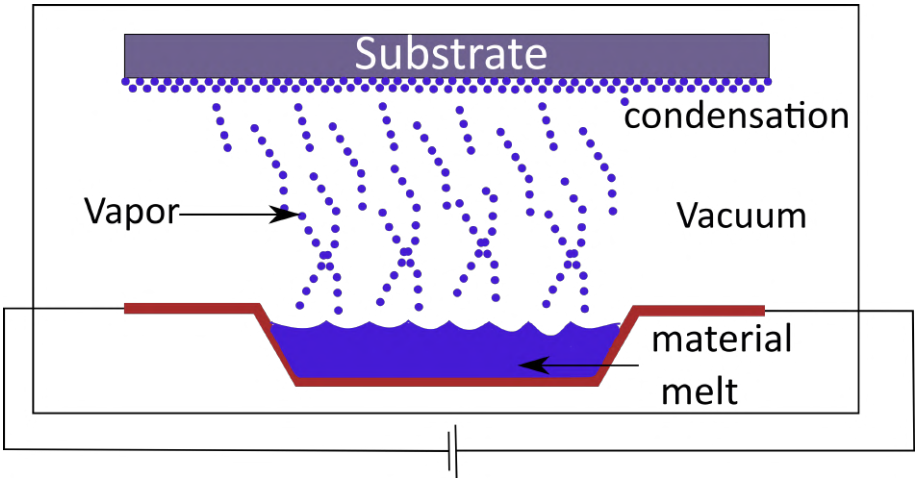


Figure 2.5: Principle of physical vapor deposition technique.

Another technique, chemical vapor deposition (CVD) transports volatile precursors into a reaction chamber via the vapor phase and decomposes on the heated substrate to form layered material or thin films. This technique uses inert gas as well as carrier gases. The preparation of high-quality graphene is one of the most known examples of CVD techniques.
Another kind of vapor growth technique is vapor transport. In which the precursor undergoes the process of sublimation, decomposition sublimation and auto transport with or without a transport agent. The vapor transport technique in the presence of a chemical reagent is called chemical vapour transport (CVT) whereas the physical vapor transport (PVT) method works without a transport agent (see Figure 2.6). A suitable method is chosen based on the physical and chemical properties of the components of the desired compounds. The single crystals grown by using PVT have no contamination with additional elements as well as it has a controlled nucleation and growth process [87, 88].

## 2.3 Chemical vapor transport

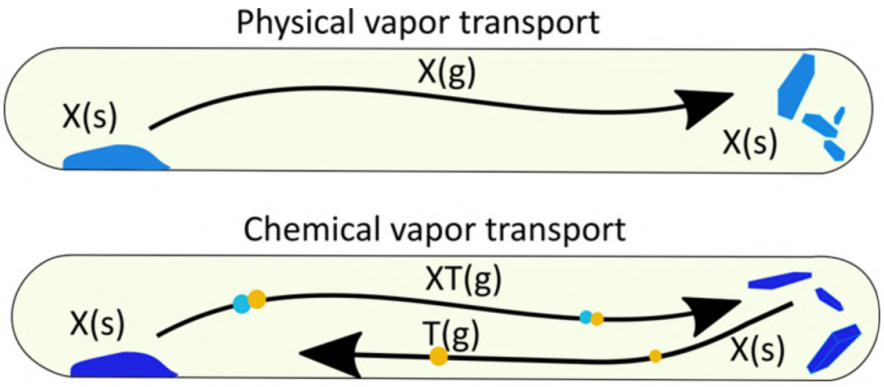


Figure 2.6: Pictorial representation of physical vapor transport (without transport agent) and chemical vapor transport (with transport agent shown by yellow color) processes.

A heterogeneous reaction takes place in the CVT method. A condensed solid phase has no sufficient pressure for its volatilization but a chemical reaction with the transport agent makes them volatile. These gaseous reactants travel under the influence of temperature gradient and crystallize on the other end. A significant development in the CVT process helps to prepare metals, metalloids, chalcogenides, intermetallic phases, pnictide, and more [82]. This chapter will give a detailed idea of the growth process of arsenide and phosphide. CVT process includes the process described below.

(i) Sublimation
The most important factor while considering the CVT process is the transport agent. Usually, iodine is considered the most convenient transport agent. The solid iodine sublimes into gaseous ($I_2$) at 184 °C at sufficiently low vapor pressure inside the ampoule:

$$I_{(s)} \rightleftarrows I_{(g)}$$

(ii) Sublimation decomposition
The gaseous iodine reacts chemically with the precursor in the ampoule. This reaction is governed by the thermodynamics laws. The nature of the reaction is either exothermic or endothermic depending on the precursor. A non-volatile sold precursor is converted into volatile gaseous derivatives:

$$M_{(s)} + I_{(g)} \rightleftarrows MI_{(g)}$$

(iii) Migration
The vacuum-sealed quartz ampoule is kept under the influence of temperature gradient. This temperature gradient is the driving force for the gaseous derivatives to migrate from one zone of temperature to another zone with different temperatures. The migration happens based on the thermodynamic reactions. If the reaction is exothermic then the gaseous derivatives will migrate from the cold zone to the hot zone whereas endothermic reaction drives them towards the cold zone

(iv) Crystallization
The migrated gaseous derivatives form the crystals in the crystallization zone and gaseous iodine goes back to react with the precursor and the process continues and single crystals grow in the crystallization zone.

**Why we used the chemical vapor transport process and what is the role of the transport agent?**

Single crystals of transition metal phosphides and arsenides are usually grown by using chemical vapor transport. Because tantalum (niobium) has a very high melting point of about 3020 °C (2469 °C) and arsenic (phosphorus) has a low sublimation temperature of 615 °C (∼460 °C). Also, these compounds TaAs (NbP) do not melt up to 1400 °C. These facts made the synthesis of such compounds difficult. Hence CVT method proves itself very useful for growing such kinds of crystals. Transport agent plays a significant role in the CVT process. It chemically reacts with precursors and helps them to form crystals on the other ends of the tube [89].
Metal halides are the central choice as transport agents due to volatility. Elemental halogens such as chlorine, bromine and iodine are usually suitable for the process on the other hand, fluorine is not suited because fluorides form at extreme equilibrium positions. We have used iodine as a transport agent. Gaseous iodine reacts with the precursor and forms volatile metal iodides as well as arsenic (phosphorous) iodides. Tri-iodides of arsenic are more stable than phosphorous iodides. During the reaction of iodine with solid precursor form gaseous iodides with four types of reactions which determines the transport of volatile derivatives and given as follows:

| No. | Type of reaction | Transportation |
|---|---|---|
| 1 | Highly endothermic | no transport possible<br>(no formation of effective pressure) |
| 2 | Endothermic | transport from hot zone<br>to cold zone |
| 3 | Highly exothermic | no transport possible<br>(no back reaction can take place) |
| 4 | Exothermic | transport from cold zone to hot zone |

Table 2.1: The type of reactions involved in the CVT process and where crystallization takes place

### 2.3.1 Tantalum di-arsenide ($TaAs_2$)

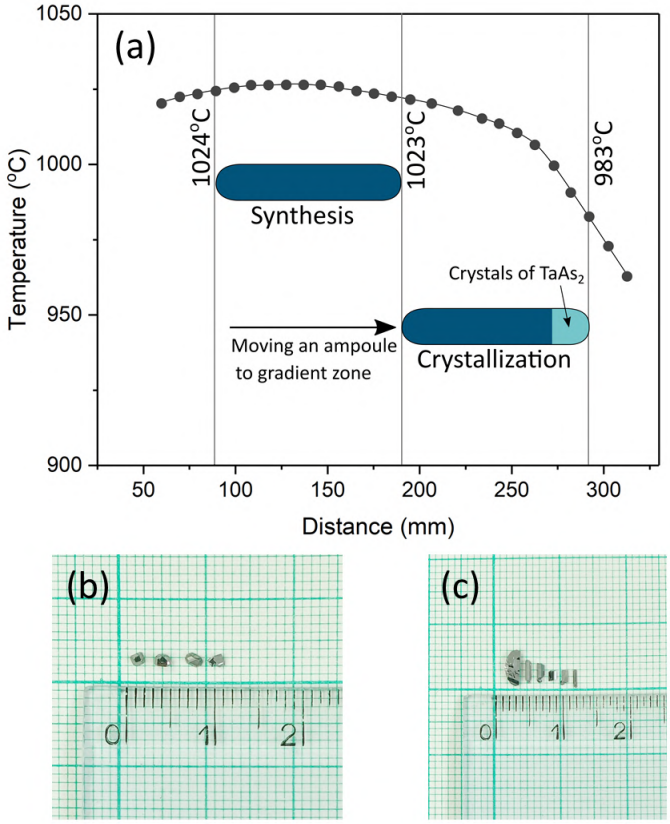


Figure 2.7: One step growth process of $TaAs_2$ single crystals, (a) temperature gradient with ampule position, (b) single crystals of TaAs and (c) single crystals of $TaAs_2$.

In this chapter, we mentioned two ways of growing $TaAs_2$, one and two-step processes. Initially, we used the one-step process to prepare $TaAs_2$

single crystals. In this process, we used tantalum foil (Zr Industrial Ltd, 99.99%) and cleaned arsenic (PPM pure metals, 99.999995%) inside the ampule. Iodine was chosen as a transport agent for this process and loaded along with Ta and As precursors to the ampoule. In the beginning, the ampoule was kept in the furnace at a constant temperature of (1024 °C)for a week and then then the ampule was slowly moved from the constant temperature zone to the gradient zone (about 0.5 cm per 2 h). One end of the ampule was at $\sim$ (1023 °C) whereas the other end was at (983 °C). We let the ampule stay at this gradient for about 13 days. Under the influence of the temperature gradient, the polycrystalline material synthesized during the synthesis process started preparing $TaAs_2$ crystals at a lower temperature zone.
After the process, we cooled down the furnace to room temperature and obtained shiny and long crystals of $TaAs_2$ (Figure 2.7 (c)), we also obtained small crystals of TaAs as shown in Figure 2.7 (b).

1. Synthesis of polycrystalline $TaAs_2$
   The recipe for preparing single crystals of $TaAs_2$ is given as follows: poly-crystalline $TaAs_2$ is prepared by using a very simple method. Tantalum foil (Zr industrial Ltd, 99.99 %) and As (PPM pure metals. 99.999995 %) is used as a precursor and loaded in the quartz tube (ampoule) and sealed in a vacuum (see Figure 2.8). The evacuated ampoule is then kept in the furnace at 990 °C temperature for 19 days. At the end of the process, we cooled down the furnace and obtained $TaAs_2$ poly-crystals.


Figure 2.8: Synthesis of polycrystalline $TaAs_2$: a vacuum-sealed quartz ampoule loaded with tantalum foil and arsenic.

2. Single crystal growth of $TaAs_2$
   We prepared pellets of previously synthesized polycrystalline $TaAs_2$ and then loaded them in the quartz ampoule along with the transport agent iodine. The ampoule is sealed under the vacuum. The sealed ampoule is then kept inside the furnace under the influence of temperature gradient. The source zone temperature was kept at 1025 °C whereas the sink zone was kept at 956 °C for 23 days (shown in Figure 2.9). After, the furnace was cooled down to room temperature at the rate of 100 °C/hour. At the end of the process, the shiny crystals as in Figure 2.10 were grown in the ampoule in the growth zone.

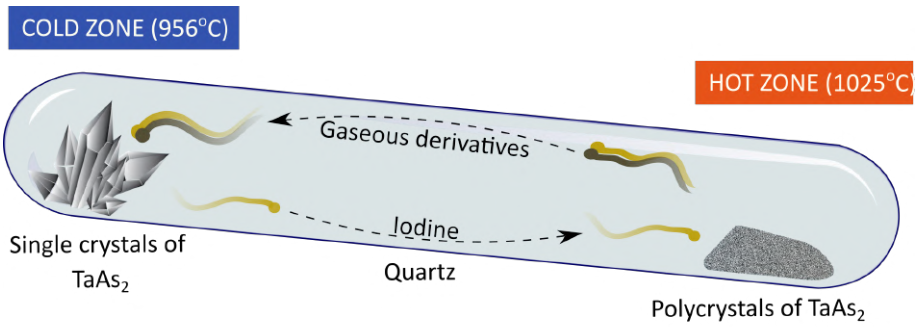


Figure 2.9: Quartz ampoule representing the CVT reaction in which single crystals of $TaAs_2$ grow at a cool zone.

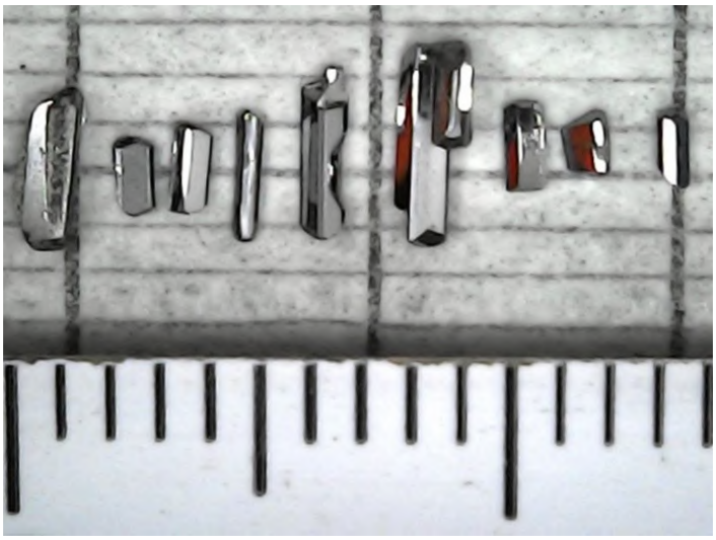

Figure 2.10: $TaAs_2$ as-grown crystals in millimetre size.

### X-ray diffraction and EDX of $TaAs_2$

One can describe $TaAs_2$ crystal structure by the monoclinic unit cell and C2/m (space group No. 12), which can be easily recalculated to the body-centered I2/m space group. The structure of our crystals was confirmed by X-ray powder diffraction using a Rigaku SmartLab 3 kW diffractometer equipped with a tube having Cu anode, and operating with U = 40 kV and I = 30 mA. The characteristic peak positions were identified using PDXL software and data from International Center for Diffraction Data as shown in Figure 2.11, powder diffraction file PDF-4+2018 RDB database (database card number: 04-003-3007). The lattice constants determined for our crystal are $a = 9.343445(12)$ Å, $b = 3.386195(4)$ Å, $c = 7.76195(9)$ Å, $\beta = 119.7065(6)°$ and $V = 213, 303(5)$ Å$^3$. The single crystal orientation

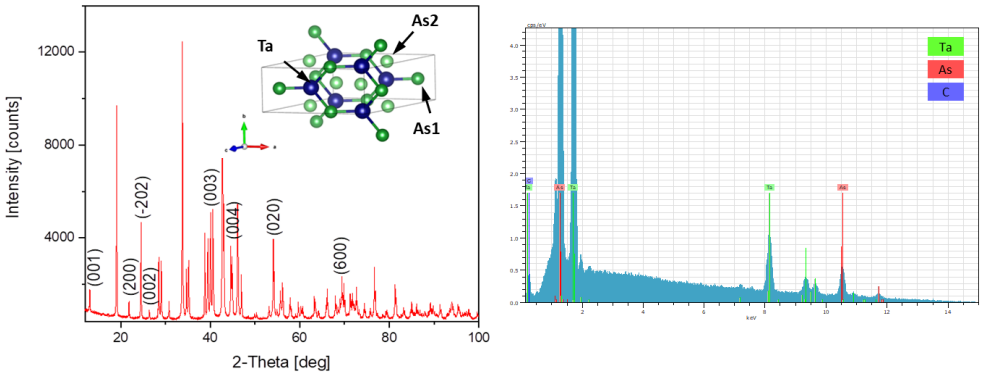


Figure 2.11: Powder X-ray diffraction spectra of $TaAs_2$ with several peaks, (inset) shows the unit cell of the crystal structure with Ta atoms (blue color) surrounded by As1 and As2 (dark green and green color resp.) and EDX spectra showing $TaAs_2$ stoichiometry indicated by green color for Ta and red for As.

was performed on a KUMA-diffraction four-circle diffractometer with a goniometer in kappa geometry. The radiation of the Cu lamp and the peak-hunting procedure were used. In a conventional unit cell of $TaAs_2$, each tantalum atom is surrounded by six arsenic atoms, out of which three are As1 and the remaining three are As2. EDX spectra show the stoichiometric peaks of Ta and As (see Figure 2.11)

### 2.3.2 Niobium monophosphide (NbP)

In the beginning, we considered the fact that transition metal Nb has a high melting point (2477 °C) and chemically active phosphorous has a low sublimation temperature. A fully safe and controlled process has been set up in order to avoid creating excess pressure and the explosion of ampoules. A setup consists of a two-zone furnace with a synthesis zone temperature of 800 °C while the phosphorous zone at 460 °C. Polycrystalline NbP is prepared by loading a stoichiometric amount of Nb powder (Alfa Aesar, 99.99 %) in the form of compressed pellets of 10 mm diameter and red phosphorous (Heranes, 99.999 %). The ampoule is sealed under the vacuum and placed in the two-zone furnace with the appropriate position for 80 hrs. The synthesis process took place from 800 to 850 °C. The black-colored polycrystalline powder was obtained after finishing the process. The phase purity of the synthesized polycrystalline material was analyzed by using the X-ray diffraction method and the desired phase was confirmed.

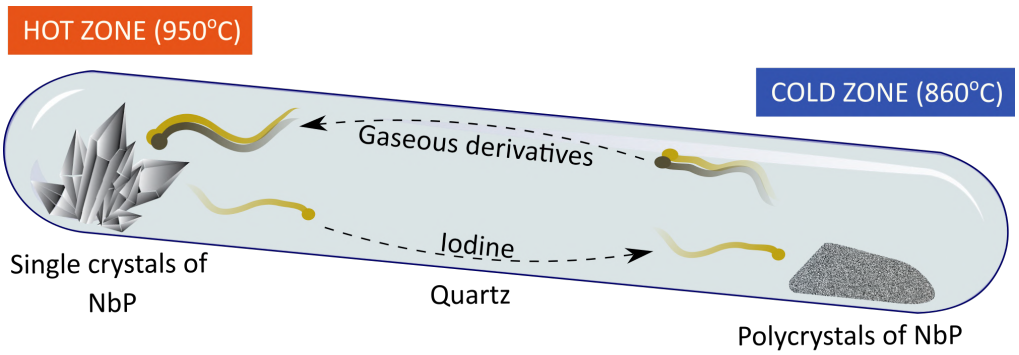


Figure 2.12: Chemical vapor transport reaction process which forms the crystals at the hot zone of the furnace.

$$NbP_{(s)} + 4I_{2(g)} \rightleftarrows NbI_{5(g)} + PI_{3(g)} \tag{2.2}$$

Above chemical reaction helps us to understand the growth process of single crystals. As it is a bidirectional reaction, the thermodynamics of the reaction between the transport agent (iodine) and solid precursors will determine whether the reaction is endothermic or exothermic. The gaseous derivatives $NbI_5$ and $PI_3$ migrate from the cold end to the hot end under the influence of temperature gradient, it is said to be the exothermic reaction. We used NbP polycrystals as a solid precursor.
Polycrystalline NbP was compressed and prepared pellets of diameter 10 mm. Those pellets were then loaded in the ampoule (inner diameter = 16 mm, length = 210 mm) along with iodine (10 $mg/cm_3$). After the ampoule is evacuated and placed in the two-zone furnace with a source zone temperature of 850 °C and growth zone temperature of 950 °C for two weeks and then the furnace was cooled down to room temperature with a cooling rate of 100 °C/hour. The shiny double trapezoidal-shaped crystals were grown 950 °C as shown in Figure 2.13.

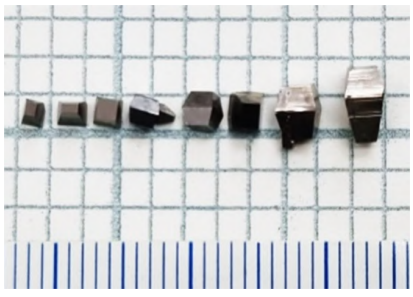

Figure 2.13: Millimetre-sized single crystals of NbP.

### X-ray diffraction and EDX of NbP

As grown NbP crystals were structurally analyzed by Rigaku SmartLab 3kW diffractometer operating with I = 30 mA and U = 40 kV. International Centre for Diffraction Data (ICDD) is used to identify characteristic peaks position (Data Base card number: 04-003-0878). All the measurements were taken along [0 0 1] direction. The single crystal orientation was performed on a KUMA-diffraction four-circle diffractometer with a goniometer in kappa geometry. The lattice constants determined for our crystal are $a = 3.335\,44(6)$ Å, $c = 11.3782(3)$ Å, $V = 126.584(4)$ Å$^3$ with the tetragonal crystal structure as shown in Figure 14 (a, b) (space group 109). Quantitative chemical composition was investigated by using the EDX system QUANTAX 400 Bruker coupled with the Zeiss Auriga field-emission (Schottky-type) scanning electron microscope in order to determine the stoichiometry (see Figure 2.14).

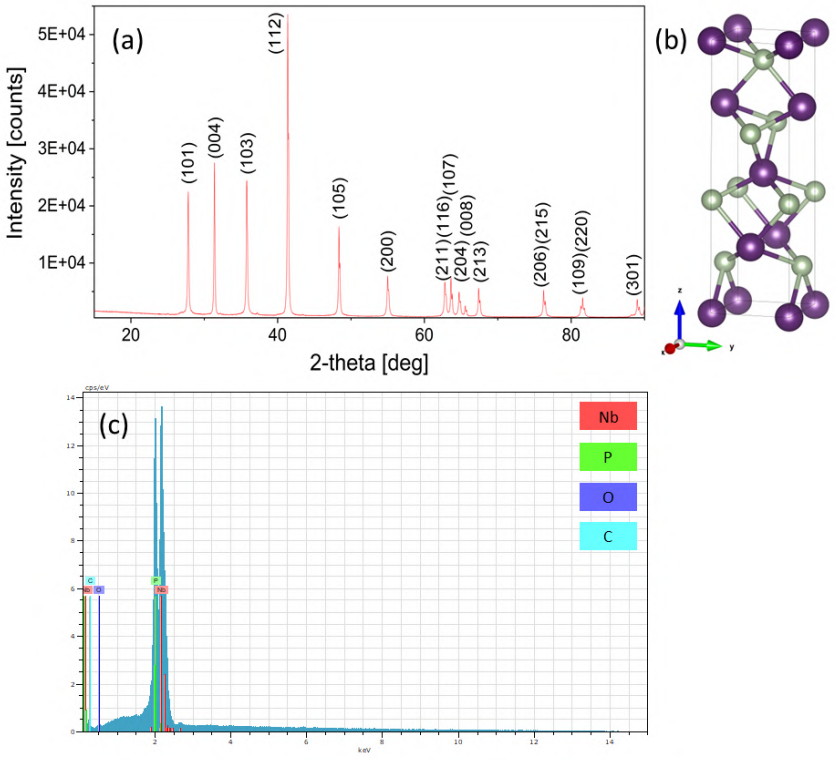


Figure 2.14: (a) XRD spectra of NbP showing different peaks, (b) unit cell of tetragonal NbP grown along [001] direction and (c) EDX graph of Nb and P peaks showing the stoichiometry.

**TEM study of NbP**

The transmission electron microscopic study has been done on NbP single crystals lamella cut from the single crystal by using the focused ion-beam method. As shown in Figure 2.15, the ordered arrangements of the atoms are in good agreement with the crystal structure shown above. The high-angle annular dark field (HAADF) profile shows the polarity profile in which two intense peaks signify the position of Nb atoms in the lattice.

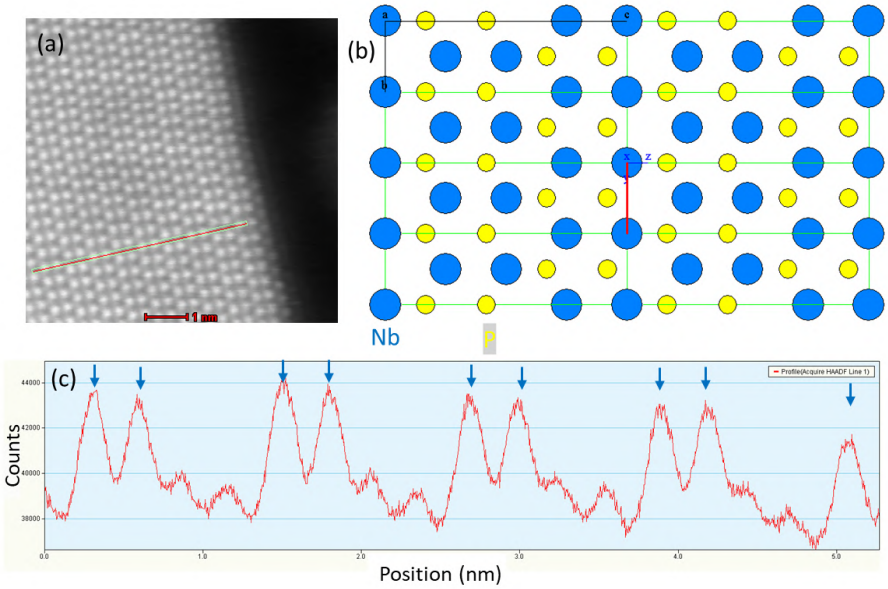


Figure 2.15: (a) Transmission electron microscopic image showing an ordered arrangement of NbP indicated by a line, (b) side view of extended crystal structure in which Nb atoms are shown by blue color whereas P atoms are indicated by yellow color and (c) the high-angle annular dark field (HAADF) profile showing the presence of Nb atoms by two high peaks as in agreement with the crystal structure.

### 2.3.3 Zirconium di-arsenide ($ZrAs_2$)

After the remarkable discovery of Weyl semimetals, new materials have entered in the family of quantum materials known as nodal line semimetals. Zirconium di-arsenide is one of the examples of nodal line semimetals with butterfly-shaped surface states. The single crystals of $ZrAs_2$ were prepared by using the CVT technique. A safe synthesis process was done in two

zone furnace where an evacuated ampoule was loaded with Zr pellets at about 800 °C and kept at 460 °C with a small amount of iodine for 7 days. Synthesized polycrystals were taken and loaded with iodine into a quartz ampule and sealed under a vacuum. An ampoule was kept in the gradient zone of 700 °C (cold end) and 800 °C (hot end) for 21 days. After 21 days the furnace was slowly cooled down to room temperature and shiny needle-like crystals are obtained as shown in Figure 2.16.

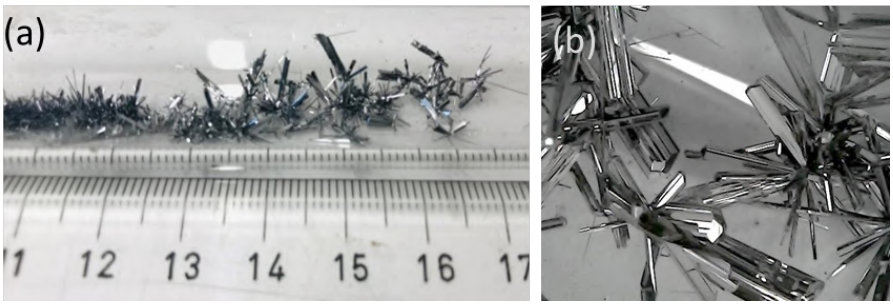


Figure 2.16: Single crystals of $ZrAs_2$ (a) as grown in an ampoule, (b) magnified optical image of the long rod-shaped crystals.

### X-ray diffraction of $ZrAs_2$

X-ray diffraction analysis was done on the samples in order to know the structural details. The single crystals of $ZrAs_2$ have an orthorhombic crystal structure and belong to space group no 62. All the details about the X-ray diffractometer are the same as mentioned in the NbP X-ray diffraction section. The investigate lattice constants as $a = 6.80261(10)$ Å, $b = 3.68926(5)$ Å, $c = 9.03115(13)$ Å, $V = 226.651(6)$Å$^3$. The experimental data were compared with database ICDD (PDF-4+ 2020 RDB) 01-079-6540 (see Figure 2.17)

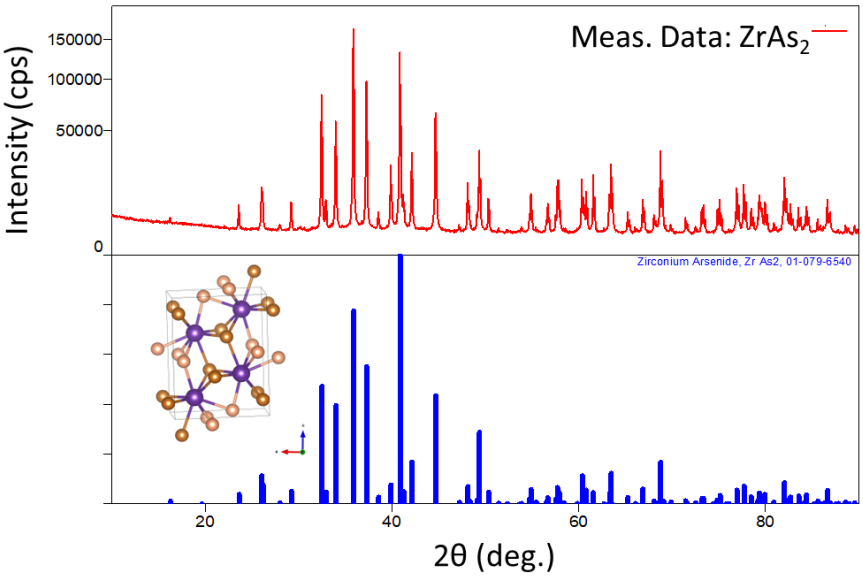


Figure 2.17: X-ray diffraction data compared with database card number ICDD (PDF-4+ 2020 RDB).

*** Electron transport and ARPES studies are currently in progress and are not included in the dissertation.**

# 3

# Experimental techniques

*"A method is more important than a discovery since the right method will lead to new and even more important discoveries."*

*Lev Landau*

## 3.1 Experimental setup of the cryostat

This section concerns the experimental setup used in low-temperature electron transport measurements as well as the experimental ARPES setup along with the sample preparation technique.
All electron transport measurements were carried out in the custom-made liquid nitrogen-shielded helium cryostat which was fabricated in the cryogenic workshop of the Institute of Physics, Polish Academy of Sciences, Warsaw. The liquid helium chamber is surrounded by a liquid nitrogen reservoir in the upper toroidal volume in order to reduce the evaporation of liquid helium. The lower part of the liquid helium chamber is surrounded by a copper screen connected to a liquid nitrogen reservoir.

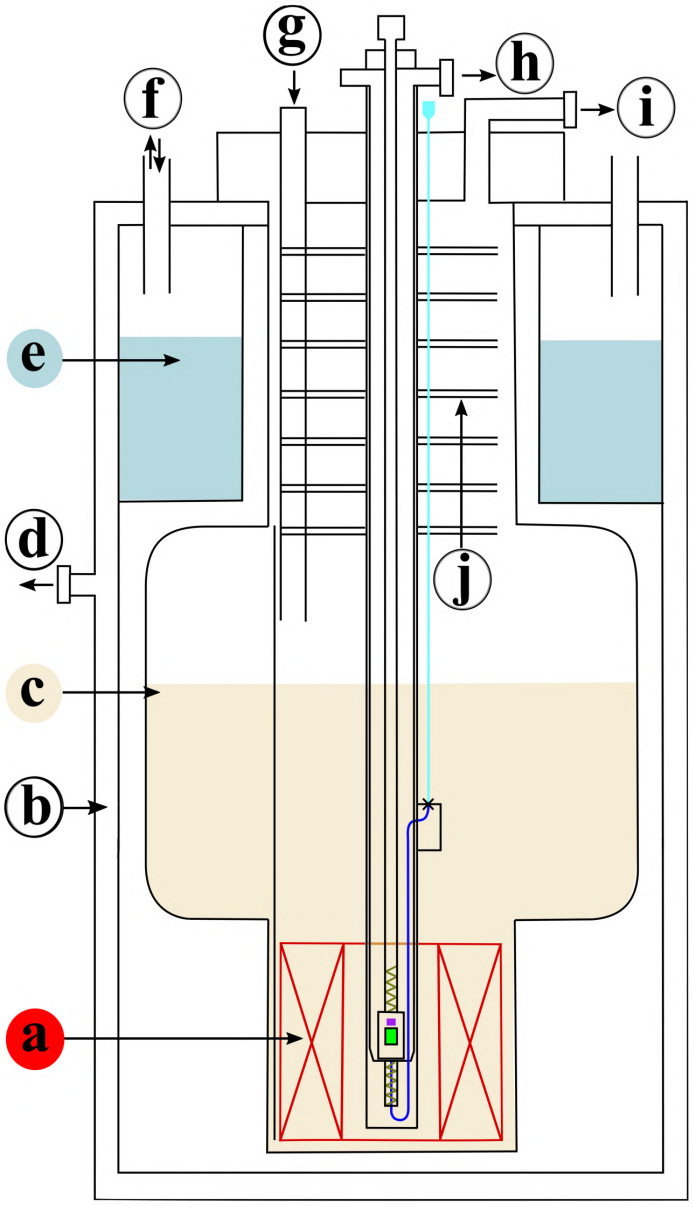


Figure 3.1: Schematic of cryostat labeled as follows: (a) superconducting coil magnet, (b) vacuum jacket, (c) liquid helium level, (d) evacuation valve, (e) liquid nitrogen reservoir with liquid nitrogen, (f) nitrogen chamber outlet, allowing nitrogen to be evaporated freely, (g) helium chamber outlet for inserting transfer tube, (h) sample chamber outlet connected by a helium recovery pump, (i) helium chamber outlet permanently connected to helium recovery and (j) baffles working as screens.

Figure 3.1 shows all the significant parts of the system. The main chamber is called a helium reservoir. The superconducting magnet (red color) is

placed at the bottom of the helium reservoir. As this coil is made of a superconducting wire, it is obligatory to maintain the liquid helium level above the superconducting coil during the measurements.
The helium chamber over the superconducting coil allows the accumulation of a larger stock of liquid helium hence the chamber is surrounded by a tight vacuum jacket to eliminate heat input by conduction. To reduce the amount of heat supplied through radiation, a copper screen cooled by a liquid surrounds a major portion of the helium bath. In order to insert the variable temperature insert (VTI) of the cryostat, a gap needs to be present at the top of the copper screen. To compensate for this gap, a series of metal flanges are utilized in the area, which forms a set of anti-radiation screens. These screens have progressively decreasing temperatures.

### 3.1.1 Variable temperatures insert (VTI)

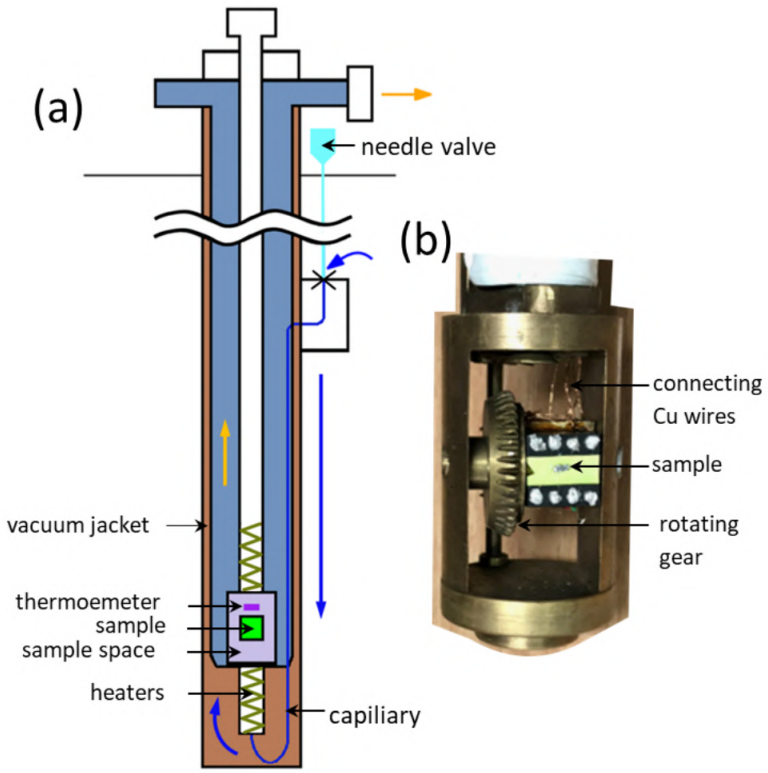


Figure 3.2: (a) Schematic of vertical temperature insert used in the helium bath cryostat, (b) rotational probe used in the experiments to rotate the sample.

Precise temperature control requires effective thermal insulation from the

surroundings, as well as a balance between heat input and dissipation. Here, we used variable temperature insert which is another important element in this system. To provide the required insulation, an additional vacuum jacket is employed. The temperature control system comprises a coolant supply (helium pumped through a capillary), temperature sensing (thermometer at the sample), and a feedback system (PID stabilization) that regulates the heating output (from heaters on the handle and inside the insert). This setup allows for precise temperature stabilization and adjustment. By using the helium pumping system, the temperature can be lowered to as low as 1.5 K, compared to a minimum temperature of approximately 4.2 K without the pumping system, depending on the efficiency of the pumping process and the cross-sectional area of the pipes leading to the pump.
Bifilarly wound manganin wires with a resistance of 50 Ω each are placed symmetrically above and below the sample to compensate for any temperature gradient, serving as radiators. The thermal insulation enables the system to operate at temperatures up to 300 K. Figure 3.2(a) The sample mounted on this kind of probe is fixed at a position facing upward direction. Another probe that was used during the experiments is a rotational probe (see Figure 3.2(b)). The rotational probe allows the sample to rotate till 120° with respect to the magnetic field enabling us to take angle-dependent measurements on the sample to probe the Fermi surface cross-section.

### 3.1.2 Sample preparation for electron transport

Sample preparation is the most fundamental stage to characterize the sample at low temperatures. Single crystals of $TaAs_2$ (2 mm × 0.7 mm × 0.5 mm) which have longer direction along the $b$ axis are used for electron transport measurements. Six contacts were made in a Hall bridge configuration with the help of 50 $\mu$m gold wires and silver paint epoxy (as shown in Figure 3.3. Silver paint was used to avoid peculiar superconducting effects due to alloy formation. The prepared samples of $TaAs_2$ were measured in a cryostat as described in 3.1 is capable of producing magnetic fields up to 9 Tesla by using a superconducting coil. VTI used can control the temperature on the sample from 1.5 to 300 K. We have used AC electrical measurements with the acoustic frequency with constant sample current applied along [0 1 0] and measured voltages by using Stanford research SR 830A lock-in amplifiers. All the contacts were ohmic in the regime.

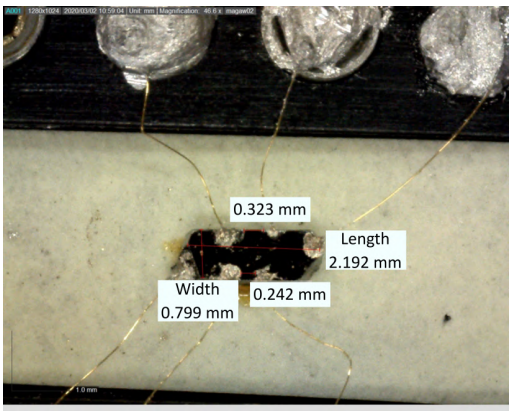


Figure 3.3: Hall bridge type contact geometry shown on $TaAs_2$ single crystal.

## 3.2 Angle resolved photoemission spectroscopy (ARPES)

In the past decade, topological materials showed their unusual electronic properties. These properties arise mainly due to surface band structure and metallic surface states. Hence, the techniques which probe the electronic structure of these materials are essential in fundamental condensed matter research. ARPES is one of the most powerful surface-sensitive techniques based on the principle of the photoelectric effect used for characterizing materials [24]. The photoemission was detected by Hertz in 1887, later the experiment was refined and the concept was explained systematically with quantum mechanical support in 1905. In this process, the incident photons with energy $h\nu$ are absorbed by the electrons in the sample and when the energy of absorption is greater than the work function ($\phi$) of the material then the electrons emit out of the material in all spatial directions. Emitted electrons are called photoelectrons (see Figure 3.4). A photoemission spectrometer is used to collect the fraction of photoelectrons as a function of their kinetic energy and emission angles ($\theta$, $\phi$) where $\theta$ is the polar angle in reference to surface normal and $\phi$ is the azimuthal angle with respect to experimental geometry [65].

$$E_{kin} = h\nu - \phi - E_B \tag{3.1}$$

$$\hbar k_{\parallel} = \sqrt{2mE_{kin}} \sin\theta \tag{3.2}$$

Here, $\phi$ = work function (minimum energy required to remove the electron from solid to the vacuum outside the surface of the sample), $E_B$ = binding energy, $\hbar k_{\parallel}$ = electron's crystal momentum parallel to the surface which

is conserved in the entire photoemission process. Experimentally, all the ARPES data are plotted as a function of binding energy hence easiest way to convert the kinetic energy to binding energy is

$$E_{kin} - E_F = -E_B \tag{3.3}$$

$E_F$ = Fermi energy.

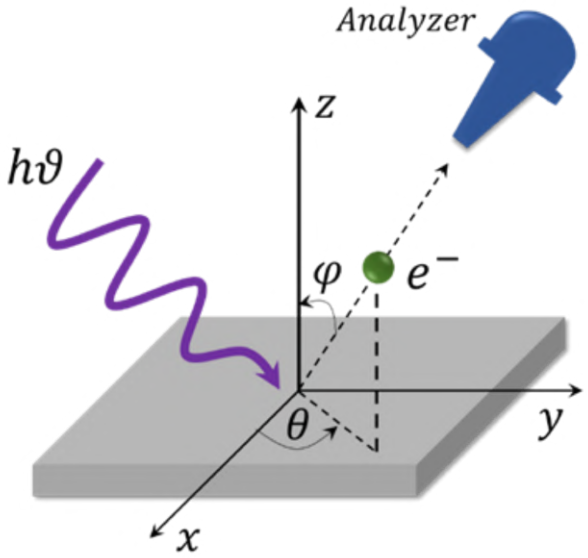


Figure 3.4: The schematic explaining the fundamental principle of ARPES with an incident photon of energy $h\nu$ which knocks off the electron out of the solid.

### 3.2.1 Ultra-Resolved Angular Photoelectron Spectroscopy beamline, URANOS (former UARPES)

All the ARPES measurements were performed at the SOLARIS synchrotron radiation centre, Cracow (Poland). The beamline, currently known as URANOS (formerly UARPES), helps to visualize the electronic band structure of topological quantum materials describing photo-emitted electrons outside the given material. Synchrotron beam is controlled and focused by optical elements described as follows

**Undulator**: elliptically polarized quasiperiodic APPLE II type undulator with magnetic period length 120 mm is used as a source.

**Monochromator**: selects one particular wavelength from the entire spectra. URANOS beamline is equipped with two different monochromators. Stepper motors separate them to swap and incorporate them into the optical

path.
I. Plane grating monochromator (PGM): it allows to select the photon energy range between approximately 16 to 100 eV.
II. Normal incidence monochromator (NIM): this type of monochromator operates at low photon energy. The energy range is from 8 to 20 eV.
**Preparation chamber**: in this chamber, many treatments on the sample

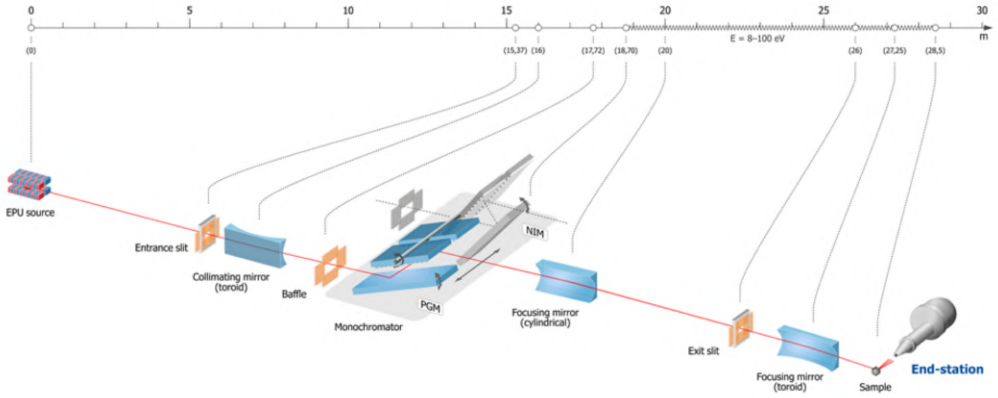


Figure 3.5: The scheme of the URANOS beamline at SOLARIS synchrotron radiation centre, Krakow (the figure is taken from the official website of SOLARIS).

can be performed such as preheating, deposition of other elements, evaporation, etc.
**Load lock**: A load lock vacuum chamber is used to transfer samples from ambient conditions to the main vacuum chamber and vice versa.
**Analysis chamber**: Major ARPES tests are performed in the analysis chamber which is equipped with 5 axis cryogenic manipulator to change the position of the sample and to choose the specific site on the sample. The chamber contains ultra-high vacuum (UHV) ($\sim$ order of $10^{-11}$ mbar) and has the facility to lower the temperature down to 12 K with liquid helium and to 78 K with liquid nitrogen. The hemispherical photoelectron analyzer (SCIENTA OMICRON DA 30-L) (shown in Figure 3.6) allows mapping of the Fermi surface not only in the direction parallel to the analyzer slit but also perpendicular to it. It has energy and angular resolution of 1.8 meV and 0.1° respectively.
**Sample respirator**: this sample chamber can accommodate 12 samples. It is connected to the main analysis chamber. *In situ*, cleaving is possible in this chamber.

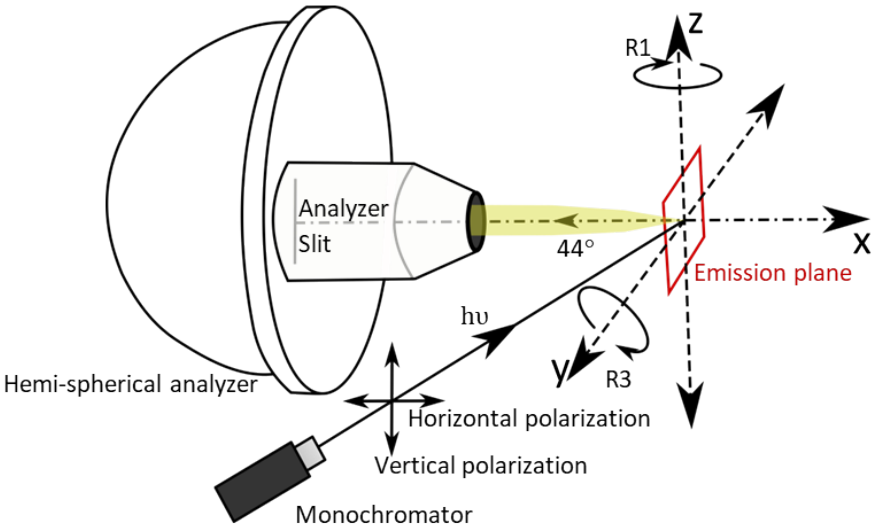


Figure 3.6: A schematic of the ARPES end station of the URANOS beam line.

### 3.2.2 Evaporation of Pb: resistive heating

A Joule heating evaporator is used in order to evaporate the ultrathin layers of Pb. This system is mainly installed in a preparation chamber interlocked with a spectrometer chamber. Pb used as a source was carefully placed inside the assembly of the tungsten coil to obtain the melting point of Pb as depicted in Figure 3.7. It is an example of resistive heating and it has a power supply equipped with PID controllers to control the amount of current in order to control the evaporation rate. In order to protect the sample from damage, it has a facility of ramp function to control the sample temperature. During the deposition rate and thickness were measured by quartz balance. A shutter is equipped with an evaporator which can be opened and closed whenever one needs to start and stop the process of deposition.

### 3.2.3 Evaporation of Nb: electron beam evaporation

Electron beam evaporator EBV 40A1 from PREVAC is used to deposit ultra-thin layers of Nb during the experiment (see Figure 3.8). Especially this evaporator is used to grow monolayers by using the molecular beam evaporation (MBE) technique. It has a facility to mount a source in the form of wire hence we used a pure Nb wire (Alfa Aesar, $\phi = 0.5$ mm, 99.06

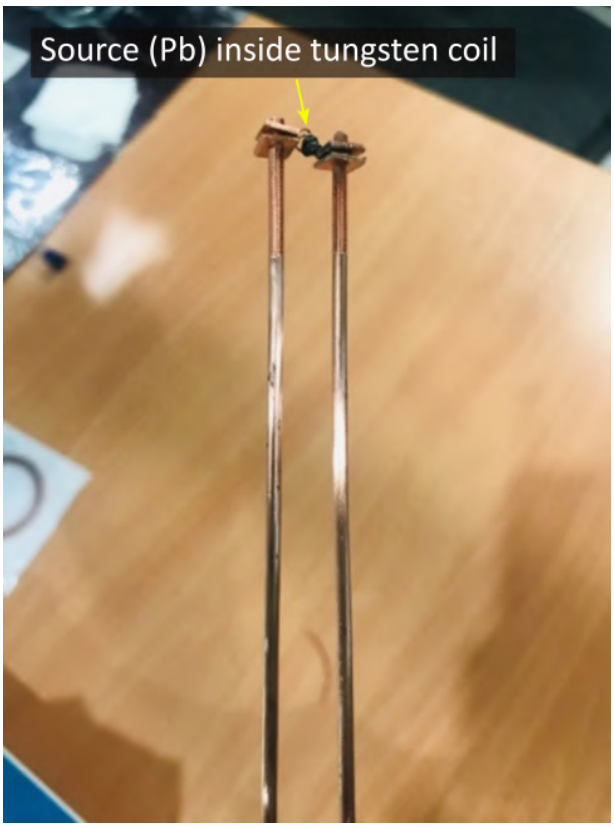


Figure 3.7: Joule heating evaporator system for controlled evaporation of Pb in which a tungsten coil is used to hold Pb.

%). The electron beam produced in the system heats the Nb wire only at the end and melts the metal as shown in the inset (see Figure 3.8(b)). The measured ion flux is proportional to evaporated atoms and is observed by an integrated flux monitor. In order to control the flux of evaporated atoms at a given energy, we set the electron emission current. The thickness was monitored by using quartz balance. At the end of the process, we deposited (*in situ*) 0.8 ML on P-terminated NbP and 1.3 ML on Nb-terminated NbP in ultra-high vacuum (UHV) condition.

### 3.2.4 Sample preparation for ARPES measurements

ARPES technique basically characterizes the surface of the material. The sample should be conductive in order to drain the total induced current, if the sample is not conductive enough then it faces some charging effects which can have a detrimental impact on the measurements. In the ARPES measurements, $TaAs_2$ and NbP single crystals were studied. They are

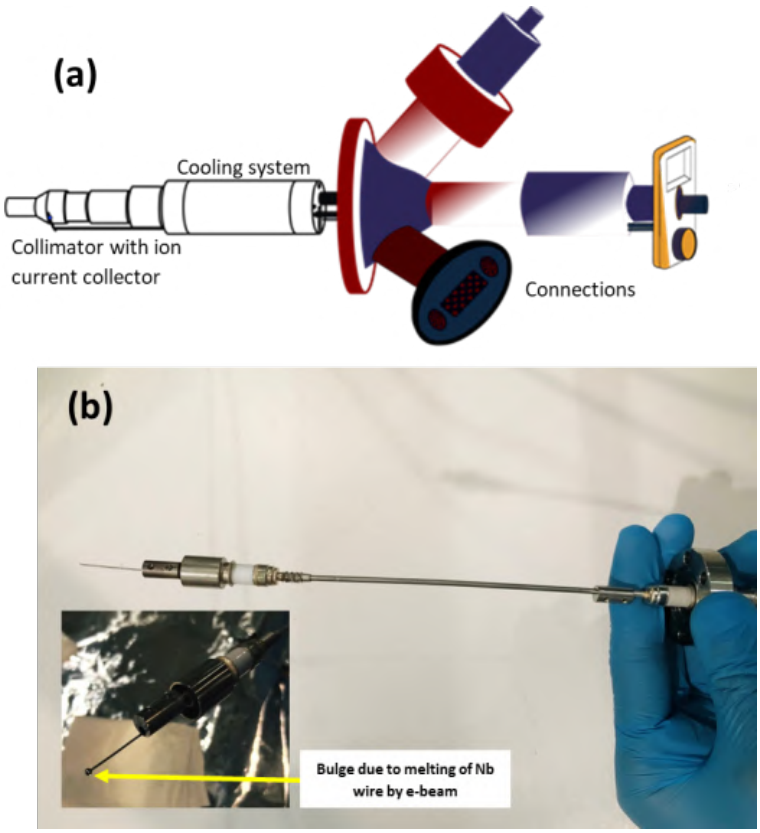


Figure 3.8: (a) complete schematic of the instrument and (b) a part inside e-beam evaporator with Nb wire attached at the top, (inset) the bulge at one end of the wire due to a melt formation by e-beam.

topological materials with semi-metallic nature. As mentioned in an earlier chapter, these crystals were produced by the chemical vapour transport method and then preserved in the lab hence the possibility of surface contamination is high with adsorbent on the surface which is not suitable for ARPES measurements. Hence, before loading the samples in the load lock chamber of the ARPES setup, the samples were prepared with proper techniques explained as follows:
First, the single crystals, metallic stick, copper wire and metallic rectangular stage were cleaned with acetone and ultra-sonicated for 15 minutes and then dried with inert gas. Single crystals were mounted on the rectangular stage and glued with silver epoxy. Metallic sticks were then glued on the top of the crystals and fixed with copper wire as shown in Figure 3.9 so that the stick will not fall into the chamber after cleaving the sample.
After the sample preparation, the samples were transferred to a load lock chamber and created a vacuum in order to transfer the sample into the preparation chamber. The sample was then heated at 200 °C (see Figure

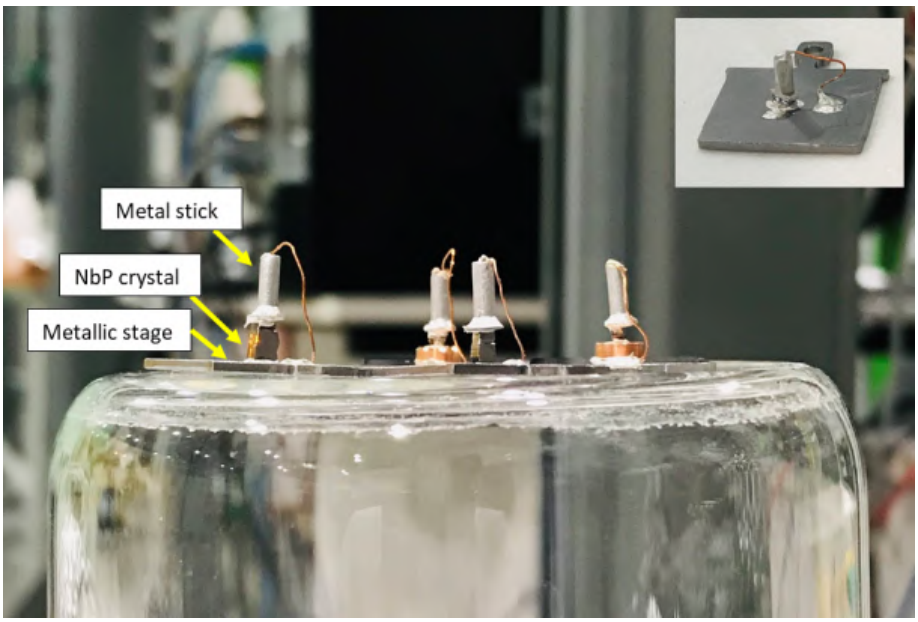


Figure 3.9: Sample preparation of NbP single crystals with rectangular stage and metallic stick supported with copper wire with a side view of the prepared samples, (inset) the sample from the top.

3.10(a) as a preheating treatment in order to remove the contamination. While maintaining the ultra-high vacuum conditions ($\sim$ 5.7e-11 mbar) and the sample was ready to cleave. The sample was cleaved in a respiratory chamber to obtain (0 0 1) surface as shown in Figure 3.10(b)
After cleaving the sample an annealing process has been done on the sample by heating it to 200 °C. Then the sample was moved to the main ARPES analysis chamber where the temperature was lowered to 78 K by using liquid nitrogen. The beam was focused on the clean surface and ARPES data for NbP was acquired. In the case of Pb and Nb deposition, we moved the same sample from the analysis chamber to the preparation chamber and deposited ultrathin layers which were measured by quartz balance and annealed at 150 °C and again moved to the ARPES section. The signatures of Pb and Nb were confirmed by using core-level spectra.

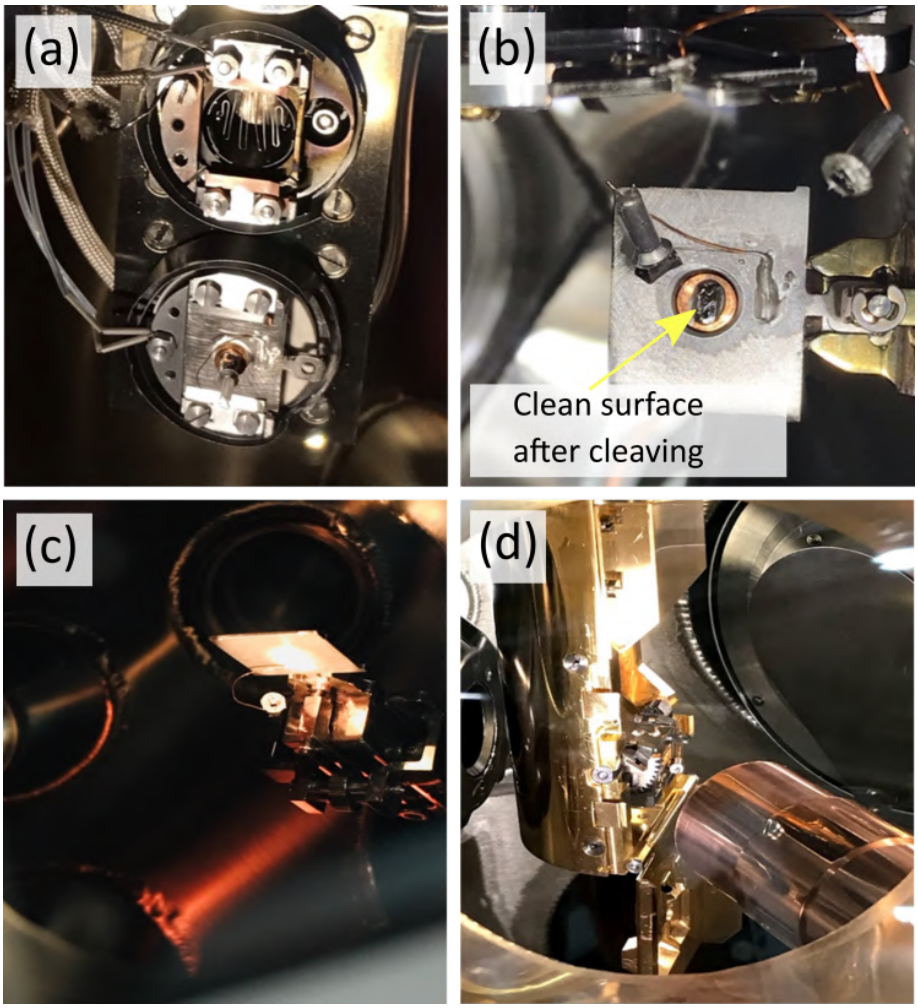


Figure 3.10: Sample preparation process in which (a) preheat treatment before cleaving, (b) *in situ* cleaved sample with cleaned and flat (0 0 1) surface for ARPES measurements, (c) deposition of Pb on cleaved (0 0 1) surface and (d) a sample in the ARPES analysis chamber to acquire data.

# 4

# Tantalum di-arsenide: $TaAs_2$

*God made the bulk; the surface was invented by the devil*

*Wolfgang Pauli*

**The first part of this chapter discusses the experimental results on electron transport of $TaAs_2$ based on A. S. Wadge, G. Grabecki, C. Autieri, B. J. Kowalski, P. Iwanowski, G. Cuono, M. F. Islam, C. M. Canali, K. Dybko, A. Hruban, A. Łusakowski, T. Wojciechowski, R. Diduszko, A. Lynnyk, N. Olszowska, M. Rosmus, J. Kołodziej, and A. Wisniewski, J. Phys.: Condens. Matter 34, 125601 (2022).**

## 4.1 Low-temperatures electron transport

$TaAs_2$ is a topological material that has attracted significant attention in recent years due to its potential for hosting different topological states of matter. This material is a transition metal di-pnictide which has been studied theoretically and experimentally [14, 15, 17, 19, 20, 90–92]. $TaAs_2$

is centrosymmetric i.e. the inversion symmetry is preserved along with time-reversal symmetry. Theoretical calculations predict that $TaAs_2$ acts as a weak topological insulator in the absence of an applied magnetic field, which means it has a bulk band gap and topologically protected surface states that are characterized by a non-trivial topological invariant and are robust against certain types of perturbations [13]. However, experimental studies have shown that when a magnetic field is applied, $TaAs_2$ can host type II Weyl points [18]. The Weyl cones in type II WSM are strongly tilted forming the Weyl points at electron-hole pocket contacts [61]. Such time reversal symmetry broken systems are still under investigation [62, 93–95]. This compound is interesting to study because it provides a platform to investigate the interplay between different topological states of matter and how they respond to external perturbations such as applied magnetic field. The temperature dependence of electrical resistivity in $TaAs_2$ can be studied

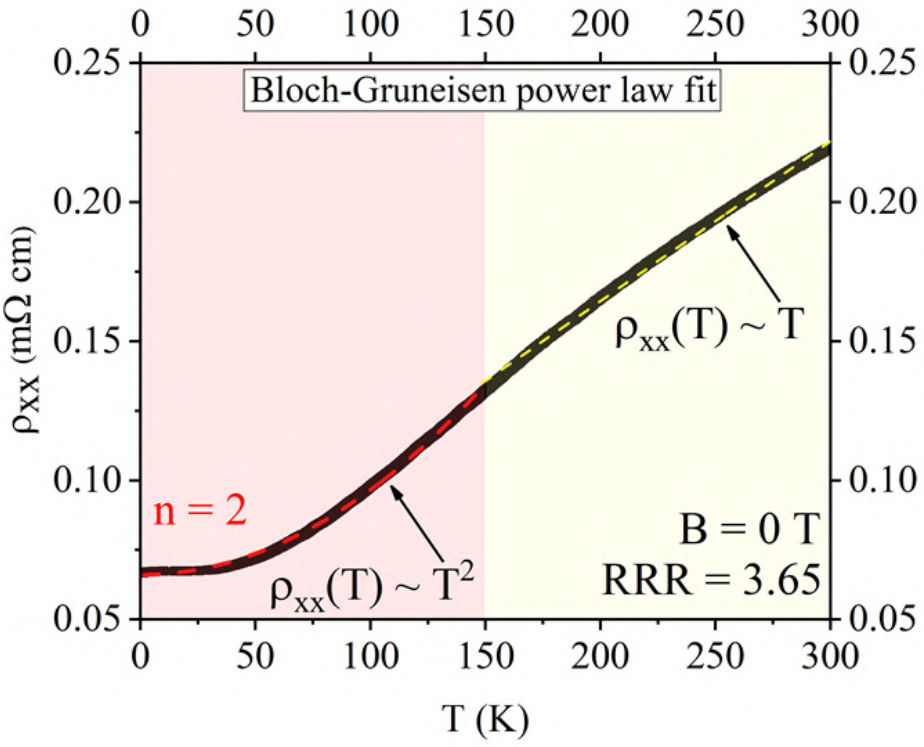


Figure 4.1: Resistivity as a function of temperature at zero magnetic field with power law fit at low temperatures n = 2 (electron-electron interaction) and linear dependence at higher temperature due to electron-phonon interaction.

by examining the resistivity as a function of temperature in the absence of a magnetic field as shown in Figure 4.1. It shows metallic behavior. One way to model this behavior is through the use of the Bloch-Grüneisen

power law fit. This model suggests that the resistivity is influenced by the interactions between electrons and phonons, which are lattice vibrations within the material. To use the power law fit, the measured resistivity data are compared to an equation 4.1:

$$\rho_{xx} = \rho_0 + AT^n \tag{4.1}$$

Where $\rho_0$ is a residual resistivity value, A is a fitting parameter, $T$ is temperature, and $n$ is the power law exponent. The value of $n$ can provide insight into the dominant scattering mechanism within the material, such as electron-phonon or electron-impurity interactions. It's worth noting that the Bloch-Gruneisen power law fit is an approximation and its validity depends on the temperature range and the nature of the material itself. For temperatures smaller than 150 K, the power law gives $n = 2$ with $\rho_0 = 6.6 \times 10^{-5}$ Ω cm and A=$3\times10^{-6}$ Ω cm/$K^2$. This is electron-electron scattering which is also known as Coulomb scattering and it occurs when electrons interact with each other through the Coulomb potential. This interaction results in an enhancement of resistivity with temperature that is also proportional to the square of the temperature. At higher temperatures, it shows linear behavior with slight bending as shown in Figure 4.1 which may occur due to temperature-dependent bands in the electronic structure [96, 97].

The residual resistivity ratio (RRR) is calculated by taking the ratio of the resistivity at absolute zero temperature (or at the lowest temperature of the sample) to the resistivity at a high temperature, such as room temperature. A higher RRR implies a higher quality sample with fewer impurities and defects, resulting in a lower resistivity.

$$RRR = \frac{\rho_{300K}}{\rho_{1.6K}} = 3.65$$

Although the RRR value of our $TaAs_2$ crystals is lower than reported in other articles, the electron transport properties of the studied samples show similarities to those reported in previous papers, with the perpendicular magnetoresistance (MR) reaching approximately $1.4 \times 10^4$ % at 9 T and 1.6 K. However, it is worth noting that this value is smaller by one order of magnitude compared to the findings published earlier [15, 17, 20, 71, 92].

Low-temperature electron transport provides insight into the electronic properties of the material and the interplay between the magnetic field and the topological states of matter. In the magnetic field (B) applied perpendicularly to the ($\bar{2}$ 0 1) plane, the resistivity increases at lower temperatures, indicating metal to insulator transition. When a constant magnetic field is applied, flat resistivity regions at low temperatures appear. Instead of the resistivity continuing to increase as the temperature decreases, there is a temperature range where the resistivity remains relatively constant.

Specifically, at around 28 K, the resistivity reaches a point where it remains relatively constant, forming a plateau (see Figure 4.2). The value of the temperature, 28 K is close to the value reported by Y.-Y. Wang, et al. [98]. This behavior is thought to be a result of the balance between the density of states and the mobility of the carriers in the material. The interplay

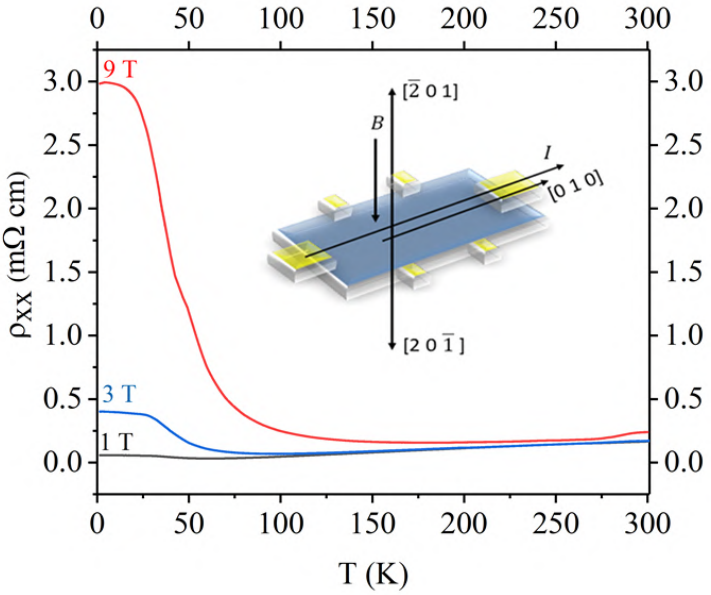


Figure 4.2: Temperature dependence of longitudinal resistivity ($\rho_{xx}$) at 1, 3 and 9 T. (inset) shows the sample configuration in which magnetic field (B) is perpendicular to ($\bar{2}$ 0 1) plane.

between the material's topological properties, such as the Berry curvature, and the magnetic field is believed to play a role in this balance. However, at high magnetic fields, this plateau becomes distorted, due to the emergence of Shubnikov-de Haas (SdH) oscillations. A detailed description of SdH oscillation is given in a later section.

Kohler's law states that at a constant temperature, MR should merge when plotted as a function of the ratio of the magnetic field to resistivity at zero magnetic field. This means that the magnetic field should not influence the MR as long as the ratio is the same. Kohler's plot for different temperatures, shown in Figure 4.3, indicates that our sample of $TaAs_2$ holds Kohler's law only for temperatures below 20 K. As stated earlier, there exists a slight bending in the graph and this bending may be the reason to violate Kohler's rule at higher temperatures due to thermally induced change in the bands as explained by J. Xu, et al. [99].

The sample configuration in which magnetic field (B) $\parallel$ [$\bar{2}$ 0 1] and the direction of current (I) is along the $b$ axis, shows a large positive non-saturating MR. As shown in Figure 4.4 (a), $TaAs_2$ exhibits 14 000 % MR at

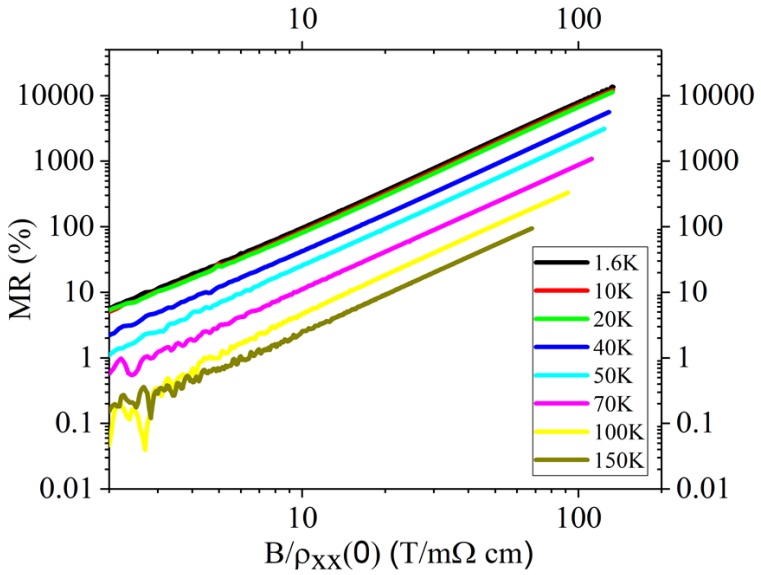


Figure 4.3: A plot shows the violation of Kohler's plot over the temperature range from 20 K.

1.6 K. The MR does not show much deviation up to 20 K and significantly reduces to 48 % at 300 K (see Figure 4.4 (b)). The behavior of the MR is parabolic and non-saturating up to 9 T.
A. Narayanan, et al. showed that the MR value in $Cd_3As_2$ is approx. 2000 % at 4 K [100]. Y. Luo et al. obtained $4 \times 10^6$ % MR for $TaAs_2$ at 0.3 K [15]. Also, D. Wu et al. reported $1.2 \times 10^6$ % MR at 2 K [92]. For $TaAs_2$, the balance between the number of electrons and holes results in a state of charge compensation which also means an approximately equal number of electron and hole carriers. This charge compensation process is responsible for large non-saturating magnetoresistance in $TaAs_2$.
This balance is maintained by the presence of impurities or defects in the material, which acts as scattering centers for the carriers. When a magnetic field is applied to the material, it causes a shift in this balance by affecting the charge neutrality point, leading to a suppression of backscattering and a decrease in resistivity, known as non-saturating magnetoresistance. Also at lower temperatures and strong magnetic fields, we observed strong oscillatory behavior in magnetoresistance above 4 T and it is known as Shubnikov-de Haas (SdH) oscillations which are studied in the later section.
A transverse magnetoresistance (Hall resistance) appeared in $TaAs_2$ in response to the applied magnetic field perpendicular to $(\bar{2}\ 0\ 1)$ and current parallel to (0 1 0) which is proportional to the distribution of charge carriers in the sample. We anti-symmetrized the Hall resistivity (to avoid the extra effects from asymmetric leads) and plotted it as a function of the magnetic field over the temperature range from 1.6 to 300 K (see Figure 4.4 (c,

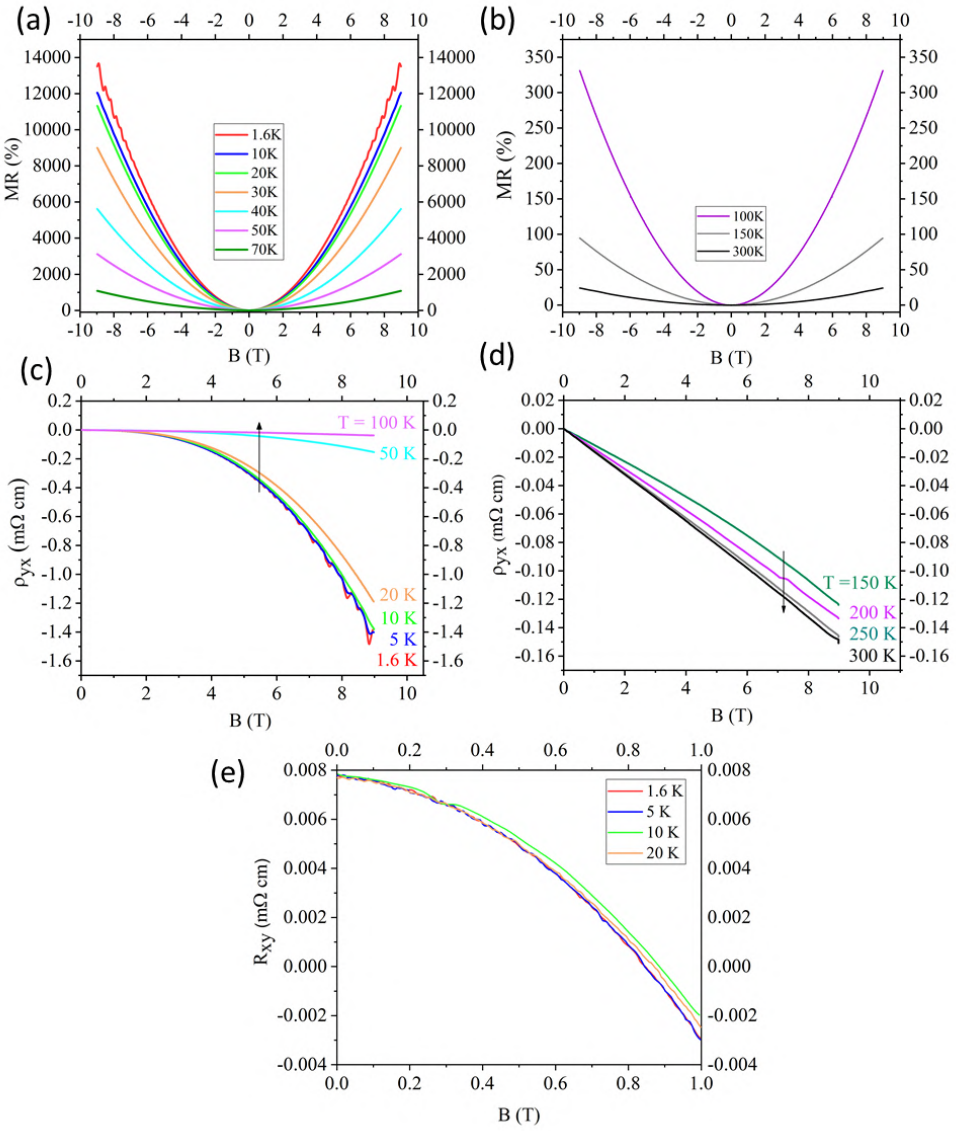


Figure 4.4: Longitudinal magnetoresistance of $TaAs_2$ as a function of magnetic field (a) over the temperature range 1.6 to 70 K, (b) from 100 to 300 K. Also it displays the Hall effect on $TaAs_2$ when magnetic field, B is perpendicular to $(\bar{2}\ 0\ 1)$ orientation and current is parallel to $b$ axis (c) over the temperature range 1.6 to 100 K showing strongly non-linear behavior, (d) depicts Hall effect from 150 to 300 K changing the sign from positive to negative shown by the arrow and (e) shows the magnified Hall data from 1.6 to 20 K.

d)). The non-linear behavior of the Hall signal indicates the presence of many carriers in the system. The slope of Hall resistivity is negative at

lower temperatures and field below 2 T (see Figure 4.4(e)) and rises with increasing field which indicates the existence of electron and hole pockets and their contribution to overall conductance. Above 100 K, Hall resistivity is almost linear with changing direction indicated by the arrow in Figure 4.4 (c, d), which indicates the electron dominant behavior. The two-band model

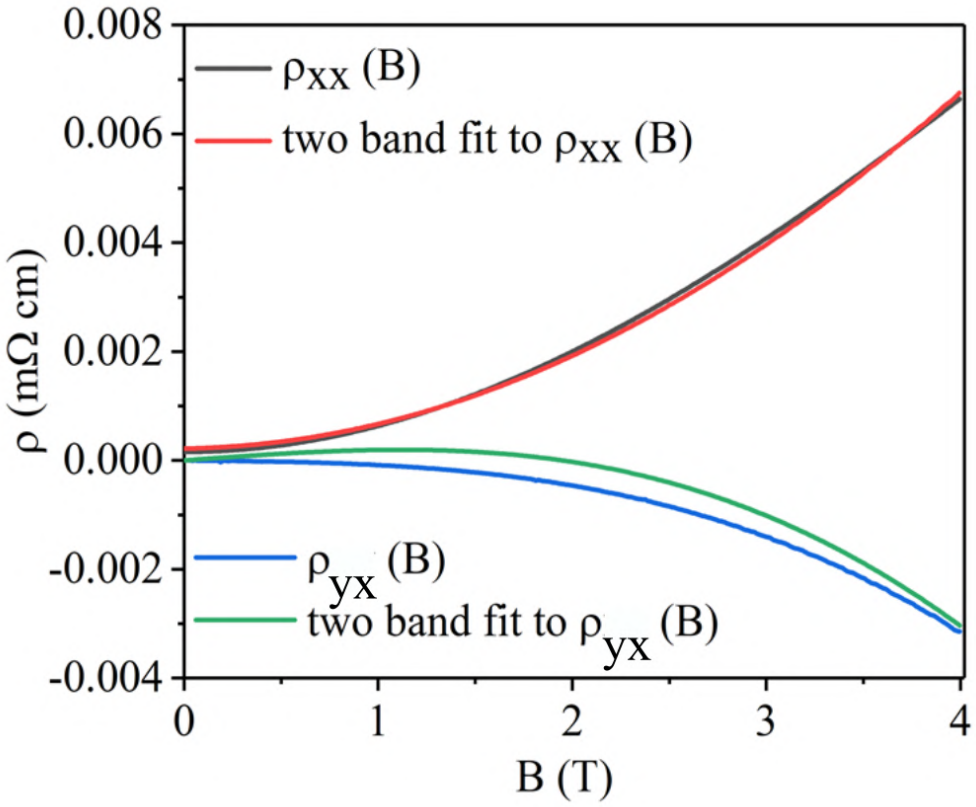


Figure 4.5: An experimental data of $\rho_{xx}$ and $\rho_{yx}$ fitted with two band model in order to calculate carrier concentration.

is an approach in a multicarrier system to calculate the average electron and hole mobilities and concentrations. Here, we used the two-band model to calculate carrier concentrations which are given as:

$$\rho_{xx} = \frac{1}{e}\frac{((n_h\mu_h + n_e\mu_e) + (n_e\mu_e\mu_h^2 + n_h\mu_h\mu_e^2))B^2}{(n_h\mu_h + n_e\mu_e)^2 + \mu_h^2\mu_e^2B^2(n_h - n_e)^2} \tag{4.2}$$

$$\rho_{yx} = \frac{B}{e}\frac{((n_h\mu_h^2 - n_e\mu_e^2) + \mu_h^2\mu_e^2B^2(n_h - n_e)}{(n_h\mu_h + n_e\mu_e)^2 + \mu_h^2\mu_e^2B^2(n_h - n_e)^2} \tag{4.3}$$

Where, $n_h$= hole concentration, $\mu_h$= hole mobility, $n_e$= electron concentration, $\mu_e$= electron mobility, B = applied magnetic field and e = 1.6 $\times 10^{-19}$ C. We have fitted the two-band model (according to equation 4.2 and 4.3)

simultaneously to experimentally obtained $\rho_{xx}$ and $\rho_{yx}$ data at 1.6 K. The fitting has been done up to 4 T (see Figure 4.5) and gives $n_h = 3.1\times10^{19}$ $cm^{-3}$ and $n_h = 3.5\times10^{19}$ $cm^{-3}$ which show the nearly equal number of carriers in the system. Nearly the same number of charge carriers also is one of the reasons for non-saturated magnetoresistance. The mobilities corresponding to carrier concentrations are $\mu_h = 1.4\times10^4$ cm$^2$/Vs and $\mu_e = 1.3\times10^4$ cm$^2$/Vs, respectively.

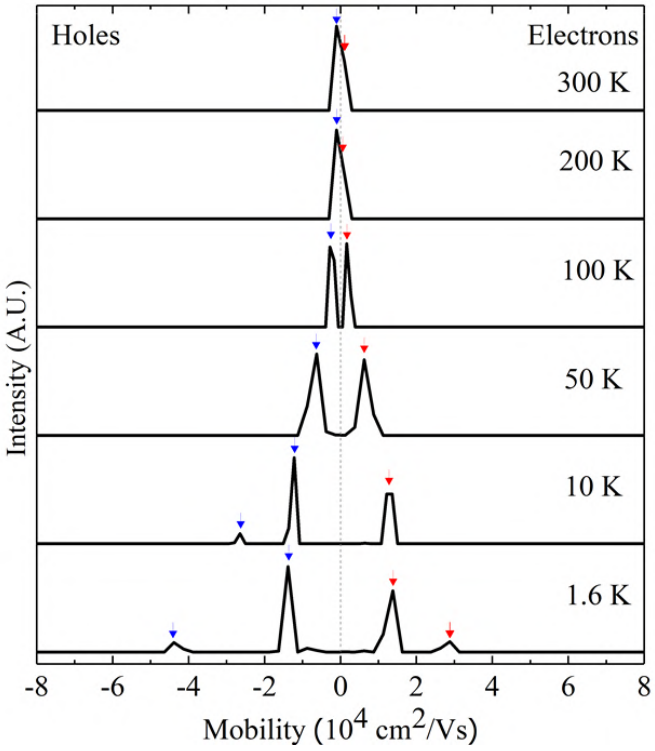


Figure 4.6: Multicarrier mobility spectra shown from 1.6 to 300 K. Holes and electrons with different mobilities are marked by blue and red arrows respectively.

As we discussed earlier, if the system has more than two types of carriers then it is difficult to show the mobility associated with each type of carrier. We already know that $TaAs_2$ contains multiple Fermi pockets contributing to conductivity hence multicarrier mobility spectrum analysis (MSA) is a possible solution to resolve this problem. MSA is an efficient tool to show the different mobilities on a single plot by using different conductive channels contributing to carrier transport measurements [101–103].
Figure 4.6 shows four separate peaks at 1.6 K out of which two represent holes and are marked by blue arrows whereas the other two peaks of electrons are marked by red arrows. The code to extract MSA was written

in FORTRAN language with linear algebra package also called LAPACK libraries. These libraries help to solve linear equations, eigenvalue problems, singular value problems and least square solutions. It also handles the dense and banded matrices. The input file contained data with three columns: B, $\sigma_{xx}$ (B) and $\sigma_{xx}$(B). The output was taken with 800 points. The longitudinal and transverse conductivity components were calculated as shown in equation 4.4 and 4.5. The FORTRAN code for MSA converts these conductivity inputs in terms of the integral of the conductivity density function in the following equations:

$$\sigma_{xx}(B) = \int_{-\infty}^{\infty} \frac{S(\mu)}{1+\mu^2 B^2} d\mu \tag{4.4}$$

$$\sigma_{xy}(B) = \int_{-\infty}^{\infty} \frac{S(\mu)\mu B}{1+\mu^2 B^2} d\mu \tag{4.5}$$

These expressions are reframed for compounds with arbitrarily shaped Fermi surfaces by solving Boltzmann's equation in the presence of the magnetic field. It gives a wider understanding of the transport mechanism present in $TaAs_2$. As temperature increases, the peaks are merging into one as depicted in Figure 4.6. At higher temperatures, mobility reduces due to the phonon-assisted scattering process. The accuracy of mobility spectrum analysis can be compromised by the presence of Shubnikov-de Haas oscillations in the input data. In order to get reliable results from mobility spectrum analysis, we eliminated the SdH oscillations from the data before analysis. This was done by subtracting the oscillatory component above 4 T. This process allowed us for a clearer understanding of the mobility spectrum and a more accurate determination of mobilities in the sample.

### Shubnikov-de Haas oscillations

SdH oscillations occur in the magnetoresistance of highly degenerated samples in a strong magnetic field and low temperatures. In the case of $TaAs_2$, the significant oscillations with frequency beating were separated by subtracting a background signal by fitting a polynomial function to magnetoresistance. Figure 4.7 (a) shows that the oscillations survived till 20 K. The oscillations have vanished above 20 K. There is a good homogeneity in the sample in contrast to the low RRR value allowing the observation of pronounced SdH oscillations up to 20 K. Thermal smearing of the Fermi surface at higher temperatures (20 K and higher) is one of the important reasons behind vanishing SdH oscillations. As the temperature rises, the electrons can occupy a larger range of energy levels, which broadens the Fermi surface. As it broadens, the quantization of the electron orbits

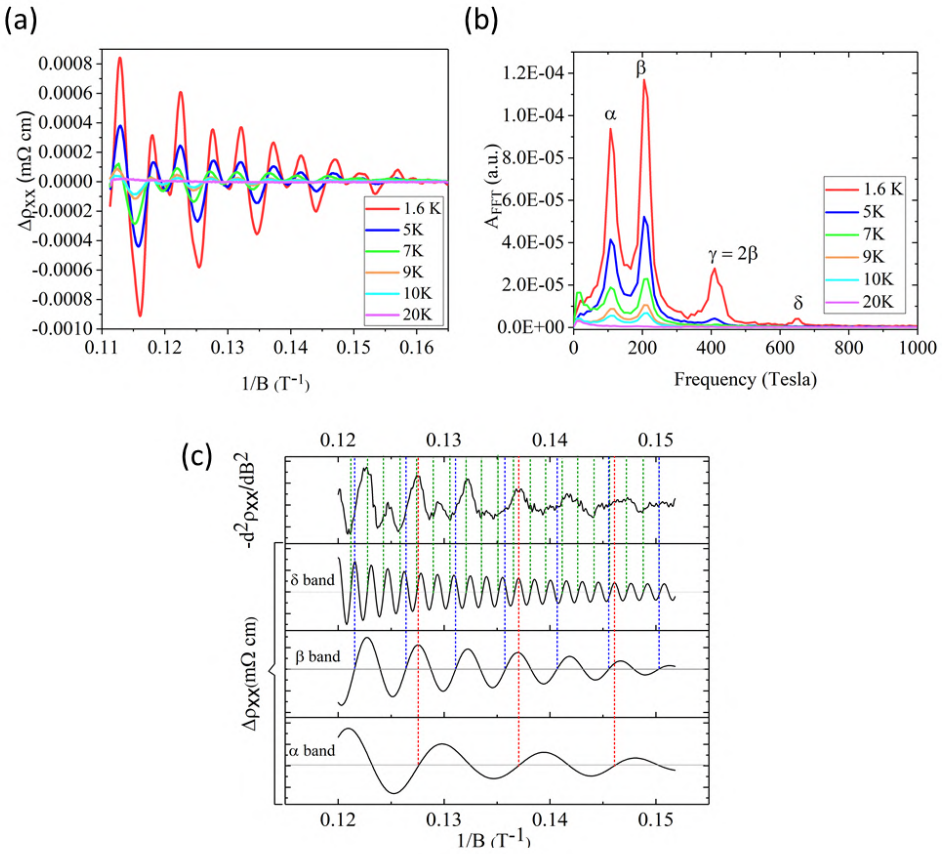


Figure 4.7: Quantum oscillations in longitudinal magnetoresistance (a) Shubnikov-de Haas oscillations extracted by subtracting background signal and plotted as a function of 1/B from 1.6 to 20 K, (b) fast Fourier transform (FFT) of SdH oscillations showing 4 significant peaks, (c) second derivative of the resistivity with respect to magnetic field B and inverse Fourier transform of separate frequencies.

becomes less prominent, and the oscillations in the longitudinal resistance become less visible. The increased thermal motion of the electrons can also lead to a reduction in the coherence of the electron orbits, further reducing the visibility of the SdH oscillations. Here, the FFT (Fast Fourier Transform) was used in order to analyze the signals and to determine the frequency components involved in the signal. With FFT, it is possible to determine the frequency spectrum of the SdH oscillations. It gives important information about the Fermi surface cross-section of the orientation perpendicular to the magnetic field. This was done by taking the discrete Fourier transform of the time-domain data, and then converting it to the frequency domain. As depicted in Figure 4.7(b), FFT indicates the presence of multiple Fermi

surface cross-sections at 109, 207 and 646 T designated as $\alpha, \beta$ and $\delta$ respectively. Pocket $\gamma$ is the second harmonic of pocket $\beta$. FFT signals are plotted at temperatures from 1.6 to 20 K.
The presence of multiple Fermi pockets makes the analysis of SdH oscillations difficult. Hence, the band pass filtering process followed by inverse Fourier transform helps to separate out the pure damping oscillations corresponding to respective frequencies as shown in Figure 4.7 (c). It is shown that it consists of the $\alpha, \beta$ and $\delta$ indicating periodic dependence by red, blue and green colors, respectively. Earlier, we have shown that the fast Fourier

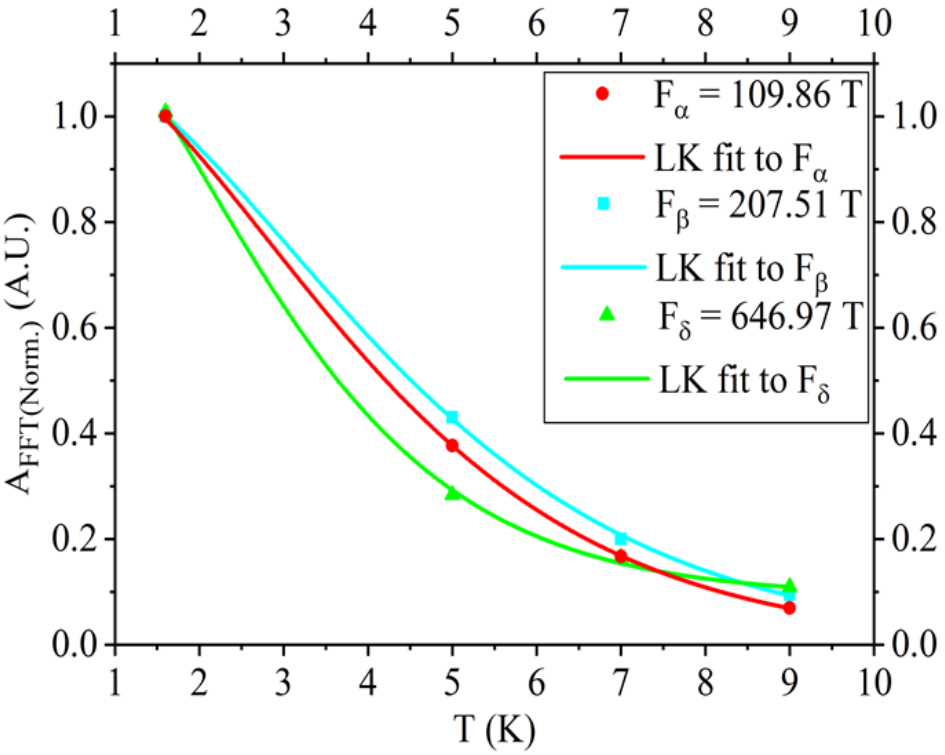


Figure 4.8: Temperature dependence of normalized FFT amplitude shows the Lifshitz-Kosevich (LK) fit in order to extract the effective masses.

transform (FFT) of SdH oscillations transforms the signal into the frequency domain, revealing three substantial frequency peaks. We have plotted the data from 1.6 K to 20 K as frequency vs FFT amplitude (see Figure 4.8 (b)). The Lifshitz-Kosevich (LK) formula (see equation 4.6) is used to describe the behavior of the SdH oscillations as a function of the magnetic field and the effective mass of the electrons.

$$\Delta A_{FFTNORM}(T) = \frac{\left(\frac{2\pi^2 k_B m^* T}{e\hbar B}\right)}{\sin\left(\frac{2\pi^2 k_B m^* T}{e\hbar B}\right)} \tag{4.6}$$

By fitting the FFT amplitude of the oscillations to the LK formula as shown in Figure 4.8, we have extracted the cyclotron effective masses associated with the Fermi pockets 109, 207 and 646 T. The corresponding effective masses are 0.30, 0.28 and 0.40 $m_e$ respectively. Other parameters such as the area of cross-section of the Fermi surface, Fermi wave-vector, Fermi velocity and Fermi energy can also be extracted from effective masses but they are not very accurate because these parameters are calculated by assuming the circular Fermi surface which is not the true in case of $TaAs_2$. It is highly anisotropic as well as complicated shapes along with elliptical Fermi pockets. FFT frequency is dependent on the magnetic field as well as

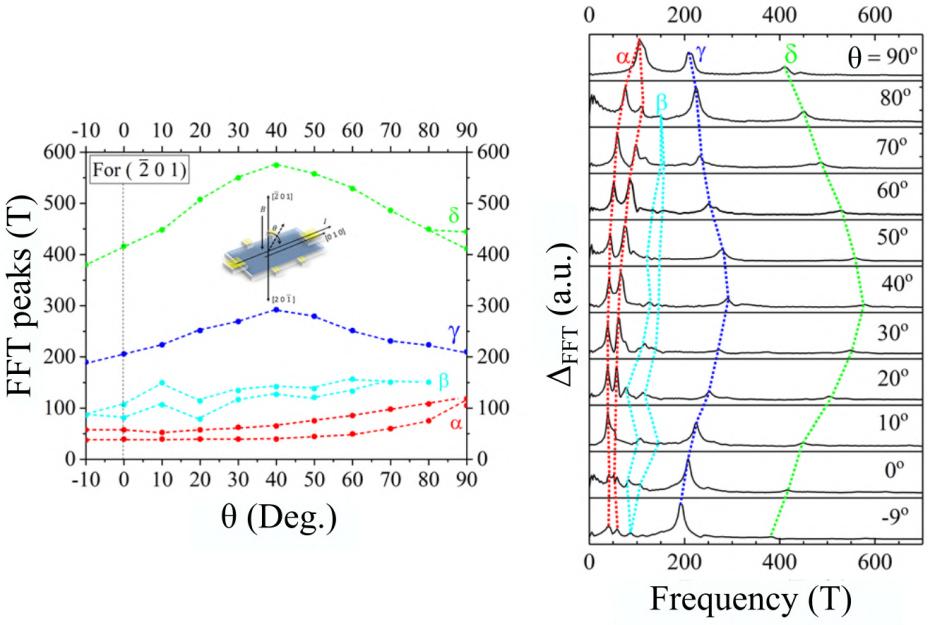


Figure 4.9: Angular dependence of the frequency of FFT of SdH oscillations showing the shifted positions of FFT peaks at various angles with reference to the magnetic field (inset) shows the sample configuration in which ($\bar{2}$ 0 1) orientation of the sample is rotated through an angle $\theta$ with respect to the magnetic field.

on the specific location at the Fermi surface that is being probed (see Figure 4.9). It is because the FFT frequency is proportional to the cross-sectional area of the Fermi surface perpendicular to the magnetic field. Different points on the Fermi surface have varying cross-sectional areas perpendicular to the magnetic field, leading to differences in the FFT frequency. One can determine the shape of the Fermi surface and the specific location of the probing point on the Fermi surface by analyzing the angular dependence of the FFT frequency. S. Sun et al. have shown that the electron transport properties in $TaAs_2$ strongly depend on the orientation of the sample [14].

Hence, we have undertaken the angle dependence investigation by rotating the sample with respect to the magnetic field (inset in Figure 4.9). We observed that the Fermi surface trajectories are part of an elliptical shape up to 90° (see Figure 4.9). The rotating probe we used can only rotate up to 90° due to technical limitations.

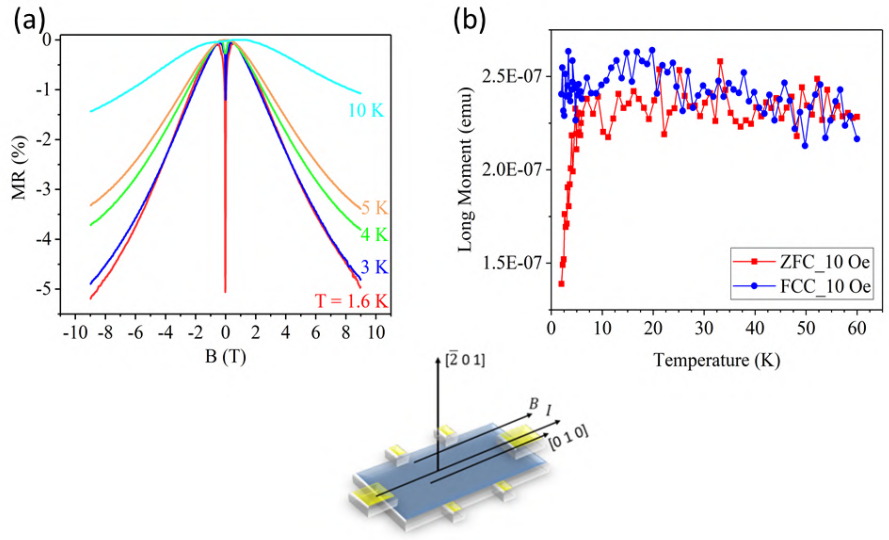


Figure 4.10: (a) A plot of negative magnetoresistance from temperature 1.6 to 10 K with and (outset) the sample configuration showing the parallel direction of magnetic field and electric field, (b) magnetization measurements in which zero field and field cooling show the transition at 4.5 K.

Application of a magnetic field in parallel to the direction of the electric field, as in Figure 4.10 (outset), shows the existence of negative magnetoresistance which may be due to the existence of type II Weyl points in the magnetic field because the magnetic field breaks the time-reversal symmetry [14]. Intriguingly, a sharp dip at zero magnetic fields was observed (see Figure 4.10 (a)). The intensity of the sharp peak was reduced as temperature increased and finally disappeared above 5 K. It may happen due to the superconducting nature of tiny tantalum clusters in the sample which were triggered in the parallel configuration. To support this fact, we performed SQUID measurements (Zero-field cooling and field cooling at 10 Oe) on the same sample used for transport measurements (see Figure 4.10 (c)). It showed a superconducting transition at 4.5 K which is a superconducting transition temperature of tantalum.

## 4.2 Band structure calculations

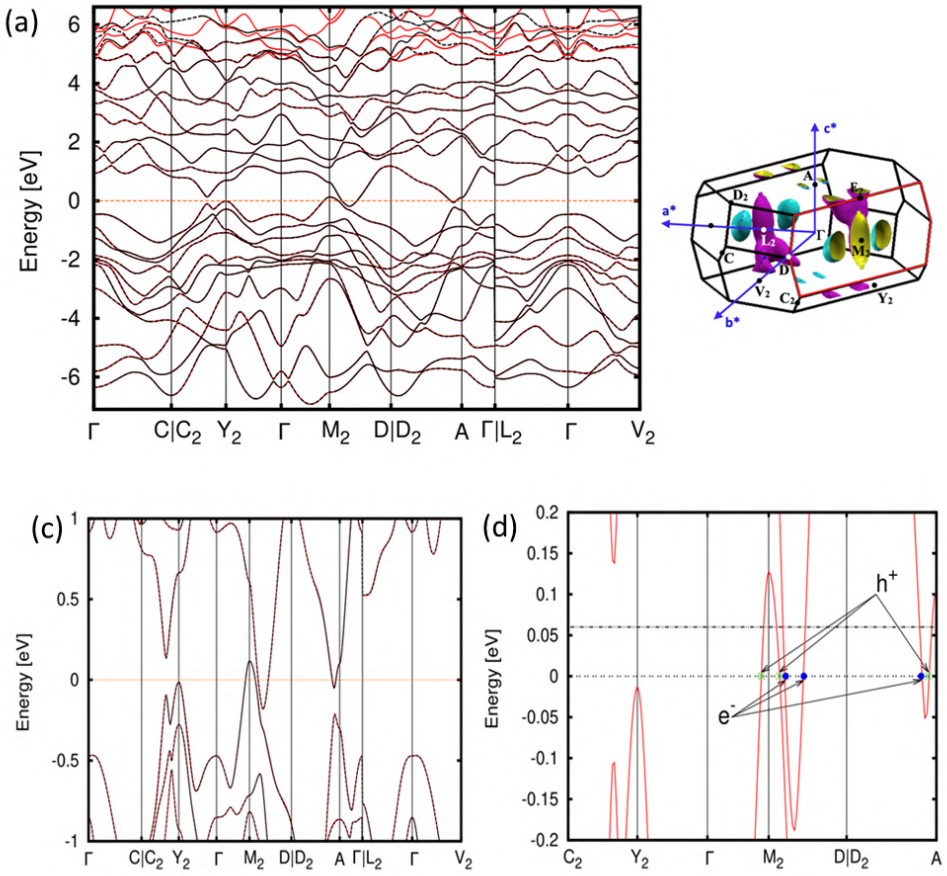


Figure 4.11: (a) the band structure of $TaAs_2$ with spin-orbit coupling, plotted using experimental lattice constants and spanning a range from -7.5 to 6.5 eV. The red line represents the result obtained using density functional theory (DFT), while the black dotted lines indicate the p-d tight-binding obtained with Wannier 90. The zero energy point corresponds to the Fermi level (FL). (b) 3D Fermi surface of $TaAs_2$ with red outline indicating $(\bar{2}\ 0\ 1)$ orientation in $k$ space, (c) a magnified version of the band structure between energies -1 to 1 eV and (d) with a larger magnification of band structure with electron and hole effective masses indicated by blue and green markers, respectively.

At room temperature, the primitive cell of $TaAs_2$ has experimental lattice constants of $a_p = 4.963$ Å, $b_p = 4.963$ Å, and $c_p = 7.752$ Å, with angles $\alpha_p = 62.229°$, $\beta_p = 117.771°$, and $\gamma_p = 140.143°$, in the convention used by the experimentalists. The relations between the lattice vectors of the primitive

and conventional unit cells are given by $\overrightarrow{a_C} = \overrightarrow{a_p} - \overrightarrow{b_p}, \overrightarrow{b_C} = \overrightarrow{a_p} + \overrightarrow{b_p}, \overrightarrow{c_C} = \overrightarrow{c_p}$ which result in lattice constants of $a_C = 9.331$ Å, $b_C = 3.383$ Å, and $c_C = 7.752$ Å for the conventional unit cell, with angles $\alpha_C = 90°$ $\beta_C = 119.71°$, and $\gamma_C = 90°$. Since the ARPES experiments were conducted at 80 K, it is necessary to have smaller lattice constants to match the experimental results.
We determined that Ta is $s^0d^5$ and found that the oxidation states are zero when the stoichiometry of the transition metal is comparable to the pnictide, as in $TaAs_2$. We chose the k-path proposed in reference [104] and calculated the bands with SOC using DFT calculations (see Figure 4.11 (a, c and d)), which were fit with Wannier 90 in a wide energy range around the Fermi level (FL). The three-dimensional Fermi surface of the system and the BZ are shown in Figure 4.11 (b), with the surface related to the ($\bar{2}$ 0 1) orientation highlighted as it is relevant for the ARPES experiments.

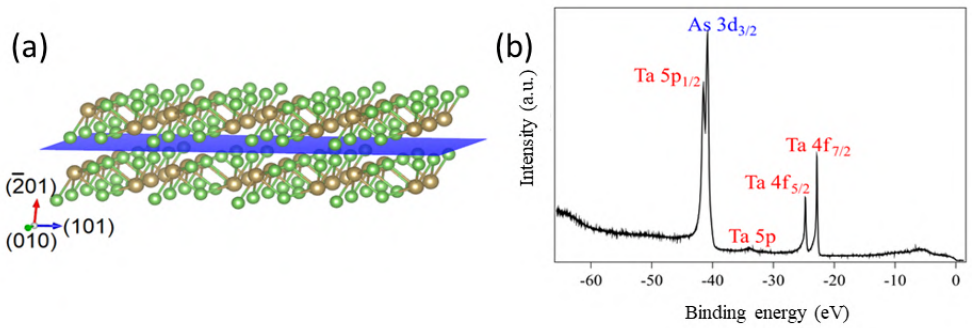


Figure 4.12: (a) A lateral view of the (201) surface, where the ($\bar{2}$ 0 1) plane is represented by the blue plane. The axes utilized are in conformity with the conventional unit cell notation. The As and Ta atoms are illustrated as green and brown balls, respectively. The core level spectra obtained at $h\nu = 100$ eV are shown in (b), where tantalum core level peaks at 4f and 5p are highlighted in red color, and the 3d core level peak of arsenic is illustrated in blue color.

Before taking experimental ARPES spectra, we have cleaved the single crystals of $TaAs_2$ in UHV, in order to obtain a clean surface. In the case of $TaAs_2$ single crystals, it is relatively difficult to cleave the crystals as they have long flat surfaces but in our investigation, we successfully cleaved a specific surface ($\bar{2}$ 0 1) denoted using the conventional unit cell notation. By utilizing DFT, we calculated the cleavage energy (CE) and found that $CE_{(\bar{2}01)} = 1.47$ eV, $CE_{(001)} = 1.62$ eV, and $CE_{(110)} = 3.78$ eV. Our findings indicate that the ($\bar{2}$ 0 1) surface is the easiest to cleave as it has the lowest value of CE. Notably, this surface exclusively comprises As-As bonds, as demonstrated in Figure 4.12 (a). We attribute the low CE to the presence of

As-As bonds, as the (0 0 1) surface with low CE also contains several As-As bonds, which reinforces this phenomenon. We propose that the weaker As-As bond strength in comparison to the Ta-As bond strength results in a lower CE, making this particular surface cleavable. We attribute this physical behaviour to the As p-states, which are distant from the Fermi level and, hence, comparatively weakly bonded compared to the Ta states present at the Fermi level. The core-level spectra acquired at $h\nu = 100$ eV display characteristic tantalum and arsenic peaks, confirming the successful cleavage of the surface (see Figure 4.12 (b)).

## 4.3 ARPES study

Our theoretical investigation focused on the semi-infinite slab with an orientation of $(\overline{2}\ 0\ 1)$, which is relevant for ARPES experiments. To tune the Fermi surface, we performed calculations and generated Figure 4.13 (a and b).

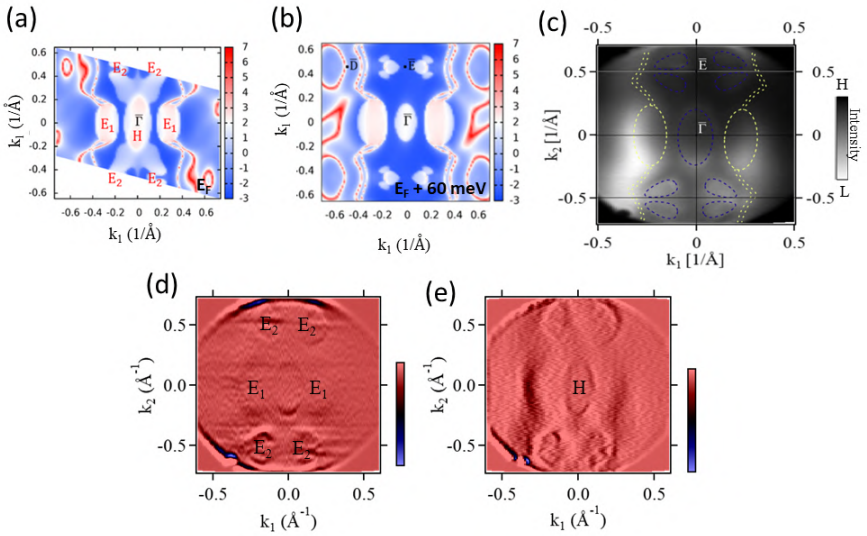


Figure 4.13: (a) The theoretically calculated Fermi surface at the FL, (b) 60 meV above the Fermi level. The spectral function is indicated on a logarithmic scale using a color bar, (c) the experimental constant energy contour captured at a photon energy of 25 eV, which is considered the best case of energy resolution with visual traces and (d, e) the second derivative of the energy distribution curve (EDC) and momentum distribution curve (MDC) curvatures in order to show electron pockets E1 more clearly.

Figure 4.13 (c) shows the Fermi surface without any doping. As the system is not purely insulating, the surface states are a mixture of trivial and topological states, including the bulk bands that are projected onto the surface [105].

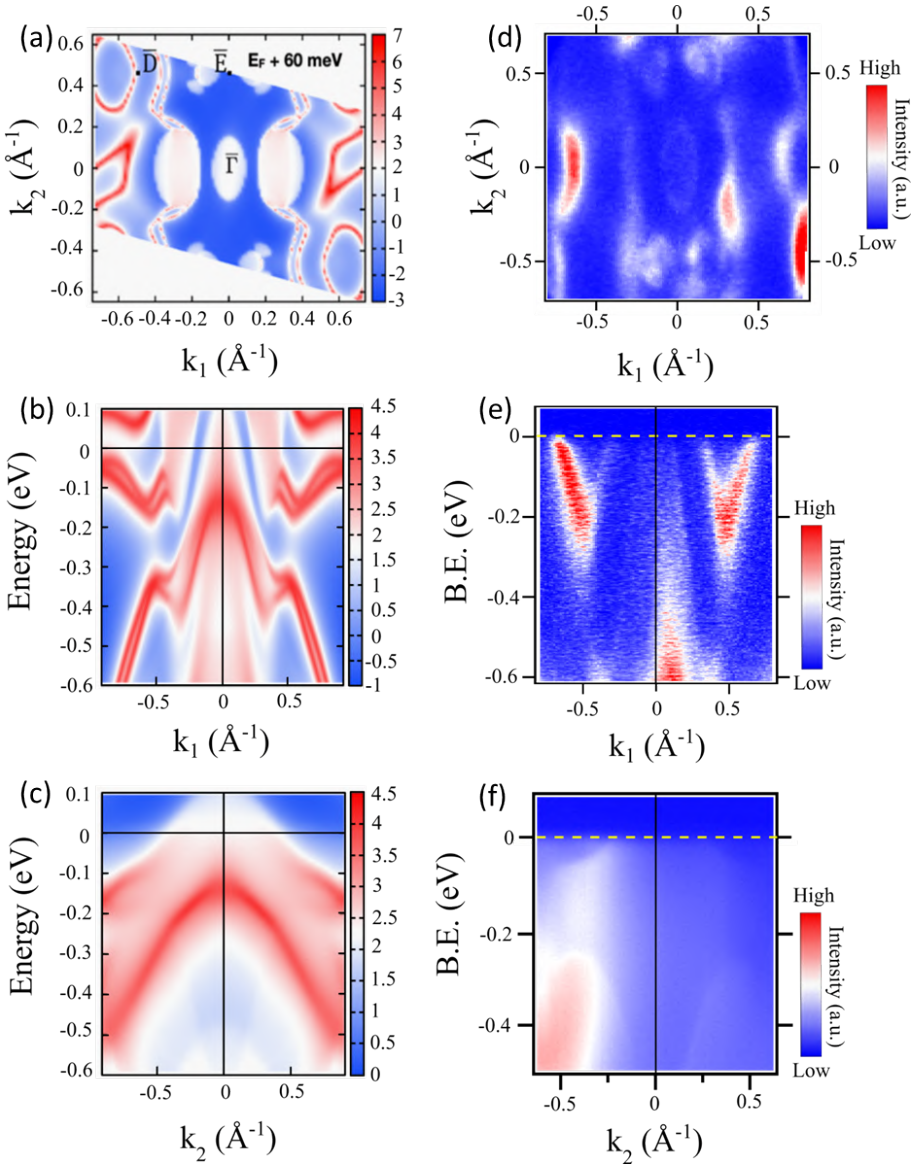


Figure 4.14: Comparisons between theoretical and experimental (a, d) 2D Fermi surface of $TaAs_2$, (b, e) band dispersions at $k_2 = 0$ and (c, f) band dispersions at $k_1 = 0$.

The bulk contribution to the Fermi surface comprises seven pockets, which can be represented using three Fermi surfaces. Based on the notation in reference [20], we have two electron pockets (E1) located on both sides of the k-point M2 in the bulk notation (or $\Gamma$ in the surface notation). We

also have four electron pockets (E2) on both sides of the k-point A, as well as a one-hole pocket centered at the k-point M2 (see Figure 4.13 (d and e)). To observe more clear features in the Fermi surface, we used special curvature algorithms of energy distribution curve (EDC) and momentum distribution curve (MDC) [106]. In Figure 4.14 (a-f), we define $k_1$ and $k_2$ as the coordinate of the k-space for the ($\overline{2}$ 0 1) surface orientation. By increasing the FL by 60 meV from its theoretical value, we observed improved agreement with the experimental results.

Although we achieved a satisfactory level of agreement for bulk states, some of the surface states were visible in the experimental results but not very sharp and clear. Based on the theoretical Fermi pockets, we associated the frequencies of 109, 207, and 646 T obtained by electron transport measurements with the $E_2$, H, and $E_1$ Fermi surfaces, respectively. By analyzing the DOS, we determined that the number of extra electrons required to shift the FL by +60 meV is 0.020 electrons per formula unit (see Figure 4.13 (b)). This value is relatively small, reflecting the low DOS of the semi-metallic phase. Additionally, our analysis indicated that the electron concentration ($n_e$) of $3.5 \times 10^{19}$ $cm^{-3}$ is slightly larger than the hole concentration ($n_h$) of $3.1 \times 10^{19}$ $cm^{-3}$, suggesting that the samples are weakly n-doped.

# 5

# Niobium mono-phosphide: NbP

*The interface is still the device*

*Herbert Kroemer*

**This chapter expands upon the insights provided in the article, which discussed in Ashutosh S. Wadge, Bogdan J. Kowalski, Carmine Autieri, Przemysław Iwanowski, Andrzej Hruban, Natalia Olszowska, Marcin Rosmus, Jacek Kołodziej, and Andrzej Wiśniewski, Phys. Rev. B 105, 235304 (2022).**
(* In order to compare our experimental data, appropriate permission was obtained from the corresponding journals to utilize the previously published theoretical calculations of Fermi surfaces and corresponding band structure. These calculations were then compared to our experimental data to gain valuable insights and improve our understanding of the material's electronic properties.)

The surface and interface of materials play a crucial role in determining their physical and electronic properties, particularly in the field of condensed matter physics. Due to an external perturbation such as the decoration of the surface with guest atoms, the electronic structure of a material can

be drastically altered at the surface compared to its bulk. As a result, the impact on trivial and non-trivial surface states is of significant interest to fundamental studies. Particular topological materials such as Weyl semimetals, exhibit exotic electronic behavior that is often confined to their surfaces and interfaces. Angle-resolved photoemission spectroscopy is a powerful technique for probing the electronic structure of materials at the surface and interface. By measuring the energy and momentum of photo-emitted electrons, ARPES can reveal the nature and dispersion of surface states, providing valuable insight into the underlying physics of topological materials [41]. In this chapter, we will discuss the ARPES study to investigate the effect on the electronic structure of the interface between Pb/NbP and Nb/NbP. We will demonstrate the critical role of surface effects in shaping the behavior of these materials and provide a detailed analysis of the surface states observed in ARPES measurements. Obtained results highlight the importance of surface properties and their influence on the electronic behavior of topological materials, providing a foundation for future studies and technological applications.

## 5.1 Termination dependent Fermi surface study

In this investigation, we cleaved the single crystals of NbP to produce a (0 0 1) surface under ultra-high vacuum (UHV) conditions. After a certain number of cleaving attempts, we observed that NbP crystal can be cleaved at two possible terminations Nb and P with distinct electronic structures. It has been known from the literature about these two terminations [27, 32]. The crystal structure of NbP is tetragonal and non-centrosymmetric, meaning that it lacks symmetry planes that can divide it into two mirror-image halves. As a result, its surface is polar and can have two different terminations based on the orientation of the crystal lattice. When NbP is cleaved, the surface can expose either niobium atoms or phosphorus atoms, resulting in two possible terminations. Therefore, two terminations can be observed on the surface of NbP after cleavage.

ARPES is a surface-sensitive technique applied to observe the surface states in NbP. Results in Figure 5.1 show that the P-terminated surface has spoon-like (non-trivial SS) and bow tie-shaped (trivial SS) surface states, while these shapes were not evident in the Nb-terminated surfaces. The constant energy contour of the Nb-terminated surface is non-equivalent along $\overline{\Gamma} - \overline{X}$ and $\overline{\Gamma} - \overline{Y}$. The band dispersion along $\overline{\Gamma} - \overline{X}$ for both terminations agreed with previously published data [27], as depicted in

Figure 5.1. This highlights the unique nature of electronic states on distinct cleaving planes. It is not possible for P and Nb terminations to coexist on the same cleaved surface due to the single-domain nature of NbP. The constant energy contour of the Nb-terminated surface is more complex than that of the P-terminated surface as it contains more Fermi surfaces around the projected Weyl points (WPs).

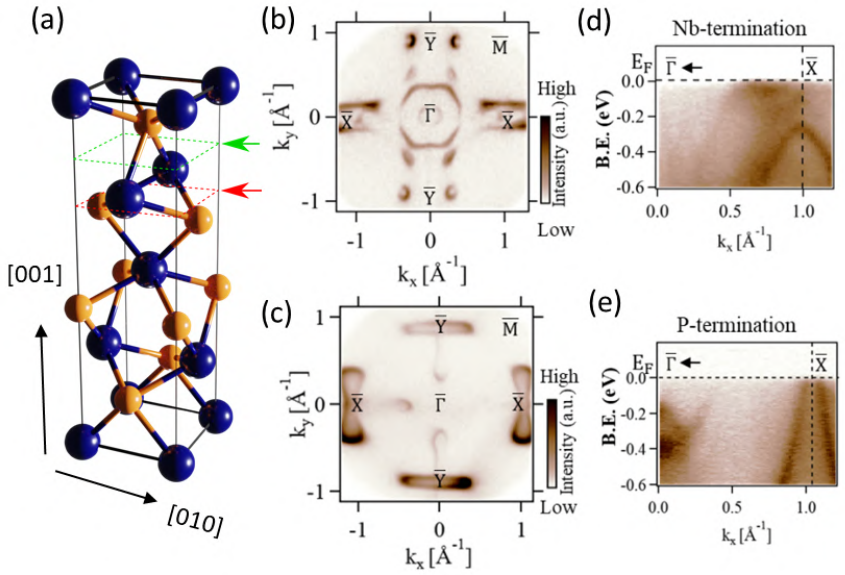


Figure 5.1: Electronic structure of NbP by ARPES (a) the tetragonal crystal structure of NbP with two easy cleaving planes indicated by two arrows with different colors, (b, c) the constant energy contours of Nb and P terminated surfaces of NbP, respectively, (d, e) band structure along $\overline{\Gamma} - \overline{X}$ directions for Nb and P terminations, respectively.

When examining P-terminated NbP, we observed two distinct types of surface states: trivial bow-tie-shaped states resulting from the presence of dangling bonds, and non-trivial spoon-like shaped states known as surface Fermi arcs (SFA), which correspond to the open Fermi surfaces and surface projection of bulk protected WPs. One interesting characteristic of SFAs is that they always originate and terminate at WPs of opposite chirality. Whereas, the Fermi surface of Nb-terminated NbP is different from P-terminated NbP (see Figure 5.2). While analyzing the electronic structure of Nb-terminated NbP, we compared our experimental results with theoretical predictions [27] and denoted the pockets as follows:

circular hole-like pocket: S5 (yellow), electron-like pocket around the $\overline{\Gamma}$ point: S6 (orange), SFAs: S8 (magenta) and S9 (cyan). SFA-related S8 are associated with W2 WPs whereas SFA-related S9 starts and ends with

W1 WPs. These SFAs are situated around the $\overline{X}$ point. Our experimental results are consistent with the theoretical predictions, as shown in Figure 5.2.

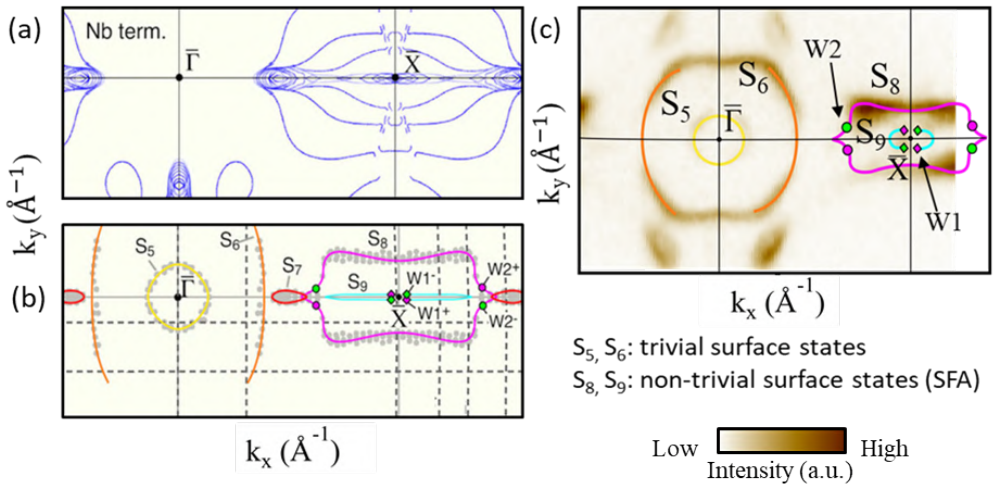


Figure 5.2: Comparison of 2D Fermi surface of Nb-terminated NbP: (a, b) the experimental Fermi surfaces and theoretically calculated Fermi surfaces of Nb-terminated [27] and (c) our experimental ARPES data indicating trivial and non-trivial surface states along with Weyl points.

## 5.2 Deposition of 1 ML Pb/P-terminated NbP

In this experiment, we decided to evaporate about 1 monolayer (ML) of lead (Pb) on the P-terminated (see graphics in Figure 5.5 (e)), clean (0 0 1) surface of NbP obtained by in situ cleaving process. To verify the successful deposition of Pb, the core-level spectrum was taken after surface decoration, which revealed Pb 5d-related peaks, thus confirming its presence on the surface (see Figure 5.5 (f)). The P-terminated surface showed bow tie-shaped trivial surface states, which were a result of the presence of dangling bonds after in situ cleaving. Additionally, spoon-like features were observed as topological SFAs. After the deposition of one monolayer of Pb, there was a significant change in the constant energy contours, affecting both trivial and nontrivial surface states. The topologically trivial bow tie-shaped features were found to be shrunken along the $\overline{\Gamma} - \overline{X}$ and $\overline{\Gamma} - \overline{Y}$ directions due to the saturation of dangling bonds, as demonstrated in Figure 5.3.

Surface Fermi arcs (SFAs) are surface features of bulk-protected WPs that are typically unaffected by the deposition of foreign elements on the surface. However, when one monolayer of Pb was deposited, the SFAs were shifted from one pair of WPs to another, connecting two adjacent surfaces Brillouin zones forming a lemniscate (or infinity) shape (see Figure 5.4 (c)). This

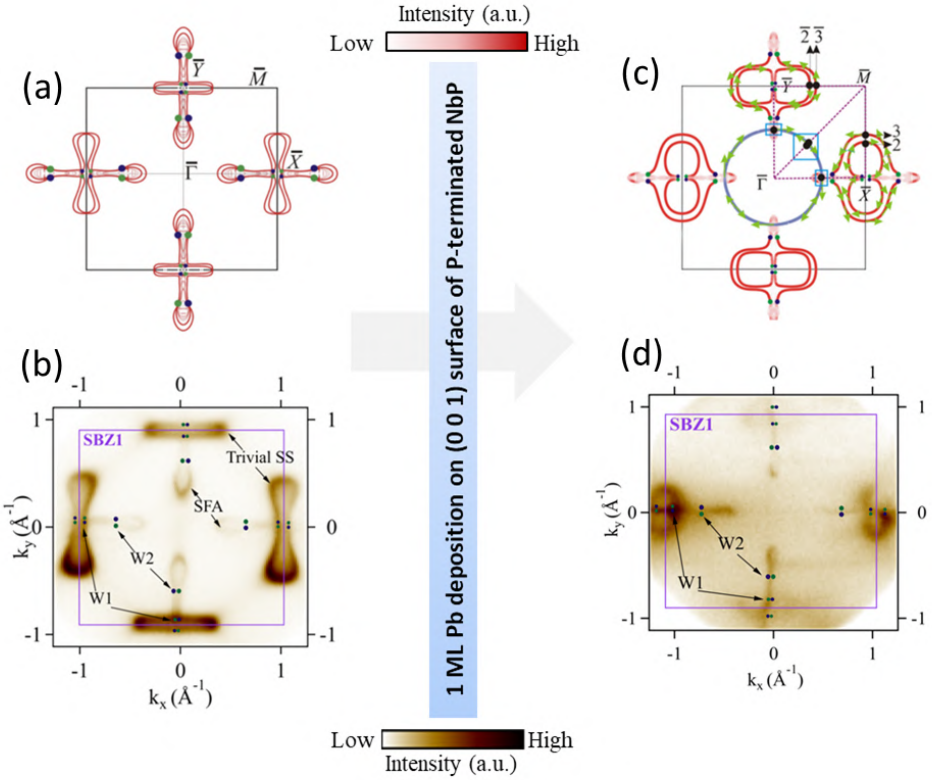


Figure 5.3: (a, c) The theoretically predicted 2D Fermi surfaces of P-terminated Weyl semimetal and modified Fermi surface by 1 atomic layer deposition of K [26] compared with our experimental data (b, d) of P-terminated NbP and modifications in the constant energy contour after 1 ML Pb deposition.

phenomenon is called the 'topological Lifshitz transition', which modifies the mirror plane for pristine P-terminated NbP from $k_x$, $k_y = 0$ to $k_x$, $k_y = \pm\pi$ a (see Figure 5.5 (I-n)). The deposited Pb atoms have 5d electrons with widely extended atomic orbitals, leading to strong hybridization with the P-terminated surface. In Figure A.1 from the Appendix, the constant energy contours for changing binding energy are plotted to show the evolution of the constant energy contours. The data indicate that only spoon-like and bow tie-shaped features are present on the pristine surface, while after the

surface decoration with 1 ML of Pb, the lemniscate shape (or infinity shape) is naturally present along the $\overline{\Gamma} - \overline{X}$ and $\overline{\Gamma} - \overline{Y}$ directions.
The modifications in the Fermi surface topology suggest that the effect of the Pb surface decoration is more complex than just introducing Pb doping. Instead, it is likely that the surface environment is changed in a way that leads to the formation of a trident shape as shown in Figure 5.5 (e and f) indicated by an arrow, including the observed surface Fermi arcs.

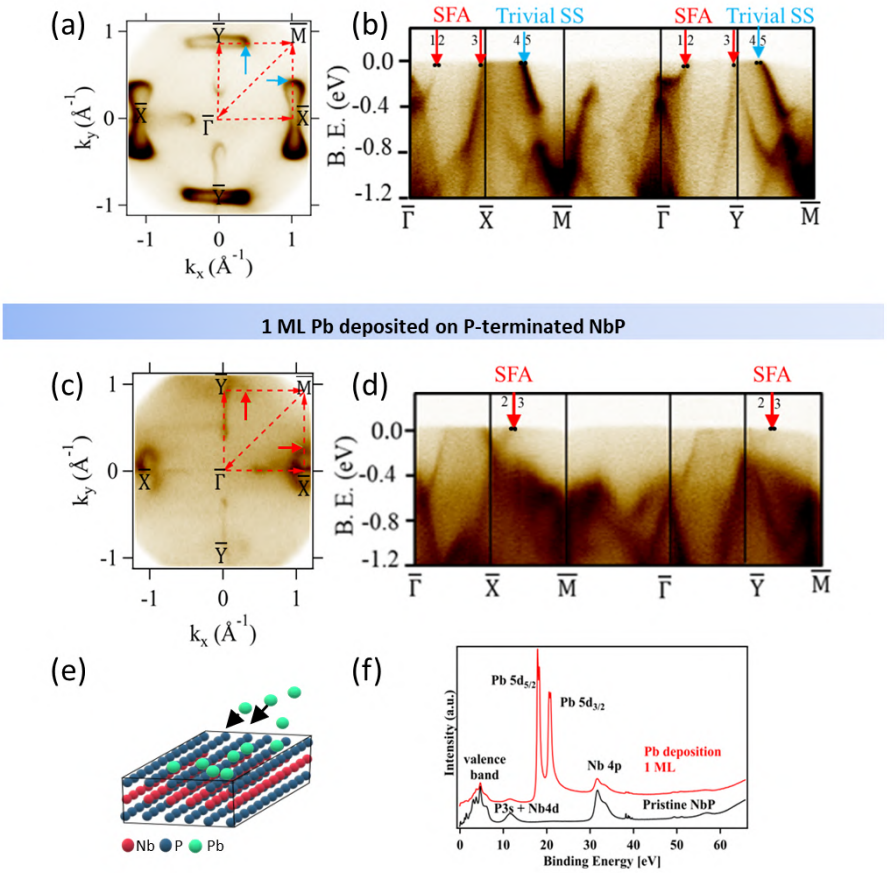


Figure 5.4: Experimental Fermi surface comparison between pristine P-terminated NbP and 1 ML Pb deposited P-terminated NbP (a, b) the constant energy contour of pure NbP and band structure shown by high symmetry path, respectively (blue arrows represent trivial and red arrow indicated the nontrivial SS), (c, d) 2D Fermi surface of Pb deposited along with corresponding band structure, respectively and (e and f) a graphical representation of deposition process and the core level spectra with 5d peaks to confirm Pb deposition.

Other band dispersions plotted in Figure 5.5 along various high symmetric

paths are in good agreement with the theoretical calculations done in the article [26].

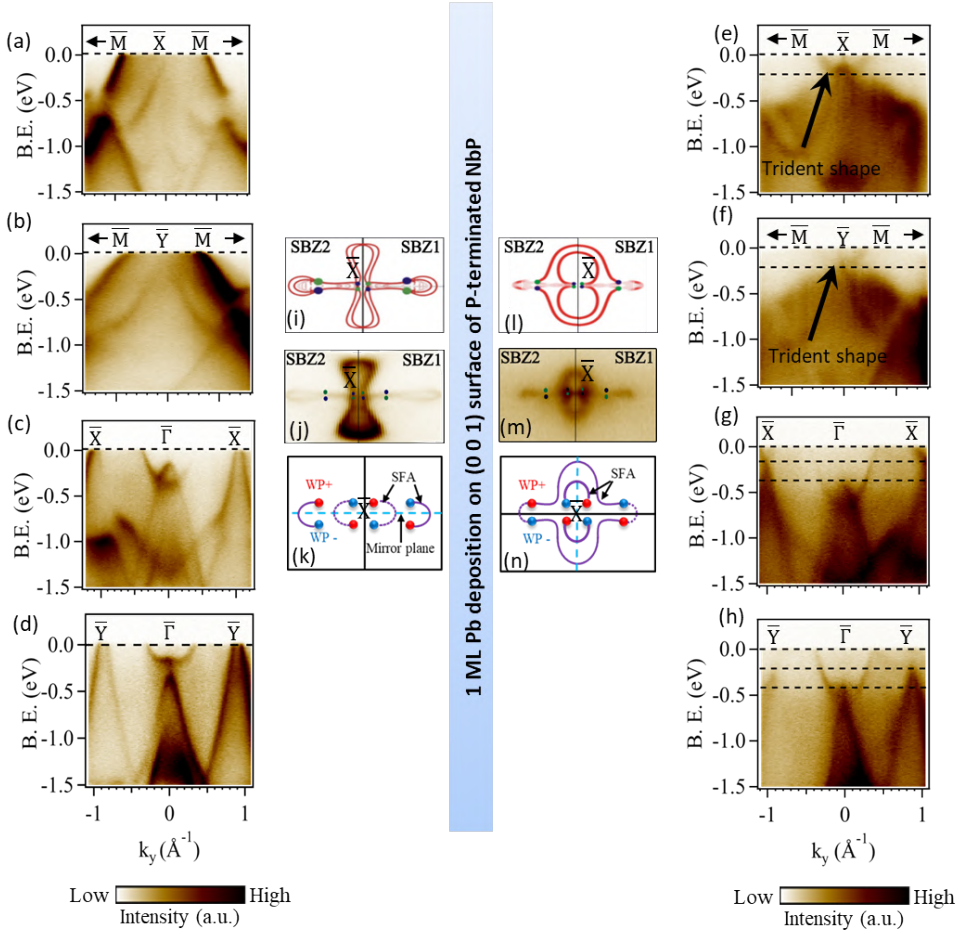


Figure 5.5: Side-by-side comparison of experimental ARPES band-structures before and after 1 ML Pb deposition on P-terminated NbP along (a, e)$\overline{M} - \overline{X} - \overline{M}$, (b, f) $\overline{M} - \overline{Y} - \overline{M}$, (c, g) $\overline{X} - \overline{\Gamma} - \overline{X}$, (d, h) $\overline{Y} - \overline{\Gamma} - \overline{Y}$, (i, l) theoretical calculations for modifications before and after the process, respectively, (j, m) experimental data compared with theory and (k, n) graphical representation of the Fermi surface modification.

## 5.3 Deposition of 1.9 ML Pb/Nb-terminated NbP

The electronic characteristics of Nb-terminated NbP differ from those of the P-terminated counterpart, as previously noted. Figure 5.6 illustrates the constant energy contour and distinctive features of Nb-terminated NbP. To provide a clearer and more detailed visualization, we utilized macro functions of 2D curvature as well as energy distribution curves (EDC), resulting in sharper ARPES data. The second derivative of EDC of Nb-terminated reveals the Fermi arcs accurately along the $\overline{\Gamma} - \overline{X}$ direction (indicated by arrows). P. Zhang, et al. [106] described that this method developed is based on mathematical curvature in 1D and 2D which is an advantage over the widely used second derivative technique. It reduces the broadness of peaks and significantly enhances the localization of extrema. Following

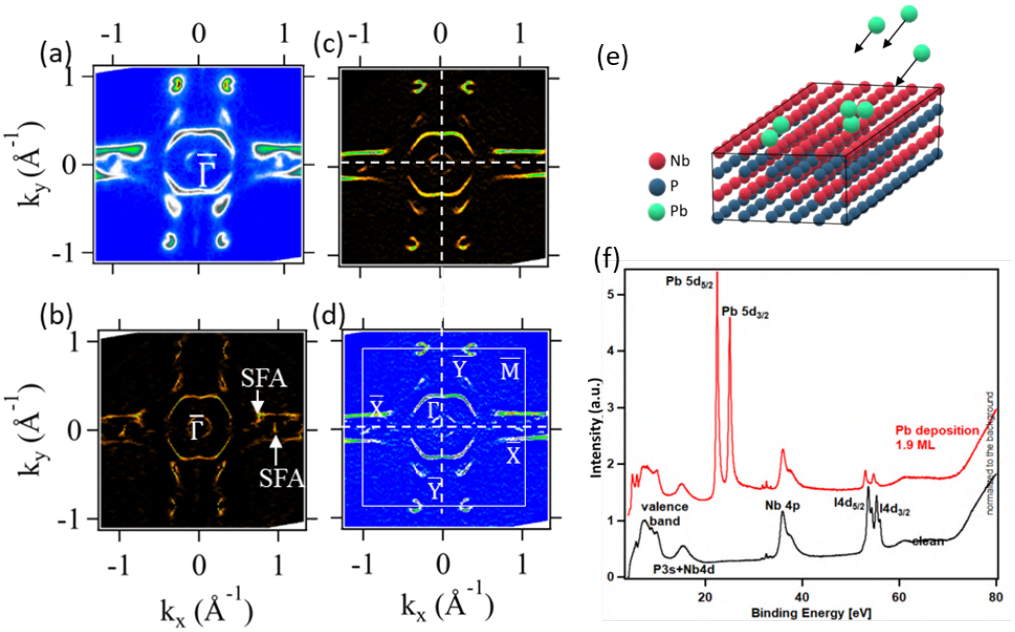


Figure 5.6: (a) Constant energy curve of Nb-terminated NbP, (b) 2D curvature of constant energy curve showing detailed features, (c) energy distribution curves (EDC) of constant energy curve as a function of $k_x$ and $k_y$, (d) second derivative of EDC of constant energy curve as a function of $k_x$ and $k_y$, (e) the pictorial representation to represent Pb deposition on Nb-terminated surface and (f) core level spectra of pristine Nb-terminated NbP and Pb deposited NbP.

our observation of the topological Lifshitz transition on P-terminated NbP induced by evaporating Pb, we decided to conduct the same process on

Nb-terminated NbP. To begin, we observed the Nb-terminated electronic structure using ARPES and then deposited Pb in situ on it. Figure 5.6 (e and f) provides a graphical representation of Pb deposition on the Nb-terminated surface, as well as a core-level spectrum showing two 5d peaks of Pb after deposition. In addition to the Pb peaks, we also observed two extra peaks indicating the presence of iodine. This is due to the use of iodine as a transport agent during the process of crystal growth, as mentioned in the chapter on crystal growth and characterization. As we know the trivial SSs are very sensitive to external perturbations hence it is wise to imagine the changes in the trivial SS on the other hand non-trivial SFAs are robust in nature. Therefore, it was interesting to investigate whether the SFAs change or not as they did in the case of P-terminated NbP.
The deposition of 1.9 ML of Pb onto the Nb-terminated surface of NbP resulted in minimal alterations to the surface states, while SFAs remained unaffected. The introduction of Pb caused the appearance of four additional

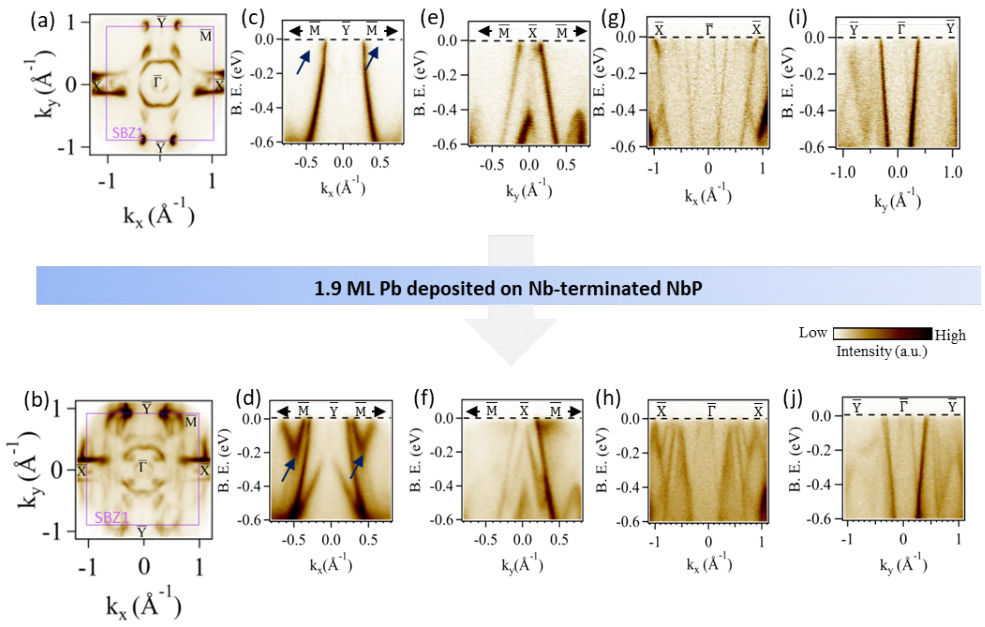


Figure 5.7: Comparison of pure Nb-terminated NbP and modified Nb-terminated NbP surfaces after 1.9 ML of Pb deposition, with constant energy contour shown for both (a) and (b), along with a comparison of band dispersion along high symmetry cuts (c, d) $\overline{M} - \overline{Y} - \overline{M}$, (e, f) $\overline{M} - \overline{X} - \overline{M}$, (g, h) $\overline{X} - \overline{\Gamma} - \overline{X}$, (i, j) $\overline{Y} - \overline{\Gamma} - \overline{Y}$.

trivial pockets alongside the pre-existing trivial hole pocket (S6) along the $\overline{\Gamma} - \overline{M}$ directions. It mainly comes from trivial bands of monolayer Pb though they are not exactly equal to pockets reported in 'F. Baumberger

et. al due to different symmetries of the Brillouin zone (square lattice in our case and hexagonal lattice in their case) [107].

Band dispersion was compared along high-symmetry paths as illustrated in Figure 5.7. Also, we observed the additional lines in constant energy contour which are connected to SFA S8 along the vertical direction (see Figure 5.8). The analysis of constant energy contour changes with binding energy (Appendix Figure A.2) revealed that the nontrivial SFAs remained unchanged. Therefore, the transition is considered an ordinary Lifshitz transition (changes only in trivial surface states), as it involves a change in the Fermi surface without altering the non-trivial topological surface states (SFAs).

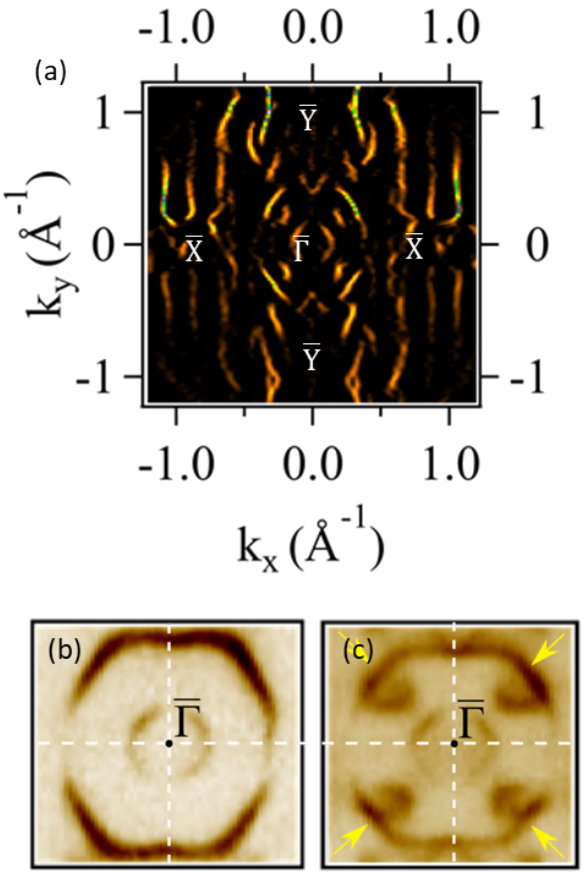


Figure 5.8: (a) 2D curvature of constant energy curve of 1.9 ML Pb/Nb-terminated surface showing modifications in SS, (b and c) the magnified S5 and S6 Fermi pockets of pristine Nb-terminated NbP and 1.9 ML Pb/Nb-terminated respectively. It shows the presence of 4 extra pockets near $\bar{\Gamma}$ point indicated by yellow arrows.

## 5.4 Deposition of 0.8 ML Nb/P-terminated NbP

After the successful experiments with Pb deposition, we were interested to evaporate Nb on both the terminations of NbP to observe changes that appear during the initial stages of formation of those interfaces even in their normal state [33]. At first, we cleaved the NbP crystal to get a (0 0 1) surface and verified the P-terminated surface by taking ARPES spectra. Nb was deposited on the same cleaned surface.

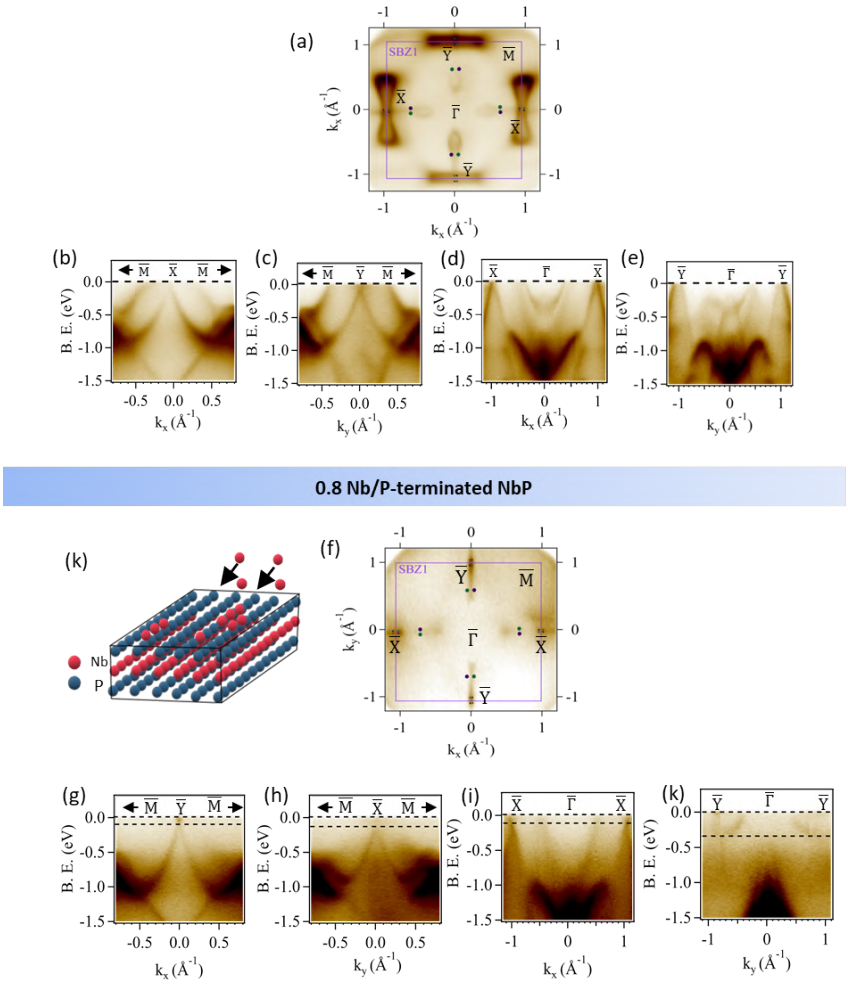


Figure 5.9: The comparative study of pure P-terminated NbP and 0.8 Nb/P-terminated NbP (a, f) constant energy contour before and after Nb deposition, (b, g) $\overline{M} - \overline{Y} - \overline{M}$, (c, h) $\overline{M} - \overline{X} - \overline{M}$, (d, i) $\overline{X} - \overline{\Gamma} - \overline{X}$, (e, k) $\overline{Y} - \overline{\Gamma} - \overline{Y}$ and (k) a graphical representation of Nb deposition on P-terminated NbP.

As explained in the chapter on experimental techniques, we have used Nb effusion cell in order to deposit Nb. An electron beam is used to evaporate the tip of the Nb wire under UHV conditions. Our findings indicate that the surface resembles a constant energy contour shown in Figure 5(c) of [31] along the $\overline{M}-\overline{X}-\overline{M}$ and the $\overline{M}-\overline{Y}-\overline{M}$ path, as illustrated in Figure 5.9. We also observed the shrinking of SFAs. This similarity suggests that the 0.8 ML Nb deposited on P-terminated NbP is situated at the critical point of the topological Lifshitz transition, but is not yet fully transformed. At this juncture, the trivial surface states contract, but is not yet completely transformed into the lemniscate shape ($\infty$-like shape).
Additionally, we observed linear dispersion along the $\overline{X}-\overline{\Gamma}-\overline{X}$ and $\overline{Y}-\overline{\Gamma}-\overline{Y}$ cuts, as depicted in Figures 5.9 (d, i, e, k), confirming the presence of WPs in the bulk both before and after Nb deposition on pristine P-terminated NbP. The 0.8 ML deposition altered the surface electronic structure of NbP, as the trivial bow tie-shaped features disappeared following surface decoration due to the saturation of dangling bonds. In appendix Figure A.3, we demonstrate a constant energy contour with changing binding energy to illustrate how the Fermi surface changed following the deposition of guest Nb atoms.

## 5.5 Deposition of 1.3 ML Nb/Nb-terminated NbP

In addition to our previous experiments, we conducted Nb deposition on Nb-terminated NbP to investigate the impact of Nb atoms on the electronic structure of the material. However, the resulting ARPES spectra were observed to be distorted and less defined on the Nb-terminated surface after Nb deposition. One possible explanation for this observation is the introduction of lattice distortions or defects in the NbP crystal due to the deposition of Nb atoms. The difference in crystal structure and lattice constant between Nb and NbP can cause strain and stress on the surface, leading to the formation of defects that can affect the electronic structure. Another potential cause for the distorted ARPES spectra is the formation of Nb clusters or islands on the surface, which can also introduce lattice distortions and alter the electronic properties. Moreover, the deposition of Nb atoms can lead to the thickening of the Nb termination, which modifies the band structure and surface potential, potentially affecting the electronic structure of the material.

These observations provide insights into the impact of surface terminations and deposited elements on the electronic structure of NbP, which can

have important implications for the development of electronic devices based on this material.

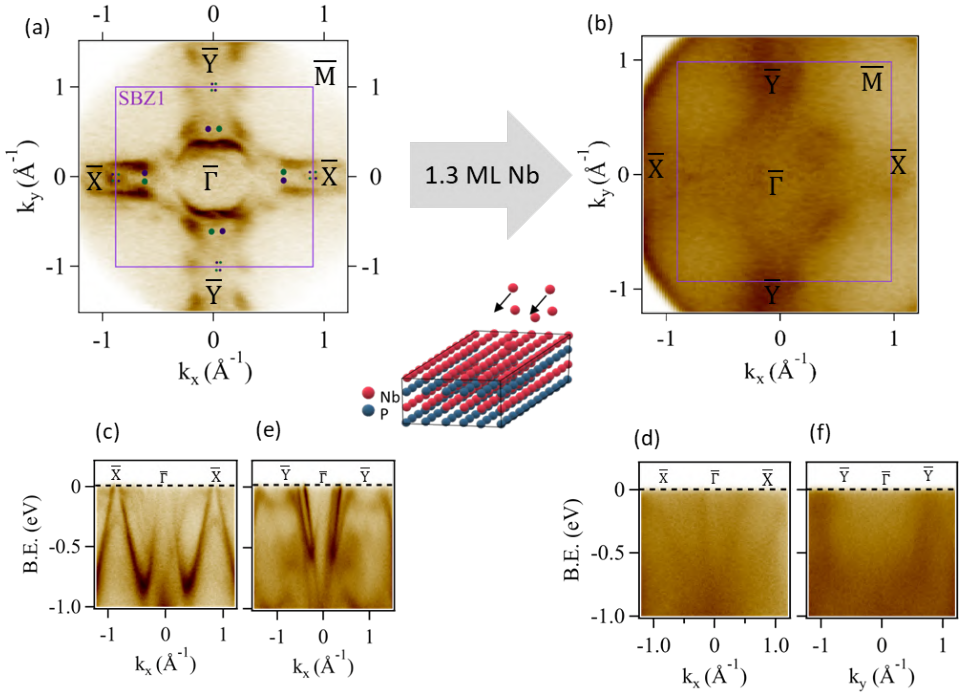


Figure 5.10: Side by side comparison of (a) pristine Nb-terminated NbP and (b) 1.3 ML Nb deposited NbP showing band dispersions along (c, d) $\overline{X}-\overline{\Gamma}-\overline{X}$ and (e, f) $\overline{Y}-\overline{\Gamma}-\overline{Y}$ respectively also in the middle part there is a graphical visualization of Nb deposition on Nb-terminated surface.

# 6

# Conclusions

We were able to probe the electronic properties of $TaAs_2$ by electron transport and ARPES studies. We successfully obtained ARPES data on $TaAs_2$ for the very first time. The good quality single crystals of $TaAs_2$ were grown by the chemical vapor transport technique. All the electron transport and ARPES measurements were performed along $(\overline{2}\ 0\ 1)$ orientation which has the lowest value of cleaving energy. The carriers present in the sample showed strong charge carrier compensation and consequently, it showed the non-saturated MR ($\sim$ 14000%) at 1.6 K and 9 T. Despite having a lower residual resistivity ratio as compared to previously published literature, our crystals displayed significant Shubnikov-de Haas oscillations at helium temperatures, enabling a detailed analysis of the material's band structure. Notably, these oscillations exhibited pronounced anisotropy in the angle-dependent study, indicating elliptical Fermi surfaces. These findings are in good agreement with ARPES results and ab initio calculations, confirming the presence of multiple conducting carriers in $TaAs_2$. Additionally, mobility spectrum analysis showed four peaks related to two kinds of electrons and holes (i.e. carriers with different values of mobility) participating in the total conductivity. The experimental band structure cuts along $[\overline{2}\ 0\ 1]$ indicate that the observed features can be attributed to a combination of surface states and bulk states projected onto the surface. The ARPES results provided for the coexistence of both trivial and topological surface states in $TaAs_2$, highlighting the diverse nature of electronic states in the

material. We identified seven Fermi surface pockets in the experimental diagrams, consistent with the bulk pockets of the theoretically calculated Fermi surface shown by the constant energy contour. The Fermi level of the theoretically calculated 2D Fermi surface was adjusted to 60 meV above the Fermi energy in order to have the best match with ARPES data.

Furthermore, the possibility of Fermi arc manipulation by covering the surface of NbP with heavy elements was observed via the ARPES technique. The good-quality crystals of NbP were prepared using the same CVT method supported by a high-quality ARPES spectrum. ARPES study showed the two different electronic structures in NbP when cleaved along [0 0 1] in the different trials. We have observed significant modifications in both trivial and nontrivial surface states in 1 ML/Pb-deposited, P-terminated NbP as a result of a topological Lifshitz transition (TLT) in which surface Fermi arcs exchanged the pair of Weyl points to which they were connected by joining two adjacent Brillouin zone. These modifications were particularly evident in the surface Fermi arcs, while the Weyl points remained unaffected by the changes in the surface environment. Previous investigations have illustrated the robustness of WPs against the deposition of light elements (with low SOC). This is noteworthy, as heavy elements introduce a stronger perturbation to the electronic structure due to their larger SOC and greater electronic hybridization. The remarkable stability of WPs stems from their topological protection in the bulk, minimally impacted by surface covers. The ability to manipulate and control the SFAs can be used in electronics and spintronics applications.

The deposition of approximately 0.8 monolayers (ML) of Nb was insufficient to induce a complete transformation of the system in accordance with the TLT. However, the system did reach the Lifshitz transition point, suggesting a significant impact of 0.8 ML Nb on its electronic properties. In the case of Nb-terminated NbP covered with 1.9 ML of Pb, we observed an ordinary Lifshitz transition taking place. Interestingly, during this transition, the topological surface Fermi arcs remained unchanged. However, we also observed the emergence of additional trivial pockets in the electronic structure. These additional pockets can be attributed to the individual characteristics of both Pb and the Nb-terminated NbP surface, indicating a complex interplay between the two materials during the Lifshitz transition. 1.3 ML Nb on the Nb-terminated surface created distortions in the lattice and blurred the spectra.

The performed studies showed that the electronic structure of NbP can be effectively influenced and manipulated by covering its surface with heavy elements. On the subsequent page, Figure 6.1 presents a summary of the various Lifshitz transitions.

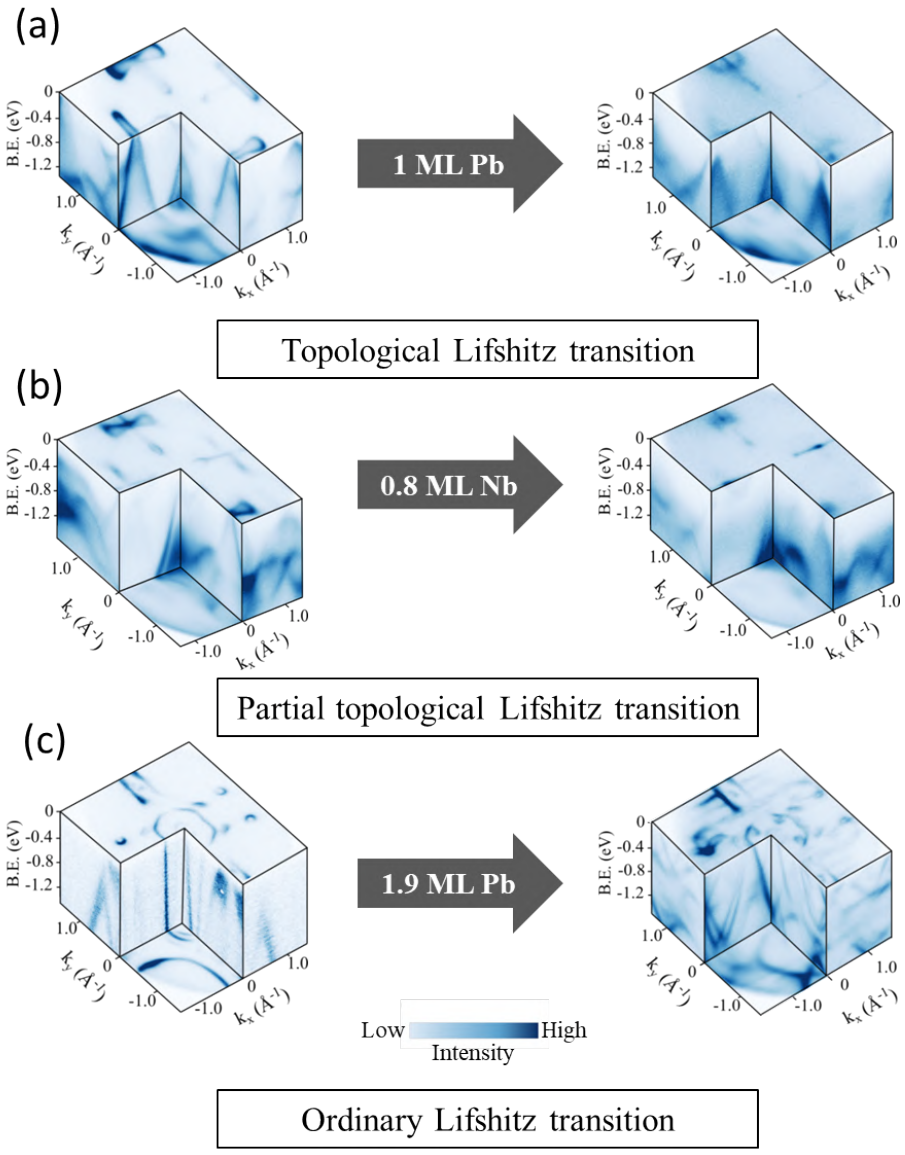


Figure 6.1: The summary of the results in the form of 3D intensity plots in which (a) shows the topological Lifshitz transition (TLT) when 1 ML of Pb deposited on P-terminated NbP, (b) shows partial TLT when 0.8 ML of Nb deposited on P-terminated NbP and (c) shows ordinary Lifshitz transition when 1.9 ML of Pb deposited on the top of Nb-terminated surface.

# A

# Appendix

This part of the dissertation contains three figures concerned with the topological Lifshitz transition in NbP

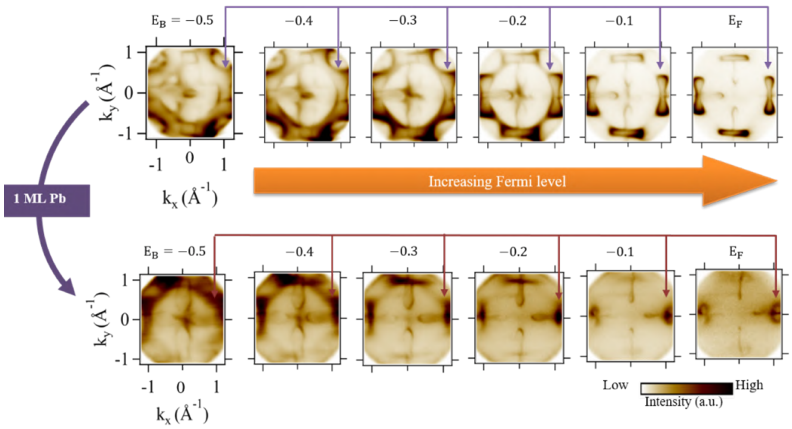


Figure A.1: Comparison of 2D Fermi surfaces between pristine P-terminated NbP and 1 ML Pb decorated P-terminated NbP showing the modifications are completely different than the pristine NbP.

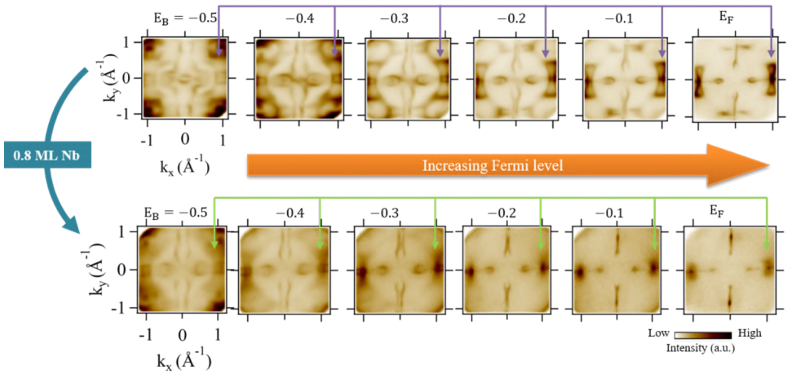


Figure A.2: Comparison of 2D Fermi surfaces between pristine P-terminated NbP and 0.8 ML Nb deposited on P-terminated NbP indicating the vanished trivial Fermi surface states along with system at the critical point of topological Lifshitz transition (TLT).

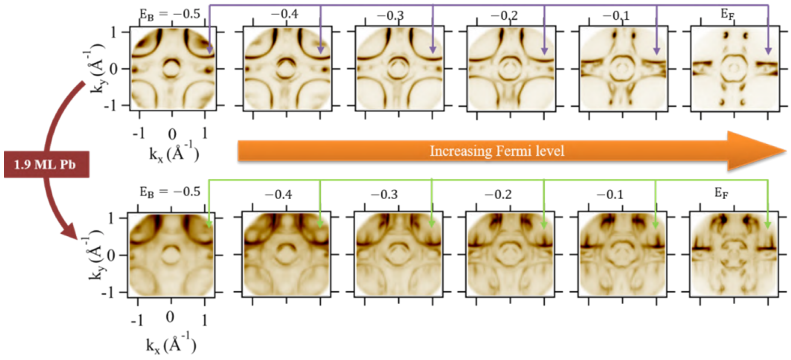


Figure A.3: Comparison of constant energy contours of pristine P-terminated NbP and 1.9 ML Pb deposited on Nb-terminated NbP showing ordinary Lifshitz transition with only modified trivial surface states while non-trivial SFAs remain unchanged.

# Bibliography


[1] K. v. Klitzing, G. Dorda, and M. Pepper. New method for high-accuracy determination of the fine-structure constant based on quantized Hall resistance. *Phys. Rev. Lett.*, **45**:494–497, 1980.

[2] D. J. Thouless, M. Kohmoto, M. P. Nightingale, and M. den Nijs. Quantized Hall conductance in a two-dimensional periodic potential. *Phys. Rev. Lett.*, **49**:405–408, 1982.

[3] F. D. M. Haldane. Model for a quantum Hall effect without Landau levels: condensed-matter realization of the "parity anomaly". *Phys. Rev. Lett.*, **61**:2015–2018, 1988.

[4] S. Murakami, N. Nagaosa, and S.-C. Zhang. Spin-Hall insulator. *Phys. Rev. Lett.*, **93**:156804, 2004.

[5] Markus König, Steffen Wiedmann, Christoph Brüne, Andreas Roth, Hartmut Buhmann, Laurens W. Molenkamp, Xiao-Liang Qi, and Shou-Cheng Zhang. Quantum spin Hall insulator state in HgTe quantum wells. *Science*, **318**(5851):766–770, 2007.

[6] R. Roy. Topological phases and the quantum spin Hall effect in three dimensions. *Phys. Rev. B*, **79**:195322, 2009.

[7] Y. Ran, Y. Zhang, and A. Vishwanath. One-dimensional topologically protected modes in topological insulators with lattice dislocations. *Nat. Phys.*, **5**(4):298–303, 2009.

[8] Y. Zhang, K. He, C.-Z. Chang, C.-L. Song, L.-L. Wang, X. Chen, J.-F. Jia, Z. Fang, X. Dai, W.-Y. Shan, et al. Crossover of the three-dimensional topological insulator $Bi_2Se_3$ to the two-dimensional limit. *Nat. Phys.*, **6**(8):584–588, 2010.

[9] J. E. Moore. The birth of topological insulators. *Nature*, **464**(7286):194–198, 2010.

[10] P. Dziawa, B. J. Kowalski, K. Dybko, R. Buczko, A. Szczerbakow, M. Szot, E. Łusakowska, T. Balasubramanian, B. M. Wojek, M. H. Berntsen, et al. Topological crystalline insulator states in $Pb_{1-x}Sn_xSe$. *Nat. Mater.*, **11**(12):1023–1027, 2012.

[11] A. A. Burkov. Topological semimetals. *Nat. Mater.*, **15**(11):1145–1148, 2016.

[12] B. Q. Lv, T. Qian, and H. Ding. Experimental perspective on three-dimensional topological semimetals. *Rev. Mod. Phys.*, **93**:025002, 2021.

[13] B. Wang, B. Singh, B. Ghosh, W.-C. Chiu, M. M. Hosen, Q. Zhang, L. Ying, M. Neupane, A. Agarwal, H. Lin, and A. Bansil. Topological crystalline insulator state with type II Dirac fermions in transition metal dipnictides. *Phys. Rev. B*, **100**:205118, 2019.

[14] S. Sun, Z. Song, H. Weng, and X. Dai. Topological metals induced by the Zeeman effect. *Phys. Rev. B*, **101**:125118, 2020.

[15] Y. Luo, R. D. McDonald, P. F. S. Rosa, B. Scott, N. Wakeham, N. J. Ghimire, E. D. Bauer, J. D. Thompson, and F. Ronning. Anomalous electronic structure and magnetoresistance in $TaAs_2$. *Sci. Rep.*, **6**(1):1–7, 2016.

[16] H. Wang, C. Pei, H. Su, Z. Yu, M. Li, W. Xia, X. Liu, Q. Liang, J. Zhao, C. Zhou, N. Yu, X. Wang, Z. Zou, Lin Wang, Q. Y., and Y. Guo. Robust magnetoresistance in $TaAs_2$ under pressure up to about 37 GPa. *Appl. Phys. Lett.*, **115**(12), 2019.

[17] Z. Yuan, H. Lu, Y. Liu, J. Wang, and S. Jia. Large magnetoresistance in compensated semimetals $TaAs_2$ and $NbAs_2$. *Phys. Rev. B*, **93**:184405, 2016.

[18] D. Gresch, Q. Wu, G. W. Winkler, and A. A. Soluyanov. Hidden Weyl points in centrosymmetric paramagnetic metals. *New J. Phys.*, **19**(3):035001, 2017.

[19] J. Sun and D. J. Singh. First-principles study of tantalum-arsenic binary compounds. *J. Appl. Phys.*, **121**(1), 2017.

[20] T. A. Butcher, J. Hornung, T. Förster, M. Uhlarz, J. Klotz, I. Sheikin, J. Wosnitza, and D. Kaczorowski. Fermi surface investigation of the semimetal $TaAs_2$. *Phys. Rev. B*, **99**:245112, 2019.

[21] v. H. Weyl. Elektron und gravitation. I. *Surveys in High Energy Physics*, **5**(3):261–267, 1986.

[22] Binghai Yan and Claudia Felser. Topological materials: Weyl semimetals. *Annu. Rev. Condens. Matter Phys.*, **8**(1):337–354, 2017.

[23] S.-M. Huang, S.-Y. Xu, I. Belopolski, C.-C. Lee, G. Chang, B. Wang, N. Alidoust, G. Bian, M. Neupane, C. Zhang, et al. A Weyl fermion semimetal with surface fermi arcs in the transition metal monopnictide TaAs class. *Nat. Comm.*, **6**(1):7373, 2015.

[24] H. Yang, A. Liang, C. Chen, C. Zhang, N. B. M. Schroeter, and Y. Chen. Visualizing electronic structures of quantum materials by angle-resolved photoemission spectroscopy. *Nat. Rev. Mat.*, **3**(9):341–353, 2018.

[25] J. A. Sobota, Y. He, and Z.-X. Shen. Angle-resolved photoemission studies of quantum materials. *Rev. Mod. Phys.*, **93**:025006, 2021.

[26] Y. Sun, S.-C. Wu, and B. Yan. Topological surface states and Fermi arcs of the noncentrosymmetric Weyl semimetals TaAs, TaP, NbAs, and NbP. *Phys. Rev. B*, **92**:115428, 2015.

[27] S. Souma, Z. Wang, H. Kotaka, T. Sato, K. Nakayama, Y. Tanaka, H. Kimizuka, T. Takahashi, K. Yamauchi, T. Oguchi, K. Segawa, and Y. Ando. Direct observation of nonequivalent Fermi-arc states of opposite surfaces in the noncentrosymmetric Weyl semimetal NbP. *Phys. Rev. B*, **93**:161112, 2016.

[28] A. A. Nikolaeva, L. A. Konopko, T. E. Huber, A. K. Kobylianskaya, and Gh. I. Para. Lifshitz topological transitions, induced by doping and deformation in single-crystal bismuth wires. *Low Temp. Phys.*, **43**(2):257–263, 2017.

[29] G. E. Volovik. Topological Lifshitz transitions. *Low Temp. Phys.*, **43**(1):47–55, 2017.

[30] A. Lau, K. Koepernik, J. van den Brink, and C. Ortix. Generic coexistence of Fermi arcs and Dirac cones on the surface of time-reversal invariant Weyl semimetals. *Phys. Rev. Lett.*, **119**:076801, 2017.

[31] H. F. Yang, L. X. Yang, Z. K. Liu, Y. Sun, C. Chen, H. Peng, M. Schmidt, D. Prabhakaran, B. A. Bernevig, C. Felser, et al. Topological Lifshitz transitions and Fermi arc manipulation in Weyl semimetal NbAs. *Nat. Comm.*, **10**(1):3478, 2019.

[32] A. Bedoya-Pinto, D. Liu, H. Tan, A. K. Pandeya, K. Chang, J. Zhang, and S. S. P. Parkin. Large Fermi-energy shift and suppression of

trivial surface states in NbP Weyl semimetal thin films. *Adv. Mater.*, **33**(21):2008634, 2021.

[33] G. Grabecki, A. Dąbrowski, P. Iwanowski, A. Hruban, B. J. Kowalski, N. Olszowska, J. Kołodziej, M. Chojnacki, K. Dybko, A. Łusakowski, T. Wojtowicz, T. Wojciechowski, R. Jakieła, and A. Wiśniewski. Conductance spectra of (Nb, Pb, In)/NbP superconductor/Weyl semimetal junctions. *Phys. Rev. B*, **101**:085113, 2020.

[34] K. Wrześniewski, I. Weymann, N. Sedlmayr, and T. Domański. Dynamical quantum phase transitions in a mesoscopic superconducting system. *Phys. Rev. B*, **105**:094514, 2022.

[35] C. L. Kane and E. J. Mele. $Z_2$ topological order and the quantum spin Hall effect. *Phys. Rev. Lett.*, **95**(14):146802, 2005.

[36] B. A. Bernevig, T. L. Hughes, and S.-C. Zhang. Quantum spin Hall effect and topological phase transition in HgTe quantum wells. *science*, **314**(5806):1757–1761, 2006.

[37] H. Zhang, C.-X. Liu, X.-L. Qi, X. Dai, Z. Fang, and S.-C. Zhang. Topological insulators in $Bi_2Se_3$, $Bi_2Te_3$ and $Sb_2Te_3$ with a single Dirac cone on the surface. *Nat. Phys.*, **5**(6):438–442, 2009.

[38] Y. L. Chen, J. G. Analytis, J.-H. Chu, Z. K. Liu, S.-K. Mo, X.-L. Qi, H. J. Zhang, D. H. Lu, X. Dai, Z. Fang, et al. Experimental realization of a three-dimensional topological insulator, $Bi_2Te_3$. *science*, **325**(5937):178–181, 2009.

[39] D. Hsieh, D. Qian, L. Wray, Y Xia, Yew San Hor, R. J. Cava, and M. Z. Hasan. A topological Dirac insulator in a quantum spin Hall phase. *Nature*, **452**(7190):970–974, 2008.

[40] D. Hsieh, Y. Xia, L. Wray, D. Qian, A. Pal, J. H. Dil, J. Osterwalder, F. Meier, G. Bihlmayer, C. L. Kane, et al. Observation of unconventional quantum spin textures in topological insulators. *Science*, **323**(5916):919–922, 2009.

[41] A. Damascelli. Probing the electronic structure of complex systems by ARPES. *Phys. Scr.*, **2004**(T109):61, 2004.

[42] L. V. Baiqing, Q. Tian, and D Hong. Angle-resolved photoemission spectroscopy and its application to topological materials. *Nat. Rev. Phys.*, **1**(10):609–626, 2019.

[43] M. Rosmus, N. Olszowska, Z. Bukowski, P. Starowicz, P. Piekarz, and A. Ptok. Electronic band structure and surface states in Dirac semimetal $LaAgSb_2$. *Materials*, **15**(20), 2022.

[44] C. Herring. Accidental degeneracy in the energy bands of crystals. *Phys. Rev.*, **52**(4):365, 1937.

[45] S.-Y. Xu, I. Belopolski, N. Alidoust, M. Neupane, G. Bian, C. Zhang, R. Sankar, G. Chang, Z. Yuan, C. C. Lee, et al. Discovery of a Weyl fermion semimetal and topological Fermi arcs. *Science*, **349**(6248):613–617, 2015.

[46] S.-Y. Xu, N. Alidoust, I. Belopolski, Z. Yuan, G. Bian, T.-R. Chang, H. Zheng, V. N. Strocov, D. S. Sanchez, G. Chang, et al. Discovery of a Weyl fermion state with Fermi arcs in niobium arsenide. *Nat. Phys.*, **11**(9):748–754, 2015.

[47] M. Z. Hasan, S.-Y. Xu, I. Belopolski, and S.-M. Huang. Discovery of Weyl fermion semimetals and topological Fermi arc states. *Annu. Rev. Condens. Matter Phys.*, **8**:289–309, 2017.

[48] A. A. Burkov and L. Balents. Weyl semimetal in a topological insulator multilayer. *Phys. Rev. Lett.*, **107**:127205, 2011.

[49] N. P. Armitage, E. J. Mele, and A. Vishwanath. Weyl and Dirac semimetals in three-dimensional solids. *Rev. Mod. Phys.*, **90**:015001, 2018.

[50] H. B. Nielsen and M. Ninomiya. Absence of neutrinos on a lattice:(I). proof by homotopy theory. *Nucl. Phys. B.*, **185**(1):20–40, 1981.

[51] P. R. Wallace. The band theory of graphite. *Phys. Rev.*, **71**(9):622, 1947.

[52] J. C. Slonczewski and P. R. Weiss. Band structure of graphite. *Phys. Rev.*, **109**(2):272, 1958.

[53] J. W. McClure. Diamagnetism of graphite. *Phys. Rev.*, **104**(3):666, 1956.

[54] Shuichi M., Motoaki H., Ryo O., and Takashi M. Emergence of topological semimetals in gap closing in semiconductors without inversion symmetry. *Sci. Adv.*, **3**(5):e1602680, 2017.

[55] L. Balents. Weyl electrons kiss. *Physics*, **4**:36, 2011.

[56] V. Peri, T. Dubček, A. Valenti, R. Ilan, and S. D. Huber. Weyl orbits without an external magnetic field. *Phys. Rev. B*, **101**:235117, 2020.

[57] C. Zhang, Y. Zhang, H.-Z. Lu, X. C. Xie, and F. Xiu. Cycling Fermi arc electrons with Weyl orbits. *Nat. Rev. Phys.*, **3**(9):660–670, 2021.

[58] S.-Y. Xu, I. Belopolski, Sanchez D. S., Zhang C., G. Chang, C. Guo, G. Bian, Z. Yuan, H. Lu, T.-R. Chang, Shibayev P. P., M. L. Prokopovych, N. Alidoust, H. Zheng, Lee C. C., S. M. Huang, R. Sankar, F. Chou, C.-H. Hsu, H.-T. Jeng, A Bansil, T. Neupert, V. N. Strocov, H. Lin, S. Jia, and M. Z. Hasan. Experimental discovery of a topological Weyl semimetal state in TaP. *Sci. Adv.*, **1**(10):e1501092, 2015.

[59] G. Chang, S.-Y. Xu, H. Zheng, C.-C. Lee, S.-M. Huang, I. Belopolski, D. S. Sanchez, G. Bian, N. Alidoust, T.-R. Chang, C.-H. Hsu, H.-T. Jeng, A. Bansil, H. Lin, and M. Z. Hasan. Signatures of Fermi arcs in the quasiparticle interferences of the Weyl semimetals TaAs and NbP. *Phys. Rev. Lett.*, **116**:066601, 2016.

[60] X. Wan, A. M. Turner, A. Vishwanath, and S. Y. Savrasov. Topological semimetal and Fermi-arc surface states in the electronic structure of pyrochlore iridates. *Phys. Rev. B*, **83**:205101, 2011.

[61] A. A. Soluyanov, D. Gresch, Z. Wang, Q. Wu, M. Troyer, X. Dai, and B. A. Bernevig. Type-II Weyl semimetals. *Nature*, **527**(7579):495–498, 2015.

[62] P. Li, Y. Wen, X. He, Q. Zhang, C. Xia, Z.-M. Yu, S. A. Yang, Z. Zhu, H. N. Alshareef, and X.-X. Zhang. Evidence for topological type II Weyl semimetal $WTe_2$. *Nat. Comm.*, **8**(1):2150, 2017.

[63] J. Jiang, Z. K. Liu, Y. Sun, H. F. Yang, C. R. Rajamathi, Y. P. Qi, L. X. Yang, C. Chen, H. Peng, C. C. Hwang, et al. Signature of type II Weyl semimetal phase in $MoTe_2$. *Nat. Comm.*, **8**(1):13973, 2017.

[64] S. Paul, S. Talukdar, Ravi S. Singh, and S. Saha. Topological phase transition in $MoTe_2$: A review. *Phys. Status Solidi RRL*.

[65] B. Q. Lv, N. Xu, H. M. Weng, J. Z. Ma, P. Richard, X. C. Huang, L. X. Zhao, G. F. Chen, C. E. Matt, F. Bisti, et al. Observation of Weyl nodes in TaAs. *Nat. Phys.*, **11**(9):724–727, 2015.

[66] C. Shekhar, A. K. Nayak, Y. Sun, M. Schmidt, M. Nicklas, I. Leermakers, U. Zeitler, Y. Skourski, J. Wosnitza, Z. Liu, et al. Extremely large magnetoresistance and ultrahigh mobility in the topological Weyl semimetal candidate NbP. *Nat. Phys.*, **11**(8):645–649, 2015.

[67] T. Cichorek, Ł Bochenek, J. Juraszek, Y. V. Sharlai, and G. P Mikitik. Detection of relativistic fermions in Weyl semimetal TaAs by magnetostriction measurements. *Nat. Comm.*, **13**(1):3868, 2022.

[68] A. B. Pippard. *Magnetoresistance in metals*, volume **2**. Cambridge University Press, 1989.

[69] Y. Luo, N. J. Ghimire, M. Wartenbe, Hongchul Choi, M. Neupane, R. D. McDonald, E. D. Bauer, J. Zhu, J. D. Thompson, and F. Ronning. Electron-hole compensation effect between topologically trivial electrons and nontrivial holes in NbAs. *Phys. Rev. B*, **92**:205134, 2015.

[70] D. Shoenberg. *Magnetic oscillations in metals*. Cambridge University Press, 2009.

[71] J. Hu, S.-Y. Xu, N. Ni, and Z. Mao. Transport of topological semimetals. *Annu. Rev. Mater. Res.*, **49**(1):207–252, 2019.

[72] A. C. Potter, I. Kimchi, and A. Vishwanath. Quantum oscillations from surface Fermi arcs in Weyl and Dirac semimetals. *Nat. Comm.*, **5**(1):5161, 2014.

[73] K. Hwang, W.-R. Lee, and K. Park. Electric quantum oscillations in Weyl semimetals. *Phys. Rev. Res.*, **3**:033132, 2021.

[74] M. Komada, H. Murakawa, M. S. Bahramy, T. Kida, K. Yokoi, Y. Narumi, K. Kindo, M. Hagiwara, H. Sakai, and N. Hanasaki. Angle-dependent nontrivial phase in the Weyl semimetal NbAs with anisotropic Fermi surface. *Phys. Rev. B*, **101**:045135, 2020.

[75] W. Zhao and X. Wang. Berry phase in quantum oscillations of topological materials. *Adv. Phys.: X.*, **7**(1):2064230, 2022.

[76] D. T. Son and B. Z. Spivak. Chiral anomaly and classical negative magnetoresistance of Weyl metals. *Phys. Rev. B*, **88**:104412, 2013.

[77] R. D. Dos Reis, M. O. Ajeesh, N. Kumar, F. Arnold, C. Shekhar, M. Naumann, M. Schmidt, M. Nicklas, and E. Hassinger. On the search for the chiral anomaly in Weyl semimetals: the negative longitudinal magnetoresistance. *New J. Phys.*, **18**(8):085006, 2016.

[78] J. Gooth, A. C. Niemann, T. Meng, A. G. Grushin, K. Landsteiner, B. Gotsmann, F. Menges, M. Schmidt, C. Shekhar, V. Süß, et al. Experimental signatures of the mixed axial–gravitational anomaly in the Weyl semimetal NbP. *Nature*, **547**(7663):324–327, 2017.

[79] J. Yang, W. L. Zhen, D. D. Liang, Y. J. Wang, X. Yan, S. R. Weng, J. R. Wang, W. Tong, L. Pi, W. K. Zhu, and C. J. Zhang. Current jetting distorted planar Hall effect in a Weyl semimetal with ultrahigh mobility. *Phys. Rev. Mater.*, **3**:014201, 2019.

[80] C. Gessner, J. Kentmann, G. Fabricius, S. Göbel, and V. Cordus. *De Omni Rervm Fossilivm Genere, Gemmis, Lapidibvs, Metallis, Et Hvivsmodi: Libri Aliqvot, Plerique Nvnc Primvm Editi*, volume **3**. Iacobus Gesnerus, 2022.

[81] S. F. Robert. Crystal growth through the ages: A historical perspective. In Tatau N., editor, *Handbook of Crystal Growth (Second Edition)*, pages 1–83. Elsevier, Boston, second edition edition, 2015.

[82] B. Michael, G. Robert, S. Marcus, and S. Peer. *Chemical Vapor Transport Reactions*. De G., Berlin, Boston, 2012.

[83] N. Pistawala, D. Rout, K. Saurabh, R. Bag, K. Karmakar, L. Harnagea, and S. Singh. Crystal growth of quantum materials: A review of selective materials and techniques. *Bull. Mater. Sci.*, **45**:1–20, 2022.

[84] J. Friedrich. Methods for bulk growth of inorganic crystals: Crystal growth. In *Reference Module in Materials Science and Materials Engineering*. Elsevier, 2016.

[85] J. L. Schmehr and S. D. Wilson. Active crystal growth techniques for quantum materials. *Annu. Rev. Mater. Res.*, **47**:153–174, 2017.

[86] N. Kumar, S. N. Guin, K. Manna, C. Shekhar, and C. Felser. Topological quantum materials from the viewpoint of chemistry. *Chem. Rev.*, **121**(5):2780–2815, 2020.

[87] P. Schmidt, M. Binnewies, R. Glaum, and M. Schmidt. Chemical vapor transport reactions–methods, materials, modeling. In Sukarno Olavo Ferreira, editor, *Advanced Topics on Crystal Growth*, chapter 9. IntechOpen, Rijeka, 2013.

[88] C.-H. Su and C.-H. Su. Fundamentals of physical vapor transport process. *Vapor Crystal Growth and Characterization: ZnSe and Related II–VI Compound Semiconductors*, pages 9–38, 2020.

[89] Z. Li, H. Chen, S. Jin, D. Gan, W. Wang, L. Guo, and X. Chen. Weyl semimetal TaAs: crystal growth, morphology, and thermodynamics. *Cryst. Growth Des.*, **16**(3):1172–1175, 2016.

[90] X.-L. Liu, H.-Y. Wang, H. Su, Z.-H. Yu, and Y.-F. Guo. Nontrivial topological states in the tantalum dipnictides $TaX_2$ (X = As, P). *Tungsten*, **2**:251–260, 2020.

[91] F. Jin, X. Ma, P. Guo, C. Yi, L. Wang, Y. Wang, Q. Yu, J. Sheng, A. Zhang, J. Ji, et al. Raman scattering study of large magnetoresistance semimetals $TaAs_2$ and $NbAs_2$. *Phys. Rev. B*, **94**(9):094302, 2016.

[92] D. Wu, J. Liao, W. Yi, P. Wang, X.and Li, H. Weng, Y. Shi, Y. Li, J. Luo, X. Dai, et al. Giant semiclassical magnetoresistance in high mobility $TaAs_2$ semimetal. *Appl. Phys. Lett.*, **108**(4):042105, 2016.

[93] G. Chang, S.-Y. Xu, D. S. Sanchez, S.-M. Huang, C.-C. Lee, T.-R. Chang, G. Bian, H. Zheng, I. Belopolski, N. Alidoust, et al. A strongly robust type II Weyl fermion semimetal state in $Ta_3S_2$. *Sci. Adv.*, **2**(6):e1600295, 2016.

[94] A. Tamai, Q. Wu, I. Cucchi, F. Y. Bruno, S. Riccò, T. K. Kim, M. Hoesch, C. Barreteau, E. Giannini, C. Besnard, et al. Fermi arcs and their topological character in the candidate type II Weyl semimetal $MoTe_2$. *Phys. Rev. X*, **6**(3):031021, 2016.

[95] K. Deng, G. Wan, P. Deng, K. Zhang, S. Ding, E. Wang, M. Yan, H. Huang, H. Zhang, Z. Xu, et al. Experimental observation of topological Fermi arcs in type II Weyl semimetal $MoTe_2$. *Nat. Phys.*, **12**(12):1105–1110, 2016.

[96] W. Wang, X. Zhang, Y. Zhao, H. Xu, Q. Lu, C. Liu, X. Hu, Ion C. Edmond T., L. He, W. Zou, et al. The metal-insulator transition in $ZrTe_5$ induced by temperature. *AIP Adv.*, **8**(12):125110, 2018.

[97] J. Wang, H. Yang, L. Ding, W. You, C. Xi, J. Cheng, Z. Shi, C. Cao, Y. Luo, Z. Zhu, et al. Angle-dependent magnetoresistance and its implications for Lifshitz transition in $W_2As_3$. *npj Quantum Mater.*, **4**(1):58, 2019.

[98] Y.-Y. Wang, Q.-H. Yu, P.-J. Guo, K. Liu, and T.-L. Xia. Resistivity plateau and extremely large magnetoresistance in $NbAs_2$ and $TaAs_2$. *Phys. Rev. B*, **94**(4):041103, 2016.

[99] J. Xu, F. Han, T.-T. Wang, L. R. Thoutam, S. E. Pate, M. Li, X. Zhang, Y.-L. Wang, R. Fotovat, U. Welp, et al. Extended Kohler's rule of magnetoresistance. *Phys. Rev. X*, **11**(4):041029, 2021.

[100] A. Narayanan, M. D. Watson, S. F. Blake, N. Bruyant, L. Drigo, Y. L. Chen, D. Prabhakaran, B. Yan, C. Felser, T. Kong, et al. Linear magnetoresistance caused by mobility fluctuations in n-doped $Cd_3As_2$. *Phys. Rev. Lett.*, **114**(11):117201, 2015.

[101] J. Antoszewski, D. J. Seymour, L. Faraone, J. R. Meyer, and C. A. Hoffman. Magneto-transport characterization using quantitative mobility-spectrum analysis. *J. Electron. Mater.*, **24**:1255–1262, 1995.

[102] J. R. Meyer, C. A. Hoffman, J. Antoszewski, and L. Faraone. Quantitative mobility spectrum analysis of multicarrier conduction in semiconductors. *J. Appl. Phys.*, **81**(2):709–713, 1997.

[103] I. Vurgaftman, J. R. Meyer, C. A. Hoffman, D. Redfern, J. Antoszewski, L. Faraone, and J. R. Lindemuth. Improved quantitative mobility spectrum analysis for Hall characterization. *J. Appl. Phys.*, **84**(9):4966–4973, 1998.

[104] Y. Hinuma, G. Pizzi, Y. Kumagai, F. Oba, and I. Tanaka. Band structure diagram paths based on crystallography. *Comput. Mater. Sci.*, **128**:140–184, 2017.

[105] M.-D. Zhang, X.-Y. Hou, Q. Wang, Y.-Y. Wang, L.-X. Zhao, Z. Wang, Y.-D. Gu, F. Zhang, T.-L. Xia, Z.-A. Ren, et al. Tip-induced superconductivity on the topological semimetals $TaAs_2$ and $NbAs_2$. *Phys. Rev. B*, **102**(8):085139, 2020.

[106] P. Zhang, P. Richard, T. Qian, Y.-M. Xu, X. Dai, and H. Ding. A precise method for visualizing dispersive features in image plots. *Rev. Sci. Instrum.*, **82**(4), 2011. 043712.

[107] F. Baumberger, W. Auwärter, T. Greber, and J. Osterwalder. Electron coherence in a melting lead monolayer. *Science*, **306**(5705):2221–2224, 2004.